General Disclaimer

One or more of the Following Statements may affect this Document

- This document has been reproduced from the best copy furnished by the organizational source. It is being released in the interest of making available as much information as possible.

- This document may contain data, which exceeds the sheet parameters. It was furnished in this condition by the organizational source and is the best copy available.

- This document may contain tone-on-tone or color graphs, charts and/or pictures, which have been reproduced in black and white.

- This document is paginated as submitted by the original source.

- Portions of this document are not fully legible due to the historical nature of some of the material. However, it is the best reproduction available from the original submission.

Produced by the NASA Center for Aerospace Information (CASI)

SINGLE-STAGE
EXPERIMENTAL EVALUATION OF
TANDEM-AIRFOIL ROTOR AND STATOR
BLADING FOR COMPRESSORS,

PART VIII - FINAL REPORT

By J. A. Brent and D. R. Clemmons

**PRATT & WHITNEY AIRCRAFT
DIVISION OF UNITED AIRCRAFT CORPORATION
FLORIDA RESEARCH AND DEVELOPMENT CENTER**

1. Report No. NASA CR-134713	2. Government Accession No.	3. Recipient's Catalog No.
4. Title and Subtitle "SINGLE-STAGE EXPERIMENTAL EVALUATION OF TANDEM-AIRFOIL ROTOR AND STATOR BLADING FOR COMPRESSORS," PART-VIII FINAL REPORT		5. Report Date November 1974
		6. Performing Organization Code
7. Author(s) J. A. Brent and D. R. Clemmons		8. Performing Organization Report No. FR-6247
		10. Work Unit No.
9. Performing Organization Name and Address Pratt & Whitney Aircraft Division of United Aircraft Corporation Florida Research and Development Center West Palm Beach, Florida 33402		
		11. Contract or Grant No. NAS3-11158
		13. Type of Report and Period Covered Contractor Report
12. Sponsoring Agency Name and Address National Aeronautics and Space Administration Washington, D. C. 20546		
		14. Sponsoring Agency Code

15. Supplementary Notes
Project Manager, Everett E. Bailey, Fluid System Components Division,
NASA-Lewis Research Center, Cleveland, Ohio 44135

16. Abstract

An experimental investigation was conducted with an 0.8 hub/tip ratio, single-stage, axial flow compressor to determine the potential of tandem-airfoil (two airfoils in series) blading for improving the efficiency and stable operating range of compressor stages. The investigation was conducted in two phases, designated Tasks I and III of Contract NAS3-11158, and included testing of five individual stages.

The first phase (Task I) of the investigation included testing of a baseline stage with single-airfoil blading and two tandem-blade stages. The two tandem stages differed by the tangential loading split between the front and rear airfoils of the rotor. A common tandem stator was used for both tandem stages. The overall performance of the baseline stage and the tandem-blade stage with a 20-80% loading split was considerably below the design prediction. The other tandem-blade stage, which had a rotor with a 50-50% loading split, came within 4.5% of the design pressure rise ($\Delta \overline{P}/\overline{P}_1$) and matched the design stage efficiency.

In the second phase (Task III) of the investigation, the baseline stage with single-airfoil blading, which was designed to account for the actual rotor inlet velocity profile and the effects of axial velocity ratio and secondary flow, achieved the design predicted performance. The corresponding tandem-blade stage (50-50% loading split in both blade rows) slightly exceeded the design pressure rise but was 1.5 percentage points low in efficiency.

The tandem rotors tested during both phases demonstrated higher pressure rise and efficiency than the corresponding single-airfoil rotor, with identical inlet and exit airfoil angles. No improvement in the operating range between peak efficiency and incipient surge or the attenuation of either radial or circumferential inlet flow distortion was noted for the tandem-bladed stages. The conclusion regarding the inability of the tandem blading to improve the distortion attenuation over that achieved with conventional blading is based solely on the Task III data since the Task I baseline stage was not tested with inlet flow distortion.

17. Key Words (Suggested by Author(s)) Compressor Tandem Blading Secondary Flow	18. Distribution Statement Unclassified-Unlimited

19. Security Classif. (of this report) Unclassified	20. Security Classif. (of this page) Unclassified	21. No. of Pages 97	22. Price* $3.00

* For sale by the National Technical Information Service, Springfield, Virginia 22151

NASA-C-168 (Rev. 6-71)

FOREWORD

This report was prepared by the Pratt & Whitney Aircraft Division of United Aircraft Corporation, West Palm Beach, Florida, to summarize the experimental results obtained from test programs performed under Task I and Task III of Contract NAS3-11158, Single-Stage Experimental Evaluation of Tandem-Airfoil Rotor and Stator Blading for Compressors. Mr. Everett E. Bailey, NASA-Lewis Research Center, Fluid System Components Division, was Project Manager.

The requirements of NASA Policy Directive NPD 2220.4 (September 14, 1970) regarding the use of SI Units have been waived in accordance with the provisions of paragraph 5d of that Directive by the Director of Lewis Research Center.

CONTENTS

CONTENTS (Continued)

ILLUSTRATIONS

TABLES

SUMMARY

An experimental investigation was conducted with an 0.8 hub/tip ratio, single-stage, axial flow compressor to determine the potential of tandem-airfoil (two airfoils in series) blading for improving the efficiency and stable operating range of compressor stages. The investigation was conducted in two phases, designated Tasks I and III of Contract NAS3-11158, and included testing of five individual stages.

A highly loaded baseline stage, with conventional single-airfoil blading, and two tandem-airfoil stages were designed and tested during Task I. The tandem-airfoil stages differed by the loading split between the front and rear airfoils of the rotor, but utilized the same tandem stator. All three rotors were designed to produce a pressure ratio of 1.32 at a rotor tip velocity of 757 ft/sec. The design stage pressure ratios were 1.30. The predicted rotor and stage adiabatic efficiencies were 90.8% and 85.4%, respectively, for all three stages. Both tandem rotors demonstrated higher pressure rise and efficiency than the conventional single-airfoil rotor; however, all three stages failed to achieve their design pressure ratio at the design flow. The higher pressure rise for the tandem rotors was primarily attributed to higher turning for the tandem rotors. Tandem Stage C, which included a rotor with a 50-50% loading split between the airfoils in tandem, matched the design efficiency and was within 4.5% of the design pressure rise ($\Delta P/\overline{P}_1$) at design speed and flow. The efficiency of the other tandem stage, which included a rotor with a 20-80% loading split, and the efficiency of the conventional stage were both approximately 8 percentage points below the design value. The poor performance of the conventional stage was caused to a large extent by high losses near the walls. The superior performance of Stage C indicates a definite effect on performance due to rotor loading split.

No improvement in the operating range between peak efficiency and incipient surge was noted for the tandem-bladed stages. Thus, the hypotheses that the tandem blades should have a larger operating range than conventional blading and that tandem configurations designed with the majority of the loading on the rear airfoil should have a larger operating range than one with equal loadings were not substantiated. The failure of the tandem blades to improve the operating range apparently resulted because, contrary to the theoretical calculations, the rear airfoil loading did not remain constant as the incidence angle (i.e., loading) on the front airfoil was increased. In fact, the loading on the rear airfoil actually decreased, and the overall loading remained essentially constant above the design incidence angle. This observation is based solely on loading characteristics determined from pressure and suction surface static pressure measurements for the tandem-airfoil stators.

Based on the higher rotor pressure rise and efficiency demonstrated by the tandem rotors during Task I, a second investigation was initiated to evaluate the potential of tandem blading for improving the performance of a more moderately loaded stage not designed with high work input near the walls to offset the high losses and the associated three-dimensional flows in these regions. A conventional stage and a tandem-bladed stage were designed and tested during this second investigation. A study was performed to select a design pressure ratio and radial work gradient, which resulted in the maximum rotor and stator

loading levels consistent with good performance. Based on this study, the rotors were designed for a pressure ratio of 1.28 at a tip speed of 757 ft/sec, with a uniform work input at all radii, as compared to a pressure ratio of 1.32, with higher work input near the walls for the Task I blading. The Task III stage design pressure ratios were 1.26. The predicted rotor and stage efficiencies for Task III were 89.9% and 84.8%, respectively. Because of the large inlet boundary layer noted during the Task I testing, the inlet total pressure gradient, with the resulting velocity gradient, and the effects of axial velocity ratio and secondary flow on blade row performance were accounted for during the design of the Task III blading.

The conventional stage tested during Task III achieved its design pressure ratio and efficiency at the design point, whereas the tandem-bladed stage tested during Task III exceeded the design pressure ratio but was 1.5 percentage points below the design efficiency at the design point. In accordance with the Task I results, the Task III tandem rotor had a higher pressure rise and efficiency than the conventional rotor at the design point, and the operating range between peak efficiency and incipient   ge was approximately the same for both the tandem and conventional stage.

Even though the tandem rotors demonstrated a higher pressure rise capability than the conventional rotors, the level of improvement over that obtainable with a well-designed conventional stage does not appear to justify the added cost and complexity associated with the tandem blades. The same result might have been achieved by simply adding camber to the conventional type rotors.

The fact that the Task III conventional stage designed to match the actual inlet velocity gradient and to include the effects of secondary flow and axial velocity ratio came much closer to achieving its design objective than the Task I stage is at least partially attributable to the technique used to design this stage. However, the complexity associated with manufacturing the blade end-bends that result from this technique may not be warranted unless the losses attributable to the end wall boundary layer are extremely high.

Both of the Task III stages were tested with hub radial, tip radial, and 90-deg circumferential distortion of the inlet flow. Hub radial and circumferential distortion generally had less effect on the performance of the stages than did tip radial distortion, which substantially reduced their performance relative to uniform inlet test results. No improvement in the attenuation of either radial or circumferential distortion was noted for the tandem-bladed stage.

2

INTRODUCTION

Advanced aircraft turbojet propulsion systems will require lightweight, highly loaded, axial flow compressors capable of achieving high efficiency over a wide range of operating conditions. Axial flow blower experience has indicated that tandem blading can be successfully employed to extend the efficient operating range of compressors. In 1955, H. E. Sheets (Reference 1) reported excellent efficiencies for a highly loaded, axial flow blower comprised of a tandem-blade rotor. Favorable results were also reported by H. Linnemann (Reference 2) based on a series of axial flow blower tests involving both tandem-blade rotors and stators. These results indicated that the tandem blading produced a better efficiency at a higher pressure ratio than that of equivalent conventional blading. Analytical studies of the effects of geometric and aerodynamic changes on the flow characteristics of tandem-airfoil stators, performed by N. L. Sanger at the NASA-Lewis Research Center and reported in References 3 and 4, also showed that most tandem configurations had lower losses than those calculated for a comparable conventional stator.

In principle, tandem blading offers improved performance over conventional blading by distributing the overall blade row aerodynamic loading between the airfoils in tandem. A new boundary layer is also begun on each airfoil, and the front airfoil provides control of the inlet air angle to the rear airfoil at off-design conditions. Thus, as shown in Reference 4, changes in overall incidence angle should result in significant increases in loading across the front segment. Therefore, tandem configurations designed with the majority of the loading on the rear airfoil should result in the largest operating range, since the rear airfoil loading remains essentially constant as the front airfoil loading increases with incidence angle until the loading limit (i.e., flow separation) is reached on the front airfoil.

This experimental program was initiated to evaluate the effectiveness of tandem airfoils as a means of improving the efficiency and stable operating range of compressor blade rows. The program was conducted under Tasks I and III of Contract NAS3-11158. Task I involved the design and test of a highly loaded, conventional, single-airfoil rotor and stator; two tandem-blade rotors; and a tandem-blade stator. The tandem-blade rotors differed by the loading split between the two airfoils in tandem. Task III entailed the design and testing of a more moderately loaded, conventional, single-airfoil stage and a tandem-bladed stage. Because of the large inlet boundary layer noted during the Task I testing, the Task III design procedure accounted for the inlet total pressure gradient, with the resulting velocity gradient, and the effects of axial velocity ratio and secondary flow on blade row performance. Within each task, the blade row leading and trailing edge metal angles for the conventional and tandem-blade rows were identical. A summary of these stages and their design intent is provided in table I.

The aerodynamic and mechanical designs of the Tasks I and III blading are presented in References 5 and 6, respectively. Performance data, as well as discussion of the test equipment and procedures, are presented in References 7 through 9 for the Task I blading and in References 10 and 11 for the Task III blading. Parts I and II of this report summarize the results obtained during Tasks I and III, respectively, and discuss these results relative to the program goals.

3

Table I. Summary of Compressor Stages

Task	Stage	Blading Type	Design Pressure Ratio	Diffusion Factor,* Rotor	Stator	Tandem Rotor Loading** Split
I	A	Conventional	1.30	0.522	0.511	---
I	B	Tandem	1.30	0.522	0.511	20% – 80%
I	C	Tandem	1.30	0.522	0.511	50% – 50%
III	D	Conventional	1.26	0.504	0.462	---
III	E	Tandem	1.26	0.504	0.462	50% – 50%

*Rotor and Stator diffusion factors are quoted for 10% and 90% span from the tip, respectively.

**Loading is defined as the tangential lift produced by the airfoil.

Part III discusses and evaluates: (1) the differences in the techniques used to design the Tasks I and III blading; (2) front-to-rear airfoil loading characteristics of the tandem stators with changes in front airfoil incidence angle; and (3) effects of inlet distortion on the tandem-bladed stages.

PART I

This portion of the report su.nmarizes the work performed under Task I. A conventional, single-airfoil rotor and stator (Rotor A and Stator A); one tandem-airfoil rotor with 20% of the overall loading on the front airfoil (Rotor B); a tandem-airfoil rotor with equal loading on each airfoil (Rotor C); and a tandem-airfoil stator (Stator B) intended for use behind each of the tandem rotors were designed and tested during Task I. Stator B was designed to provide the maximum differential in loading between the front and rear airfoils without exceeding a maximum suction surface-to-exit velocity ratio of 1.8. For the purposes of this report, loading was defined as the tangential lift produced by the airfoil.

SUMMARY OF STAGES A, B, AND C

Selection of Design Vector Diagrams

The selection of the design vector diagrams for Stages A, B, and C was accomplished within the range of the design guidelines given in table II.

Table II. Design Guidelines

Rotor Tip Diameter	30 in. (minimum)
Hub-Tip Ratio	0.7 to 0.8
Rotor Tip Speed	900 fps (maximum)
Rotor Tip Diffusion Factor	Less than 0.55
Rotor Tip Solidity	1.4 to 1.5
Stator Hub Diffusion Factor	Less than 0.60
Stator Hub Solidity	1.5 or greater

In addition to the guidelines specified in table II, the following criteria were specified for the design:

1. No inlet guide vanes (axial inlet flow)
2. Radially constant rotor inlet and rotor exit total pressure
3. Axial stator discharge flow
4. Common flowpath geometries for all stages
5. Double circular arc blade sections.

To ensure a valid comparison between the conventional Stage A and the tandem-blade stages, the vector diagrams selected for Rotor and Stator A were used in the design of the tandem blading.

The vector diagram values were calculated by means of an iteration using an axisymmetric flow field calculation and selected loss correlations (Reference 5). The calculation procedure solved the continuity, energy, and radial equilibrium equations, which included the effects of streamline curvature and radial gradients of enthalpy and entropy. The iteration was terminated when the following groundrules had been satisfied: (1) rotor overall pressure ratio was 1.32; (2) rotor exit total pressure was constant spanwise; (3) rotor and stator diffusion factors at tip and hub, respectively, were less than values specified in table II; and (4) stator exit flow angle was axial across the span.

The flowpath used for this investigation is shown in figure 1. The flow-path selection was governed by existing hardware. For the design vector diagram calculations, blockage allowances of 2%, 5%, and 5% of local annulus area were assumed at the rotor inlet, rotor exit, and stator exit, respectively, to account for boundary layer growth on the flowpath walls. A rotor tip inlet Mach number of 0.8 and a specific flow of 33 lb/sec-ft^2 (based on annulus area) were selected as representative of design practice for compressor middle stages. A summary of the vector diagram calculation results along the design streamlines, which were selected to pass through 5, 10, 15, 30, 50, 70, 85, 90, and 95% span at the rotor exit instrumentation station, is presented in tables III and IV for the rotors and stators, respectively. The predicted rotor pressure ratio and adiabatic efficiency were 1.32 and 90.8%, respectively, at a design rotor tip speed of 757 ft/sec. The predicted pressure ratio and efficiency for the stage at design rotor speed were 1.30 and 85.4%, respectively.

Selection of Blade Geometry

Circular-arc airfoil sections were selected for the rotor and stator blading to be consistent with the Reference 3 studies. Design incidence (minimum loss) and deviation angles for the conventional blading of the baseline Stage A were calculated using equations 286 and 287 of Reference 12. The three-dimensional corrections for incidence and deviation angles were omitted from these equations.

To ensure interchangeability with the single-airfoil blading of Stage A, radial distributions of overall axial chord for tandem-blade Stage B (Rotor B – Stator B) and tandem blade Stage C (Rotor C– Stator B) were made identical to those for the Stage A blading. Similarly, the individual airfoil maximum thickness-to-chord ratio for each of the tandem-blade airfoils were made identical to the corresponding values selected for the Stage A blading. The individual airfoil chords for the tandem blades were arbitrarily set equal. The rotor camber angles were selected to provide the prescribed distribution of loading between the front and rear airfoils (20-80% for Rotor B and 50-50% for Rotor C). The Stator B camber angles were selected to provide a maximum differential in loading between the front and rear airfoils without exceeding a maximum suction surface-to-exit velocity ratio of 1.8 on the rear airfoil. For both the rotor and stator of the tandem-blade stages, the leading edge metal angle of the front air-foil and the trailing edge metal angle for the rear airfoil were equal to the leading and trailing edge metal angles, respectively, selected for Stage A. In keeping with the Reference 3 studies, the individual airfoils were positioned so that:

1. There was zero axial overlap of the front and rear airfoils

2. The passage width between the airfoils was approximately 10% of the front airfoil chord

3. The passage between the airfoils would be slightly convergent (inlet-to-exit area ratio slightly greater than one).

Details of the Task I blading aerodynamic and mechanical design are presented in Reference 5. Figures 2 and 3 show the blading designed for Rotors A, B, and C and Stators A and B, respectively. Tables A-1 through A-5 of Appendix A present the blade element geometry for each rotor and stator used in the Task I investigation.

6

Table III. Rotor Vector Diagram Calculation Results for Rotors A, B, and C

Equivalent Rotor Speed = 4210 rpm   Equivalent Rotor Tip Speed = 757 ft/sec   Equivalent Weight Flow = 110 lb/sec

| | Percent Span From Tip | | V'le (ft/sec) | Vzle (ft/sec) | V"θle (ft/sec) | β'le (deg) | Ule (ft/sec) | V"te (ft/sec) | Vzte (ft/sec) | V"θte (ft/sec) | β'te (deg) | Ute (ft/sec) | ∅ (deg) |
	Leading Edge	Trailing Edge											
Hub	96.5	95.0	778.0	484.5	608.8	51.49	608.8	483.8	463.4	138.9	16.49	610.5	1.08
	91.5	90.0	784.0	484.4	616.5	51.84	616.5	492.2	467.0	155.5	18.42	617.6	0.50
	86.4	85.0	790.1	484.3	624.2	52.19	624.2	5(0.2	469.8	171.6	20.07	624.7	-0.08
	70.9	70.0	808.5	483.8	647.8	53.24	647.8	523.3	476.7	215.9	24.36	645.9	-1.78
	50.0	50.0	833.5	482.6	679.6	54.52	679.6	548.2	480.2	264.3	28.83	674.2	-3.95
	29.1	30.0	858.7	480.8	711.5	55.95	711.5	562.1	474.0	302.2	32.53	702.6	-6.03
	13.6	15.0	877.4	479.0	735.1	56.91	735.1	566.1	463.1	325.6	35.11	723.8	-7.52
	8.5	10.0	883.5	478.4	742.8	57.22	742.8	566.0	458.6	331.8	35.88	730.9	-8.00
Tip	3.5	5.0	889.6	477.7	750.5	57.52	750.5	565.0	453.8	336.6	36.56	738.0	-8.44

| | Percent Span From Tip | | M'le | D | ω̄ | Loss Parameter | Ple (psia) | Tle (°R) | Pte (psia) | Tte (°R) |
	Leading Edge	Trailing Edge								
Hub	96.5	95.0	0.7102	0.5533	0.11341	0.03154	14.694	518.7	19.368	566.63
	91.5	90.0	0.7152	0.5447	0.10314	0.02876	14.694	518.7	19.369	566.20
	86.4	85.0	0.7212	0.5370	0.09446	0.02637	14.694	518.7	19.366	565.81
	70.9	70.0	0.7380	0.5171	0.07363	0.02067	14.694	518.7	19.367	565.94
	50.0	50.0	0.7608	0.5028	0.06131	0.01732	14.694	518.7	19.395	564.71
	29.1	30.0	0.7836	0.5057	0.07348	0.02085	14.694	518.7	19.395	565.53
	13.6	15.0	0.8005	0.5167	0.09534	0.02713	14.694	518.7	19.366	566.69
	8.5	10.0	0.8061	0.5224	0.10505	0.02988	14.694	518.7	19.363	567.28
Tip	3.5	5.0	0.8116	0.5296	0.11647	0.03318	14.694	518.7	19.363	568.04

Note: $\beta_{te} = 0$ and is constant with radius

7

Table IV. Stator Vector Diagram Calculation Results for Stators A and B

Equivalent Rotor Speed – 4210 rpm Equivalent Rotor Tip Speed = 757 ft/sec Equivalent Weight Flow = 110 lb/sec

	Percent Span From Tip		V_{le} (ft/sec)	V_{zle} (ft/sec)	$V'\theta_{le}$ (ft/sec)	β_{le} (deg)	V_{te} (ft/sec)	V_{zte} (ft/sec)	$V'\theta_{te}$ (ft/sec)	β_{te} (deg)	α (deg)
	Leading Edge	Trailing Edge									
Hub	95.0	95.0	667.2	471.9	471.7	44.99	480.0	450.0	0.0	0.0	-0.05
	90.0	90.1	663.0	475.4	462.2	44.20	481.9	481.9	0.0	0.0	-0.10
	85.0	85.2	658.9	478.2	453.3	43.47	483.6	483.6	0.0	0.0	-0.15
	70.0	70.1	648.6	485.1	430.5	41.58	488.8	488.8	0.0	0.0	-0.28
	50.0	50.0	638.6	489.2	410.5	40.00	494.4	494.4	0.0	0.0	-0.47
	30.0	29.8	628.6	483.9	401.1	39.66	494.7	494.6	0.0	0.0	-0.63
	15.0	14.8	619.8	474.1	399.2	40.09	492.2	492.0	0.0	0.0	-0.77
	10.0	9.9	617.4	470.1	400.2	40.40	491.4	491.4	0.0	0.0	-0.80
Tip	5.0	4.9	615.6	465.8	402.5	40.84	491.2	491.2	0.0	0.0	-0.85

	Percent Span From Tip		M_{le}	D	$\bar{\omega}$	Loss Parameter	P_{te} (psia)
	Leading Edge	Trailing Edge					
Hub	95.0	95.0	0.5915	0.5183	0.09619	0.03242	18.975
	90.0	90.1	0.5878	0.5106	0.09171	0.03125	18.999
	85.0	85.2	0.5840	0.5035	0.08721	0.03004	19.017
	70.0	70.1	0.5747	0.4840	0.07636	0.02717	19.070
	50.0	50.0	0.5655	0.4672	0.07100	0.02634	19.126
	30.0	29.8	0.5556	0.4649	0.07570	0.02926	19.116
	15.0	14.8	0.5468	0.4695	0.08253	0.03276	19.072
	10.0	9.9	0.5442	0.4722	0.08632	0.03457	19.057
Tip	5.0	4.9	0.5422	0.4755	0.08920	0.03602	19.050

8

RESULTS AND DISCUSSION

Performance of Stages A, B, and C

Stage A, with conventional single-airfoil blading, was tested to establish a performance baseline for comparison with the results of subsequent tests of Stage B and Stage C, which comprised tandem airfoil rotors and stators. The overall and blade element performance results, including the effects of loading split on tandem-airfoil performance and the effects of tandem-airfoil blading on loading limit and stable operating range, are discussed in the following paragraphs. Descriptions of the compressor test facility, compressor test rig, instrumentation, test and data reduction procedures, and complete tabulations of overall and blade element performance data for Stages A, B, and C are presented in References 7, 9, and 8, respectively.

Overall Performance

The overall performance with uniform inlet flow for the single-airfoil and the two tandem-airfoil configurations is compared for the rotor in figure 4 and for the stage in figure 5. As shown in figure 4, both tandem rotors exhibited higher peak pressure ratio values at each rotor speed than the conventional single-airfoil Rotor A. At approximately design equivalent rotor speed and flow, Rotors A, B, and C achieved efficiencies of 83, 84, and 92%, respectively, compared to the predicted value of approximately 91% for the Task I rotor designs.

As shown in figure 5, all three stages failed to achieve their predicted pressure ratio of 1.30 at design flow and rotor speed. Stage C, however, came within 4.5% of the design pressure rise ($\Delta \overline{P}/\overline{P}_1$). At approximately design equivalent rotor speed and flow, the efficiency of Stage C was equal to the predicted value of approximately 85%, while the efficiencies of Stages A and B were both 77%. In general, Stage C had the highest efficiency at each rotor speed tested, and, at the peak efficiency point for design equivalent rotor speed, all three stages exhibited a surge margin of approximately 18%.

Blade Element Performance for Rotors

As noted in figure 4, all three rotors did not achieve their design pressure ratio, although Rotor C closely approached its pressure ratio goal and exceeded its efficiency goal. The radial distributions of loss coefficient and deviation angle for all three rotors at near design flow and design rotor speed are compared to the design values in figure 6. The loss coefficient data indicate that all rotors experienced endwall losses on the order of twice those assumed during the design. Tandem Rotor C produced lower losses than Rotors A or B, particularly between hub and midspan, thus accounting for its superior efficiency. Similar trends are seen in the deviation angle data in that all rotors produced greater-than-design deviation in the wall region and values nearer to design in the midspan region. Rotor C achieved the greatest turning in the midspan region, and matched its design values very well from 15 to 70% span.

The distributions of loss and deviation angle noted are typical for blading in a highly loaded or overloaded condition. The superior performance of tandem Rotor C is attributable to its "cascade" or two-dimensional performance away from the wall region. In the midspan region, the 50-50% split in design loading between the tandem airfoils apparently produced the desired improvement in the blade boundary layers and did improve the performance of these elements. In the wall region, however, no real improvement is noted for the tandem airfoils.

The diffusion factor, work, and exit axial velocity distributions provided in figures 7 and 8 corroborate the loss and deviation angle data and show the resultant high diffusion and low axial velocities in the wall region and the low work levels, particularly in the midspan region, due to the high axial velocity as the flow is forced away from the walls.

The differences between the design rotor relative inlet velocity distributions and the actual velocity distributions (figure 9) may have been partially responsible for the high losses near the walls. The low velocities near the walls resulted in an increase in the rotor relative inlet air angles and caused the rotor to operate at higher-than-design incidence angles in these regions (figure 10). As indicated in Reference 2, high incidence angles can stall the blade sections near the walls and affect the blade row performance over a large portion of the blade span. It was also shown in Reference 2 that not accounting for the inlet velocity gradients near the walls during the aerodynamic design could have resulted in substantial errors in the prediction of rotor diffusion factors near the walls.

Rotor loss parameter is presented as a function of diffusion factor at design equivalent rotor speed in figure 11 for the hub, mean, and tip (90, 50, and 10% span) sections of Rotors A, B, and C. The correlation curves from Reference 5 that were used to design the rotor are included for comparison with the test data. Near the tip and at midspan the data agree fairly well with the correlation; however, near the hub higher losses are noted. At the tip and midspan sections, both tandem rotors tended to produce lower loss parameter values than the conventional blading for the higher loading levels, an indication of the ability of tandem blading to extend the loading limit for conventional blading designs.

Blade Element Performance for Stators

The stator inlet velocity and incidence angle distributions for approximately design equivalent rotor speed and flow are shown in figure 12. Stators A, B, and BC (i.e., Stator B when tested with Rotor C) were operating with less than design incidence across most of the span due to the combination of high rotor exit axial velocity in the midspan region and higher-than-predicted rotor deviation angles (figure 6). Although all three rotors exhibited deviation angles higher than predicted near both walls, the reduction in rotor exit axial velocity near the walls was large enough to result in higher-than-predicted incidence angles in the hub and tip regions of Stators A, B, and BC. However, as indicated in figure 13 for 10, 50 and 90% span, the stator incidence angles at design equivalent rotor speed and flow are within the low-loss incidence operating ranges for the individual blade elements. The variations in stator inlet conditions, therefore, should not have adversely affected stator performance.

The blade element performance for Stators A, B, and BC is summarized in figure 14, which presents the radial distributions of loss coefficient, deviation angle, and diffusion factor at design incidence angle for each blade element. Loss coefficient data are not shown for Stator B at 5 and 95% span because the stator exit wake probes had been deleted at those locations. The data for each stator configuration were summarized from the curves presented in the pertinent data and performance report (References 7 through 9) and represent a condition that was not simultaneously achieved at all spanwise locations. However, this technique provides a method of comparing each blade element at its intended design inlet angle. Of particular notice in figure 14 is that the tandem stator exhibited much higher losses than Stator A in the endwall regions even though the loadings were much less than the Stator A loadings. Also, the tandem stator exhibited generally the same loss and loading levels across the span when tested with either of the tandem rotors. Stator A deviation angles were close to the design values between 50 and 95% span, whereas Stators B and BC had higher deviation angles across the entire span. Except for the hub region of Stator A, the stator diffusion factors are less than the predicted values across the entire span.

Loss parameter vs diffusion factor for Stators A, B, and BC is presented in figure 15 for the hub, mean, and tip (90, 50, and 10% span) sections at design equivalent rotor speed. Correlation curves from Reference 5 that were used to design the stator are included on figure 15 for comparison with the test data. In general, for equivalent levels of loading, the tandem stator, when tested with either of the two tandem rotors, appears to have exhibited slightly lower loss parameter values than did Stator A in the tip and midspan regions and higher loss parameter values at the hub. The differences between the tandem stator performance and the Stator A performance, however, are generally small enough to fall within the range of normal data scatter. The tandem stator also operated over a much wider range of loading at each span location than did Stator A and repeated its loss parameter vs loading characteristic fairly well for both stage configurations. This latter result is in accord with the spanwise loss and loading results shown in figure 14.

Stage B Tests With Radial and Circumferential Inlet Flow Distortion

Stage B was tested at 70, 90, and 100% design equivalent rotor speed with hub radial and tip radial distortion of the inlet flow to obtain overall performance, blade element performance, and flow distribution data for comparison with the uniform inlet flow performance results. Similar tests with 90-deg circumferential inlet flow distortion were performed to obtain overall performance and flow distribution data. Since Stages A and C were not tested with distortion, no comparison of distorted inlet performance can be made for the Task I stages. Details of the Stage B distortion tests, related test equipment, overall performance maps, blade element performance plots, flow distribution plots, and tabulations of performance and flow distribution data are presented in Reference 9.

PART II

Based on the fact that the highly loaded tandem rotors tested during Task I demonstrated higher pressure rise and efficiency than the single airfoil rotor with identical inlet and exit airfoil angles, a second investigation, designated Task III, was initiated to evaluate the potential of tandem blading for improving the performance of a more moderately loaded stage. Furthermore, the fact that the Task I stages were not designed to match the actual inlet velocity profile and exhibited high losses in the wall regions prompted further investigation of tandem-airfoil blading, based on an aerodynamic design that accounted for the actual inlet conditions. A single-airfoil rotor and stator, a dual-airfoil tandem rotor, and a dual-airfoil tandem stator were designed and tested during Task III. The conventional single airfoil rotor and stator were designated Rotor D and Stator D. The tandem-blade rotor and stator were designated Rotor E and Stator E.

SUMMARY OF STAGES D AND E

Selection of Design Vector Diagrams

The selection of the design vector diagrams was accomplished within the range of the design guidelines given in table II, which also applied to the design of the Task I stages. In addition to the guidelines presented in table II, the following criteria were specified for the Stage D and E designs:

1. No inlet guide vanes (axial inlet flow)

2. Use rotor inlet total pressure profile from data obtained during Task I program for the same inlet configuration

3. Axial stator discharge flow

4. Use same flowpath as used for the Task I stages.

To ensure a valid comparison between the conventional Stage D (Rotor D - Stator D) and the tandem-blade Stage E (Rotor E - Stator E), the vector diagrams selected for Rotor D and Stator D were used to design the tandem blading. This approach was also used in the Task I design.

Prior to the selection of the final design vector diagrams, a study was performed to select a radial work gradient and level for the rotor that resulted in maximum rotor and stator loading levels consistent with good performance (Reference 6). Based on this study, a rotor design with uniform work input at all radii and an average overall pressure ratio of 1.28 at a rotor tip speed of 757 ft/sec was chosen for the Task III investigation. The rotor designs of Task I had higher work input near the walls, whereas the rotors of Task III had no radial work gradient. The relatively lower work input near the walls for the Task III rotors was intended to help reduce the three-dimensional flows and high wall losses that are characteristic of highly loaded blade rows.

The vector diagrams were calculated by means of an iteration, using an axisymmetric flow field calculation and selected loss correlations (Reference 6). To better define the radial loss profile, the loss parameter vs diffusion factor correlation used in the Task I design (Reference 5) was expanded from three span locations (10, 50, and 90%) to five span locations (10, 30, 50, 70, and 90%). The 30 and 70% span data were obtained from the same references used in the three-span correlation (Reference 5). The five-span loss correlation was updated by adding data from NASA-sponsored programs (Reference 6) and unpublished loss data from FRDC single-stage compressor programs. The resultant design loss curves for each percent span are shown in Reference 6. The calculation procedure solved the continuity, energy, and radial equilibrium equations, which included the effects of streamline curvature and radial gradients of enthalpy and entropy. The iteration was terminated when the following groundrules had been satisfied: (1) rotor overall pressure ratio was 1.28; (2) rotor work input was constant spanwise; (3) rotor and stator diffusion factors at tip and hub, respectively, were less than values specified in table II, and (4) stator exit flow angle was axial across the span.

Blockages, rotor tip inlet Mach number, and specific flow values were the same as the values selected for the Task I design. A summary of the vector diagram calculations along the design streamlines, which pass through 5, 10, 15, 30, 50, 70, 85, 90, and 95% span at the rotor exit instrumentation station, is presented in tables V and VI for the rotors and stators, respectively. The predicted rotor pressure ratio and adiabatic efficiency were 1.28 and 89.9%, respectively, at a design rotor tip speed of 757 ft/sec. The predicted pressure ratio and efficiency for the stage at design equivalent rotor speed and flow were 1.26 and 84.8%, respectively.

Selection of Blade Geometry

Simulated double-circular-arc airfoil sections (i.e., the mean camber line and the suction and pressure surface lines of each blade element are lines with a constant rate of angle change with path distance on a specified conical surface) were selected for the rotor and stator blading. These blade sections, designed on conical surfaces, are analogous to conventional circular arc blading, which is designed on cylindrical surfaces. Design incidence and deviation angles for Stage D were selected, using the same methods employed in the Task I program for the Stage A blading. The thickness-to-chord ratio distributions, chord lengths, number of blades, and number of vanes used in the design of Stage A were also used in the Stage D design.

A study performed by Pratt & Whitney Aircraft has revealed better agreement between predicted and measured rotor and stator exit air angles when the cascade turning is modified to include the effects of axial velocity ratio and secondary flow. Consequently, the Stage D blading geometry selection included these corrections, whereas the Stage A design, which preceded the axial velocity ratio and secondary flow study, did not. The procedure for calculating the two-dimensional turning that combines with the axial velocity ratio and secondary flow corrections to produce the blade exit vector diagrams corresponding to the axisymmetric flow field calculations is presented in detail in Reference 6.

Table V. Rotor Vector Diagram Caluclation Results for Rotors D and E

Equivalent Rotor Speed = 4210 rpm   Equivalent Rotor Tip Speed = 757 ft/sec   Equivalent Weight Flow = 110 lb/sec

	Percentage Span From Tip		V_{zle} (ft/sec)	V'_{le} (ft/sec)	$V''_{\theta le}$ (ft/sec)	β'_{le} (deg)	U_{le} (ft/sec)	V'_{te} (ft/sec)	V_{zte} (ft/sec)	$V'_{\theta te}$ (ft/sec)	β'_{te} (deg)	U_{te} (ft/sec)	α (deg)
	Leading Edge	Trailing Edge											
Hub	96.9	95.0	458.8	758.6	608.7	53.00	608.7	416.8	371.3	191.5	27.95	610.5	1.32
	92.0	90.0	488.5	787.8	615.8	51.50	615.8	493.9	448.9	204.8	24.55	617.6	1.37
	86.9	85.0	500.5	800.7	623.8	51.10	623.8	535.6	491.5	215.9	23.72	624.7	0.89
	71.0	70.0	501.1	819.8	642.9	52.20	642.9	575.8	519.6	249.0	25.70	645.9	-1.17
	49.5	50.0	499.9	844.3	680.6	53.60	680.6	603.1	525.8	293.7	29.35	674.3	-4.21
	28.1	30.0	496.5	869.4	713.2	55.00	713.2	622.8	521.1	339.8	32.95	702.6	-7.16
	12.0	15.0	473.4	877.9	737.8	57.10	737.8	596.0	464.2	370.0	38.35	723.9	-9.37
	7.1	10.0	428.7	861.4	745.3	59.80	745.3	553.0	400.9	379.7	43.48	730.9	-9.64
Tip	3.0	5.0	375.1	837.2	751.5	64.10	751.5	483.5	270.0	388.9	53.00	738.0	-9.07

	Percent Span From Tip		M'_{le}	D	$\bar{\beta}'$	Loss Parameter	P_{le} (psia)	T_{le} (°R)	P_{te} (psia)	T_{te} (°R)
	Leading Edge	Trailing Edge								
Hub	96.8	95.0	0.697	0.604	0.236	0.0604	14.427	518.7	17.765	561.14
	92.0	90.0	0.719	0.530	0.162	0.0432	14.659	518.7	18.361	561.15
	86.9	85.0	0.732	0.484	0.106	0.0288	14.694	518.7	18.735	561.14
	71.0	70.0	0.750	0.453	0.064	0.0177	14.699	518.7	19.000	561.34
	49.5	50.0	0.774	0.436	0.046	0.0129	14.693	518.7	19.063	561.34
	28.1	30.0	0.796	0.426	0.056	0.0158	14.701	518.7	19.010	561.07
	12.0	15.0	0.801	0.461	0.123	0.0335	14.602	518.7	18.465	561.28
	7.1	10.0	0.783	0.504	0.150	0.0382	14.308	518.7	17.915	561.14
Tip	3.0	5.0	0.757	0.567	0.201	0.0428	13.820	518.7	17.130	561.38

Note: $\beta_{te} = 0$ and I_{te} is constant with radius.

Table VI. Stator Vector Diagram Calculation Results for Stators D and E

Equivalent Rotor Speed = 4210 rpm Equivalent Rotor Tip Speed = 757 ft/sec Equivalent Weight Flow = 110 lb/sec

	Percent Span From Tip		Vle (ft/sec)	Vzle (ft/sec)	V'θle (ft/sec)	βle (deg)	V'te (ft/sec)	Vzte (ft/sec)	V'θte (ft/sec)	βte (deg)	e (deg)
	Leading Edge	Trailing Edge									
Hub	95.0	95.0	569.9	383.9	417.7	47.65	395.1	395.1	0.0	0.0	-0.29
	90.0	90.0	616.8	456.9	412.8	41.90	472.2	472.2	0.0	0.0	-0.57
	85.0	85.0	645.3	501.1	407.9	39.20	514.3	514.3	0.0	0.0	-0.86
	70.0	70.0	659.8	526.2	396.8	37.00	543.9	543.9	0.0	0.0	-1.72
	50.0	50.0	655.9	533.7	380.5	35.50	554.2	554.2	0.0	0.0	-2.86
	30.0	30.0	642.5	529.8	362.9	34.40	547.8	547.8	0.0	0.0	-4.00
	15.0	15.0	595.2	471.9	354.3	36.50	486.2	486.2	0.0	0.0	-4.86
	10.0	10.0	538.1	407.2	349.0	40.40	417.2	417.2	0.0	0.0	-5.14
Tip	5.0	5.0	450.2	284.3	349.1	52.50	298.4	298.4	0.0	0.0	-5.43

	Percent Span From Tip		Mle	D	ω̄	Loss Parameter	Pte (psia)
	Leading Edge	Trailing Edge					
Hub	95.0	95.0	0.5024	0.540	0.0972	0.02216	17.419
	90.0	90.0	0.5463	0.462	0.0803	0.02027	18.117
	85.0	85.0	0.5751	0.423	3.0712	0.01902	18.472
	70.0	70.0	0.5867	0.389	0.0604	0.01714	18.748
	50.0	50.0	0.5832	0.369	0.0534	0.01610	18.864
	30.0	30.0	0.5709	0.364	0.0587	0.01866	18.762
	15.0	15.0	0.5262	0.418	0.0995	0.03165	18.153
	10.0	10.0	0.4748	0.488	0.1506	0.04575	17.534
Tip	5.0	5.0	0.3958	0.630	0.1634	0.04282	16.738

To ensure interchangeability with Stage D, the radial distributions of overall axial chord for tandem-blade Stage E were maintained equal to the distributions selected for the Stage D blading. The individual airfoil maximum thickness-to-chord ratios for the Rotor E and Stator E tandem blading were maintained equal to the corresponding values selected for the Stage D blading. The individual airfoil chords for the tandem blading were set equal to agree with the procedure for the Task I tandem blading selection. The Rotor E and Stator E camber angles were selected to provide an equal distribution of overall tangential lift (loading) between the front and rear airfoils. The individual airfoils for both the rotor and stator were positioned according to the same criteria specified in Part I for the Stage B and Stage C blading.

Details of the Task III blading aerodynamic and mechanical design are presented in Reference 6. Figures 16 and 17 show the blading designed for Rotors D and E and Stators D and E, respectively. The large variations in twist in the end regions of both the rotor and stator resulted from the design procedure, which accounted for the actual rotor inlet boundary layer, and included the effects of axial velocity ratio and secondary flow on blade row performance. Tables A-6 through A-9 of Appendix A present the blade element geometry for each rotor and stator used in the Task III investigation.

RESULTS AND DISCUSSION

Performance of Stages D and E

Stage D, with conventional single-airfoil blading, was tested to establish a performance baseline for comparison with the results of a subsequent test of Stage E, which comprised a tandem-airfoil rotor and a tandem-airfoil stator. The overall and blade element performance results, including the effects of radial and circumferential distortion of the inlet flow field on the performance of both Stage D and Stage E, are discussed in the following paragraphs. Descriptions of the compressor test facility; compressor test rig; distortion screens; and instrumentation, test, and data reduction procedures and a complete tabulation of overall and blade element performance data for Stages D and E are presented in References 10 and 11, respectively.

Overall Performance

As shown in figure 18, tandem Rotor E demonstrated a higher pressure rise than the conventional Rotor D. At approximately design equivalent rotor speed and flow, tandem Rotor E achieved an efficiency of 89.8%, which was approximately one percentage point above the level achieved by Rotor D. At design equivalent rotor speed, the peak efficiencies of Rotors D and E were approximately equal. At 110% design equivalent rotor speed, the peak efficiency of Rotor E was higher than that of conventional Rotor D. However, Rotor D achieved the highest efficiency at each of the rotor speeds tested below design. The higher pressure rise capability of the tandem rotor is consistent with the results obtained with tandem Rotor C during Task I, as discussed earlier. As shown in figure 19, Stage D achieved the design pressure ratio and efficiency levels of 1.26 and 84.8% at design equivalent rotor speed and flow, whereas Stage E exceeded the design pressure ratio but fell 1.5 percentage points short of the design stage efficiency. Both Stage D and Stage E exhibited a surge margin of approximately 25% at the peak efficiency point for design equivalent rotor speed.

16

Blade Element Performance for Rotors

As was noted in figure 18, tandem Rotor E produced a higher overall pressure ratio than did the conventional Rotor D. The loss coefficient data shown in figure 20 shows that Rotor D losses were less than, or equal to, the design values at all spanwise locations; while tandem Rotor E losses were less than the design values in the hub-to-midspan region and slightly greater than design at the remaining span locations. Although the lower losses for Rotor E contributed to the higher pressure rise for this rotor, the lower deviation angles (i.e., more turning) in the hub to midspan region, as shown in figure 18, were primarily responsible for the higher pressure rise.

The diffusion factor, work, and exit axial velocity distributions provided in figures 21 and 22 corroborate the loss and deviation angle data. The slight differences between the actual and the predicted rotor work distributions shown in figure 21 resulted from local overturning or underturning of the flow. The discrepancies in rotor turning were produced by local variations of rotor deviation angle and exit axial velocity from their corresponding design distributions, as shown in figures 20 and 22.

Rotor loss parameter vs diffusion factor at design equivalent rotor speed is presented in figure 23 for the hub, mean, and tip (90, 50, and 10% span) sections of Rotors D and E. The correlation curves from Reference 6 that were used to design the rotor are included for comparison with the test data. From these data, there appears to be no improvement in the low-loss loading limit associated with tandem Rotor E.

Blade Element Performance for Stators

The stator inlet velocity and incidence angle distributions for approximately design equivalent rotor speed and flow are shown in figure 24 for Stator D and Stator E. Both stators were operating at, or slightly above, design incidence between 10% and 90% span. Near the endwalls, both stators were operating approximately 5 to 10 deg below design incidence. The difference between the stator incidence angles and their design distribution is directly related to whether the local rotor deviation angle and exit axial velocity were either above or below their respective design values, as shown in figures 20 and 22. Considering the relatively minor divergence from design stator inlet conditions between 10 and 90%, Stator D and Stator E performance values should not have been adversely affected by the variations just described.

The blade element performance for Stators D and E is summarized in figure 25, which presents the radial distributions of loss coefficient, deviation angle, and diffusion factor at design incidence for each blade element. The data for each stator configuration were summarized from the curves presented in the pertinent data and performance report (References 10 and 11) and represent a condition that was not simultaneously achieved at all spanwise locations. This technique, however, provides a method of comparing the performance of the blade elements at their design inlet air angle. Loss coefficient values for Stator D were above design at 10 and 15% span and less than or equal to design at all other span locations. Tandem Stator E losses were less than design at midspan and 95% span and higher than design elsewhere. Deviation angles for Stator E were close to the design distribution across the span, while Stator D deviation angles were slightly higher, especially at the hub and tip sections.

Stator D and Stator E diffusion factors were near the design values for the inner 50% of span and less than design for the outer 50% of span. The low diffusion factors in the tip region for both stators were primarily caused by the very high absolute velocity ratios (i.e., low diffusion) in the tip region, as shown in figure 26. Although these very high velocity ratio (V_{2A}/V_2) values might suggest a large flow separation in the tip region, the differences between the actual and design values of loss coefficient and deviation angles are not commensurate with highly separated flow conditions. As reflected by the reduced stator turning parameter $(\Delta V_\theta/V_2)$ shown in figure 26, the higher deviation angles for Stator D also affected diffusion factor, especially at 5% span from the tip.

Loss parameter vs diffusion factor for Stators D and E is presented in figure 27 for the hub, mean, and tip (90, 50, and 10% span) sections at design equivalent rotor speed. Correlation curves from Reference 6 that were used to design the stator are included in figure 27 for comparison with the test data. In general, for equivalent levels of loading, tandem Stator E exhibited slightly lower loss parameter values than did Stator D in the midspan regions and higher loss parameter values at the endwalls, especially the tip section.

EFFECT OF RADIAL INLET FLOW DISTORTION ON PERFORMANCE OF STAGES D AND E

Stage D and Stage E were tested at 70, 90, and 100% design equivalent rotor speed with tip radial and hub radial distortion of the inlet flow to obtain overall performance, blade element performance, and flow distribution data for comparison with their corresponding uniform inlet flow performance results. At a flow of approximately 115 lb/sec (i.e., 105% design equivalent weight flow), the hub and tip radial distortion screens produced approximately 15% and 16% total pressure distortion, i.e., $(P_{max}-P_{min})/P_{max}$, over the inner 47% and outer 38% of the compressor annulus area, respectively.

The following paragraphs include discussions pertaining to the effects of radial inlet flow distortion on the Stage D and Stage E overall performance and surge loading. The transfer of the total pressure distortion through each stage is also discussed below. Complete tabulations of blade element performance and flow distribution data are presented in Reference 10 for Stage D and Reference 11 for Stage E.

Overall Performance

Overall performance data obtained with hub radial distortion of the inlet flow are presented in terms of pressure ratio and adiabatic efficiency as functions of equivalent weight flow and equivalent rotor speed for Stages D and E in figures 28 and 29, respectively. Figures 30 and 31 similarly show the overall performance obtained with tip radial distortion of the inlet flow. Uniform inlet flow data and the stage design point are also shown in these figures for comparison with the radially distorted inlet flow data. The surge lines shown were determined from surge transient data.

In order to facilitate comparisons between the effects of hub and tip radial distortion on the individual stages, quantitative values were computed for the changes in certain performance parameters relative to that obtained for uniform inlet. The values computed for design equivalent speed are shown in table VII.

Table VII. Change in Stage D and Stage E Overall Performance
With the Addition of Hub and Tip Radial Distortion
at Design Equivalent Rotor Speed

	Hub Radial Distortion			
	$(\Delta\bar{P}/\bar{P})^*$	$\Delta(\eta_{ad})^*_{stage}$	$(\Delta\bar{P}/\bar{P})^{**}_{surge}$	$\Delta(W\sqrt{\theta}/\delta)_{surge}$
Stage D	-7.3	-0.4	-10.3	-4.4
Stage E	-10.9	-4.5	-11.4	+1.0
	Tip Radial Distortion			
Stage D	-11.9	-4.3	-33.0	+15.7
Stage E	-12.0	-4.3	-26.8	+13.6

*At Design Equivalent Weight Flow
**At Surge Flow With Distorted Inlet

$$\Delta\bar{P}/\bar{P} = \left[\frac{\left[(\bar{P}_{2A} - \bar{P}_1)/\bar{P}_1\right]_{distorted}}{\left[(\bar{P}_{2A} - \bar{P}_1)/\bar{P}_1\right]_{undistorted}} - 1.0\right] \times 100\%$$

$$\Delta(\eta_{ad})_{stage} = \left[\eta_{ad_{stage, distorted}} - \eta_{ad_{stage, undistorted}}\right] \times 100\%$$

$$\Delta(W\sqrt{\theta}/\delta)_{surge} = \left[\frac{(W\sqrt{\theta}/\delta)_{surge, distorted}}{(W\sqrt{\theta}/\delta)_{surge, undistorted}} - 1.0\right] \times 100\%$$

Included are: (1) the change in overall stage pressure ratio and efficiency along
the design weight flow line; (2) the change in surge line pressure ratio along a
constant flow line equal to the surge flow with distortion; and (3) the change in
surge flow. As indicated by the tabulated results and figures 28 through 31,
overall performance at design equivalent rotor speed and weight flow for Stage D
was reduced more by tip radial distortion than by hub radial distortion, while
the reduction in Stage E performance at the same conditions was only slightly
greater with tip radial distortion that with hub radial distortion. The addition
of tip radial distortion also had a more pronounced effect than the addition of
hub radial distortion on the surge line of both stages. As shown in table VII,
the surge pressure rise for Stages D and E with tip radial inlet distortion were
33% and 27% less, respectively, than the corresponding values at constant flow
without distortion, (i.e., loss in surge line). Both stages lost about 10% in pres-
sure rise at their respective surge flow points when tested with hub radial dis-
tortion. In general, both stages were more adversely affected by the addition
of tip radial distortion of the inlet flow, and the tandem-bladed Stage E did not
exhibit any clear improvement in radial distortion tolerance over Stage D.

Transfer of Radial Distortion Between
Stage Inlet and Exit

In order to evaluate the ability of the individual stages to attenuate the inlet distortion, the distortion parameter was calculated at each axial station with hub and tip radial distortion of the inlet flow and presented in figures 32 and 33 for Stages D and E, respectively. The ratio of the distortion parameter at each axial station to the value at the rotor inlet was computed for both stages and tabulated in table VIII. As shown by the magnitude of the values for the stator exit, Stage D attenuated tip radial distortion slightly better than hub radial distortion. Furthermore, Stage D attenuated both radial distortion patterns more effectively than tandem Stage E.

Loading Limitations on Rotors D and E With
Radial Distortion of the Inlet Flow

Rotor D diffusion factors at 10 and 90% span from the tip vs equivalent weight flow at design equivalent rotor speed for hub and tip radial distortion and uniform inlet flow are shown in figure 34. Similar results are shown in figure 35 for tandem Rotor E. Extrapolating the variation in diffusion factor with flow to the surge flow indicates that when either stage was tested with uniform and tip radially distorted inlet flow, the rotor tip diffusion factor at surge was approximately the same for both inlet flow conditions. The same level of surge loading at the rotor tip for uniform inlet flow and tip radial distortion is indicative of a rotor tip section limiting the operating range with uniform inlet flow. However, recordings of rotor exit pressure by high-response instrumentation as each stage was operated into and out of surge indicate that the hub, mean, and tip sections stalled simultaneously with uniform inlet flow and with both hub and tip radial distortion of the inlet flow.

Table VIII.   Ratio of Local Distortion Parameter to the
Value at Rotor Inlet for Stages D and E at
Design Equivalent Rotor Speed

STAGE D				
Axial Station	Hub Radial Distortion		Tip Radial Distortion	
	Maximum Flow (114.76 lb/sec)	Near-Surge Flow (84.40 lb/sec)	Maximum Flow (115.11 lb/sec)	Near-Surge Flow (99.09 lb/sec)
Rotor Inlet	1.0	1.0	1.0	1.0
Rotor Exit	0.66	0.78	0.62	0.81
Stator Exit	0.68	0.72	0.55	0.69

STAGE E				
	Maximum Flow (114.81 lb/sec)	Near-Surge Flow (93.49 lb/sec)	Maximum Flow (114.99 lb/sec)	Near-Surge Flow (103.95 lb/sec)
Rotor Inlet	1.0	1.0	1.0	1.0
Rotor Exit	0.72	0.88	0.71	0.92
Stator Exit	0.68	0.91	0.78	0.86

EFFECT OF CIRCUMFERENTIAL INLET FLOW DISTORTION
ON PERFORMANCE OF STAGES D AND E

Stage D and Stage E overall performance and flow distribution data were also obtained at 70, 90, and 100% design equivalent rotor speed with circumferential distortion of the inlet flow. At a flow of approximately 115 lb/sec (i.e., 105% design equivalent flow), the circumferential distortion screen produced approximately 13.5% total pressure distortion, i.e., $(P_{max}-P_{min})/P_{max}$, over a 90-deg sector of the compressor flow annulus.

Overall Performance

The Stage D and Stage E overall performance achieved with circumferential distortion of the inlet flow is compared with the performance obtained with uniform inlet flow in figures 36 and 37. The darkened symbols of figures 36 and 37 indicate the data points for which both overall performance and flow distribution data were recorded. The overall performance was calculated from pressures and temperatures measured at one circumferential location within, and one circumferential location outside, the low-pressure region. The pressures and temperatures were weighted according to the circumferential extent of the high- and low-pressure areas to obtain the average values for calculating the pressure ratio and efficiency. In an effort to verify some of the high Stage D efficiencies shown on figure 36, the overall performance was recalculated using a larger sample of the data within and outside the distorted area for the three data points for each stage at which data were recorded at six circumferential locations of the distortion screen. Recalculation of the overall performance values, as discussed in References 10 and 11, revealed that the larger data sample had little effect on pressure ratio but suggested that the efficiencies are not correct. Several unsuccessful efforts to correct the efficiency values were made by weighing the temperature data from the distorted and undistorted regions in different proportions. A larger data sample should be obtained in future test programs to obtain a more accurate assessment of the rotor and stage efficiencies with circumferential distortion of the inlet flow.

Reductions of stage pressure rise relative to uniform inlet test results for Stage D and Stage E, with circumferential distortion at design equivalent rotor speed for design equivalent flow and surge flow, are summarized in table IX. Although the effects of circumferential distortion on efficiency cannot be accurately evaluated, the relatively large decreases in surge pressure rise indicate that Stages D and E were significantly affected by circumferential distortion.

Table IX. Change in Stage D and Stage E Overall Performance With Circumferential Distortion at Design Equivalent Rotor Speed

	$(\Delta \bar{P}/\bar{P}_1)^*$	$(\Delta \bar{P}/\bar{P}_1)^{**}_{surge}$	$(W\sqrt{\theta}/\delta)_{surge}$
Stage D	−2.3	−20.4	4.7
Stage E	−8.3	−16.0	2.2

*At Design Equivalent Weight Flow
**At Surge Flow With Distorted Inlet

$$\Delta \bar{P}/\bar{P}_1 = \left[\frac{\left[(\bar{P}_{2A} - \bar{P}_1)/\bar{P}_1\right]_{distorted}}{\left[(\bar{P}_{2A} - \bar{P}_1)/\bar{P}_1\right]_{undistorted}} - 1.0 \right] \times 100\%$$

$$\Delta(W\sqrt{\theta}/\delta)_{surge} = \left[\frac{(W\sqrt{\theta}/\delta)_{surge,\ distorted}}{(W\sqrt{\theta}/\delta)_{surge,\ undistorted}} - 1.0 \right] \times 100\%$$

Stage D and Stage E Attenuation of Circumferential
Distortion of the Inlet Flow

Tables of flow distribution data (i.e., total pressure, total temperature, flow angles, velocity, Mach number, and turning) at each of the axial stations for circumferential increments of 30 deg around the compressor annulus; and circumferential distributions of total pressure, static pressure, total temperature, air angle, and axial velocity are presented in Reference 10 for Stage D and Reference 11 for Stage E. Figures 38 and 39 show the distortion parameters for Stages D and E calculated at each of the three span locations plotted vs the corresponding axial station. The ratios of the distortion parameter at each axial location to the value at the rotor inlet are tabulated for Stage D in table X and Stage E in table XI. As shown in figures 38 and 39 and tables X and XI, Stages D and E attenuated the circumferential distortion pattern in the tip region more effectively than at the hub or midspan sections for both flow conditions. A comparison of tables X and XI shows that Stage D attenuated the circumferential inlet distortion better than Stage E in the hub and midspan regions; however, Stage E attenuated the inlet distortion better in the tip region. Thus, on an overall basis no improvement in the attenuation of circumferential inlet distortion was noted for the tandem-bladed Stage E.

Table X. Ratio of Local Distortion Parameter to the Value at
Rotor Inlet for Stage D at Design Equivalent Rotor
Speed With Circumferential Distortion

Equivalent Weight Flow = 101.60 lb/sec

Location*	Rotor Inlet	Rotor Exit	Stator Exit
Hub (90)	1.0	0.490	0.559
Midspan (50)	1.0	0.451	0.588
Tip (10)	1.0	0.432	0.568

Equivalent Weight Flow = 90.59 lb/sec

Hub (90)	1.0	0.584	0.455
Midspan (50)	1.0	0.324	0.608
Tip (10)	1.0	0.554	0.405

*Numbers in Parenthesis Indicate Percent Span From Tip.

Table XI. Ratio of Local Distortion Parameter to the Value at
Rotor Inlet for Stage E at Design Equivalent Rotor
Speed With Circumferential Distortion

Equivalent Weight Flow = 103.40 lb/sec

Location*	Rotor Inlet	Rotor Exit	Stator Exit
Hub (90)	1.0	0.624	0.624
Midspan (50)	1.0	0.424	0.387
Tip (10)	1.0	0.284	0.370

Equivalent Weight Flow = 92.60 lb/sec

Hub (90)	1.0	0.673	0.733
Midspan (50)	1.0	0.416	0.714
Tip (10)	1.0	0.419	0.306

*Numbers in Parenthesis Indicate Percent Span From Tip.

23

PART III

EVALUATION OF DESIGN TECHNIQUES, TANDEM AIRFOIL LOADING CHARACTERISTICS, AND RADIAL AND CIRCUMFERENTIAL DISTORTION EFFECTS ON TANDEM-BLADED STAGES

Evaluation of Design Techniques
Used for Stage A and Stage D

A comparison of figures 5 and 18 shows that Stage D came much closer to achieving its design objective than Stage A. The relative success of Stage D is at least partially attributable to the technique used to design the stage. As previously discussed, the actual rotor inlet velocity profile and the effects of axial velocity ratio and secondary flow on blade row turning were accounted for in the Stage D design, whereas these effects were not included in the Stage A design. The importance of using the correct inlet velocity distribution is illustrated by comparing the Stage A and Stage D axial velocity and loading distributions calculated from the data with their corresponding design distributions, as shown in figures 40 and 41. Ignoring the inlet velocity gradients near the walls during the Stage A design resulted in substantially larger discrepancies between the estimated and measured values of the rotor and stator loading and exit velocities near the walls. These large discrepancies resulted because the rotor blade sections near the walls were operating at high incidence angles relative to the design intent. These high incidence angles caused high losses, with a resultant reduction in flow near the walls. The shifting of the flow away from the walls caused an increase in the midspan velocity, with a resultant decrease in midspan loading.

To illustrate the effectiveness of correcting the cascade turning for the effects of axial velocity ratio and secondary flow, the predicted exit air angles for Rotor A and Stator A both with and without the corrections are compared with the measured values in figures 42 and 43. Similar comparisons are made in figures 44 and 45 for Rotor D and Stator D, respectively. The corrected exit air angles for both the rotor and stator reveal consistently better agreement with the measured values than do the cascade predicted values.

As discussed in Reference 6, the Stator D geometry was selected by using only half of the camber angle correction that resulted from applying the secondary flow correction to the stator turning. This method was arbitrarily selected because the predicted secondary flow resulted in more overturning near the walls than had been observed from results of previous tests performed for NASA at Pratt & Whitney Aircraft. A comparison of the measured and predicted stator exit air angles, shown in figure 45, confirms the assumption that the secondary flow calculation predicts too much overturning at the stator endwall. These data show that the measured air angles at 5 and 95% span were in fact approximately half way between the predicted values, with and without the secondary flow correction.

Evaluation of Tandem-Airfoil Stator Loading
Characteristics for Stage B and Stage E

To determine the front-to-rear loading characteristics of tandem airfoil blading, the tandem-airfoil stators in both the Task I and Task III programs were instrumented with suction surface and pressure surface static pressure taps. Tandem Stator B had pressure taps at midspan on the pressure and suction surfaces of both the front and rear airfoils. Tandem Stator E had pressure taps at 10 and 90% span from the tip on both surfaces of both airfoils. Plots of static pressure coefficient vs percent overall stator chord for each data point recorded at design rotor speed are included in the data and performance reports for Stage B and Stage E (References 9 and 11, respectively). Figures 46 and 47 show variations in front airfoil loading, rear airfoil loading, and total loading as a function of front airfoil incidence angle at the indicated spanwise locations for Stator B and Stator E, respectively. The individual and total loading values are ratioed to their respective design values. Contrary to theoretical calculations, the rear airfoil loading did not remain constant as the incidence angle on the front airfoil was increased. Rear airfoil loading actually decreased, while the overall loading remained essentially constant above the design incidence angle. This result is evi'ent with both Stators P and E. Assuming that this result also applies to the rotor, it would explain the failure of tandem blading to improve on the operating range of the stages with conventional single-airfoil blading.

Evaluation of Radial and Circumferential
Distortion Effects on the Performance
of Tandem-Bladed Stages

Tandem-bladed Stage B was tested with both radial and circumferential distortion of the inlet flow. However, as was previously discussed, Stages A and C were not tested with distortion, thus precluding any comparisons of performance results with distortion for the Task I stages. Even though a true comparison of the performance of Stages B and E with distortion cannot be made since the two stages differed significantly in design goals and approach, it seems worthwhile to note that the two stages did exhibit similar results when tested with distortion. With either hub radial or circumferential distortion of the inlet flow, the performance of both stages was only slightly or moderately deteriorated relative to the undistorted performance results. With tip radial distortion, however, both stages experienced substantial reductions in both surge pressure ratio and the flow range between design flow and the surge flow point. Reference 9 contains a more detailed discussion of the performance of Stage B with distortion, and Part II of this report contains a discussion of the results obtained with Stage E.

SUMMARY OF RESULTS

An experimental investigation was conducted to determine the potential of tandem-airfoil (two airfoils in series) blading for extending the loading limit and stable operating range of compressor stages. The investigation was conducted in two phases, designated Tasks I and III of Contract NAS3-11158, and included testing of five individual stages. Task I had the secondary objective of determining the effect of the aerodynamic loading split between the two airfoils in series on the performance of tandem blading. The major results of this investigation are summarized below.

1. Tandem rotors offer slightly improved pressure rise capability; however, the same level of improvement might be achieved, without introducing the additional fabrication complexity associated with tandem blades, by simply adding camber to the conventional rotor.

2. For the compressor stages designed to match actual inlet conditions, no improvement in efficiency was obtained by incorporating tandem blading.

3. The distribution of loading between the front and rear airfoils of tandem blading can have a significant effect on performance. Rotors with a 50-50% loading split exhibited better performance, relative to design, than a rotor with a 20-80% loading split.

4. For operation at peak efficiency conditions, the surge margin for tandem-blade stages was not greater than for stages with conventional airfoil blading. The surge margin at peak efficiency was also independent of loading split.

5. Accounting for the actual rotor inlet velocity and the effects of axial velocity ratio and secondary flow on blade row turning can have a significant effect on the success or failure of a compressor designer to accurately predict the performance of a stage.

6. Tip radial distortion generally had a more severe effect on the overall performance of the stages tested during this investigation than did either hub radial or circumferential distortion.

7. No improvement in the attenuation of either radial or circumferential distortion was noted for tandem-bladed Stage E.

FLOW PATH DIMENSIONS

SCREEN SUPPORT STRUTS (6) BLADES (70) VANES (66)
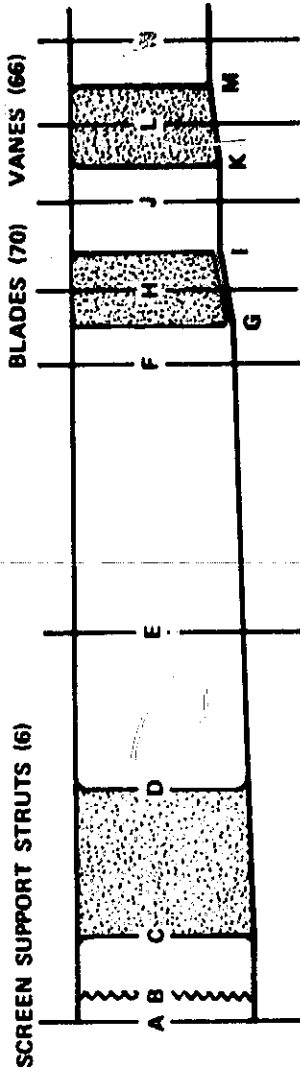
FLOWPATH LOCATION	LOCATION DESCRIPTION	INNER DIAMETER, in.	STAGES A, B, AND C		STAGES D AND E	
			OUTER DIAMETER, in.	AXIAL DISTANCE FROM REFERENCE PLANE, in.	OUTER DIAMETER, in.	AXIAL DISTANCE FROM REFERENCE PLANE, in.
A	REFERENCE PLANE	32.850	41.790	0.0	41.790	0.0
B*	DISTORTION SCREEN	32.850	41.790	1.500	41.790	1.500
C	SUPPORT STRUT LEADING EDGE	32.850	41.744	2.440	41.744	2.440
D	SUPPORT STRUT TRAILING EDGE	32.850	41.444	6.265	41.444	6.265
E	INSTRUMENTATION STATION 0	32.850	41.340	10.248	41.340	10.248
F	INSTRUMENTATION STATION 1	32.850	41.226	17.188	41.226	17.188
G	ROTOR INLET STATION	32.850	41.145	18.423	41.145	18.061
H	ROTOR STACKING LINE	32.850	40.854	19.188	40.860	19.188
I	ROTOR EXIT STATION	32.850	40.562	20.223	40.562	20.315
J	INSTRUMENTATION STATION 2	32.850	40.520	21.368	40.520	21.368
K	STATOR INLET STATION	32.850	40.450	22.163	40.450	22.163
L	TANDEM STATOR FRONT AIRFOIL TRAILING EDGE	32.850	40.244	23.160	40.228	23.276
M	STATOR EXIT STATION	32.850	39.990	24.468	39.990	24.468
N	INSTRUMENTATION STATION 2A	32.850	39.993	25.418	39.990	25.418

* SUPPORT SCREEN INSTALLED FOR TESTING STAGES B, D, AND E

NOTE: ALL DIMENSIONS ARE IN INCHES.

Figure 1. Flowpath Dimensions

FD 84172
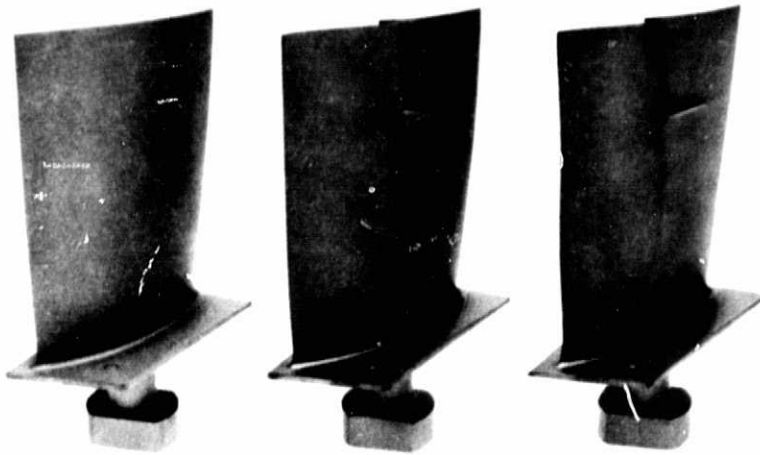
Figure 2. Rotor A, B, and C Blading FAE 133393
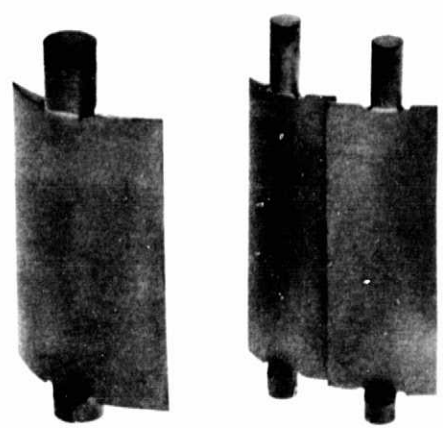
Figure 3. Stator A and B Blading FAE 133396

28
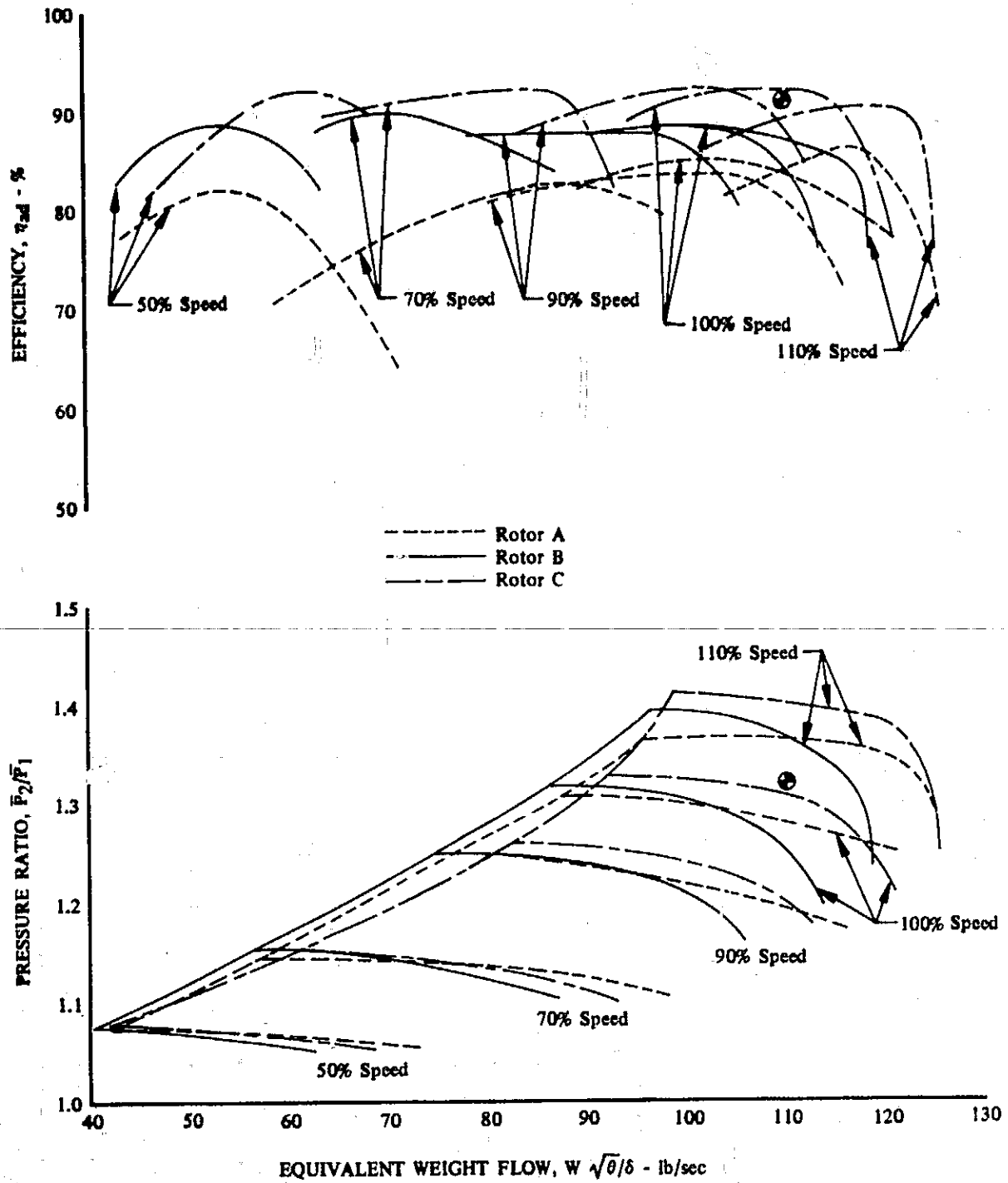
Figure 4. Overall Performance of Rotors A, B, and C; Uniform inlet Flow

DF 100315
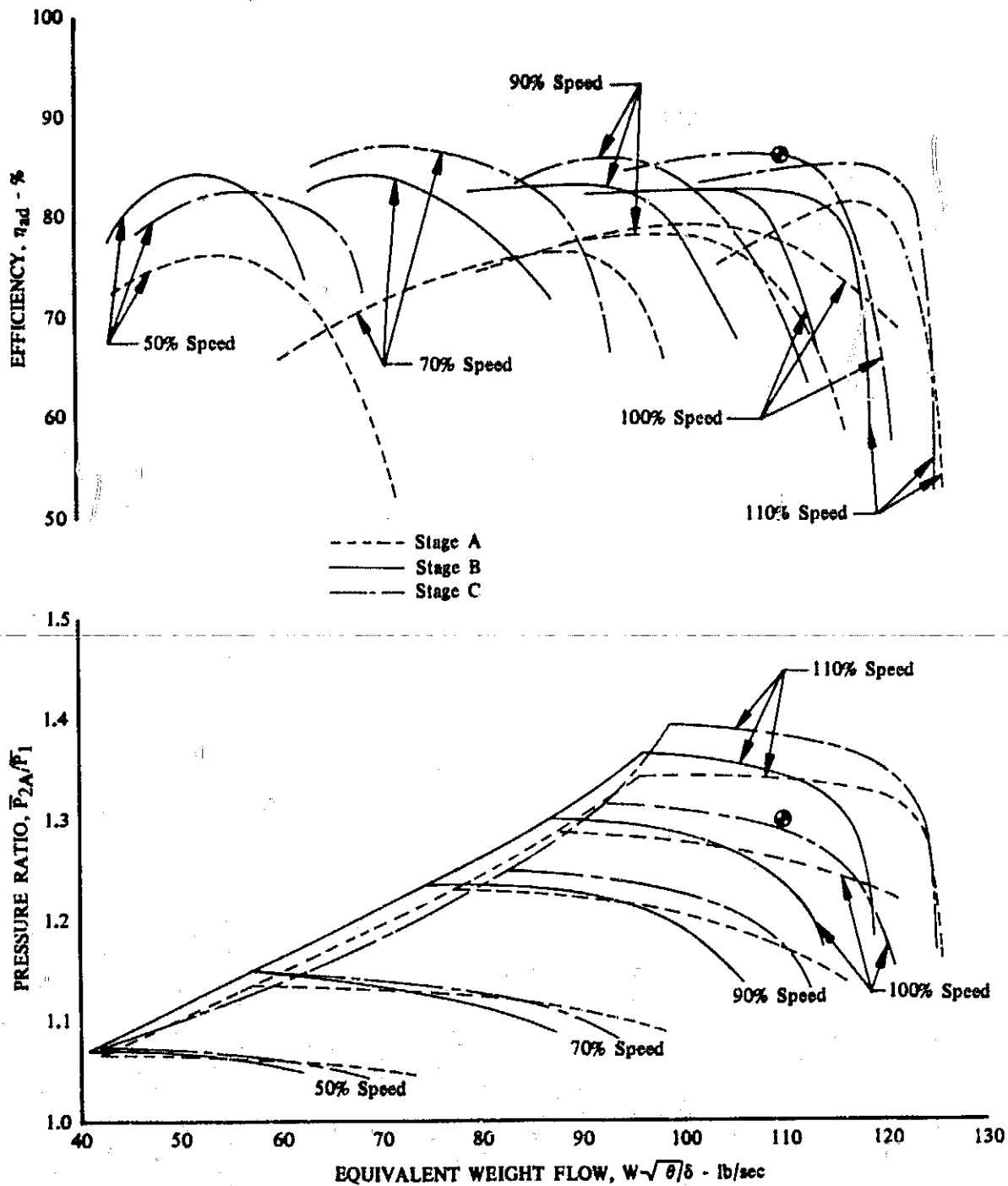
Figure 5. Overall Performance of Stages A, B, and C; Uniform Inlet Flow

DF 100316
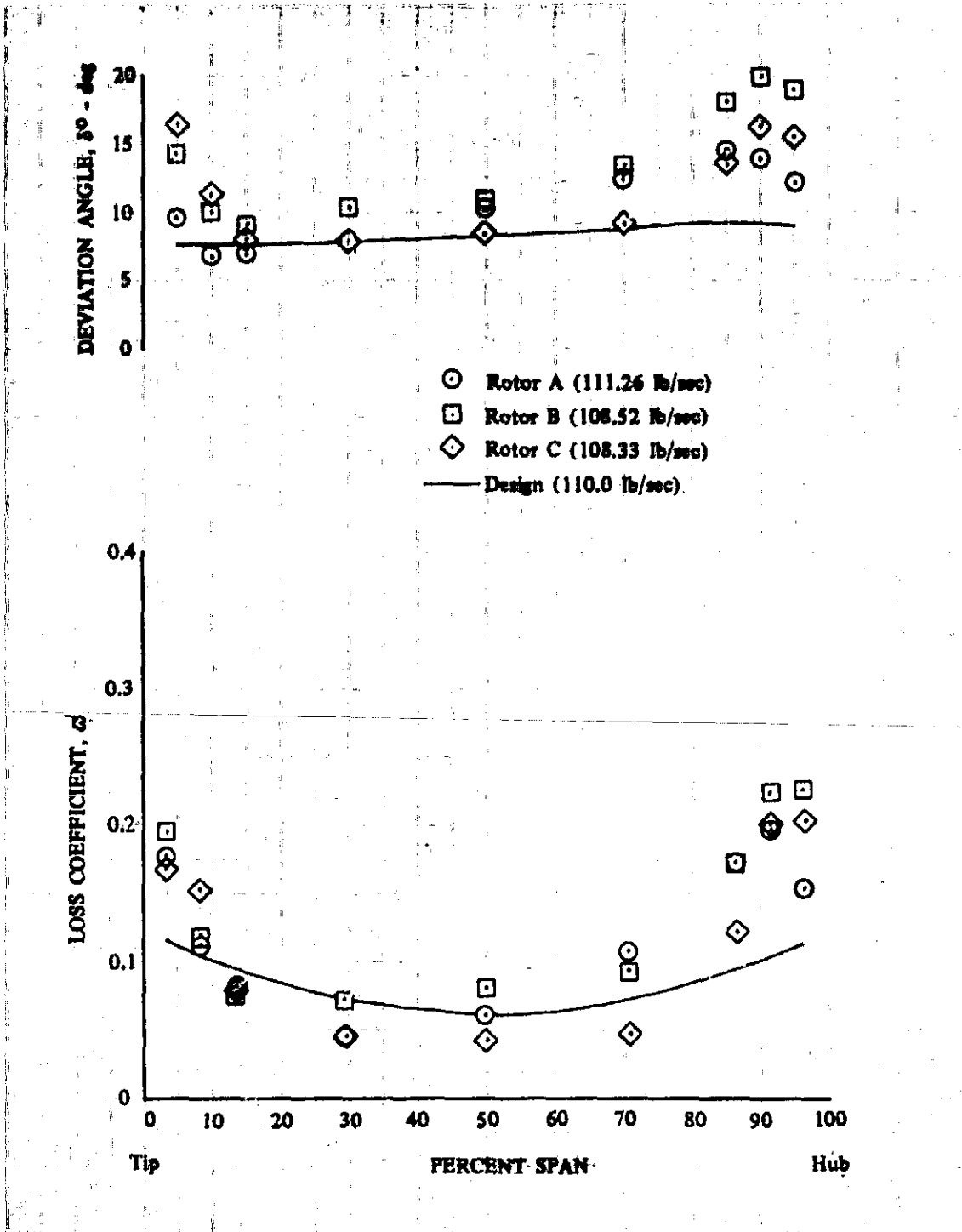
Figure 6. Loss Coefficient and Deviation Angle   DF 100317
vs Percent Span for Rotors A, B, and
C; Design Equivalent Rotor Speed; Near
Design Flow; Uniform Inlet Flow
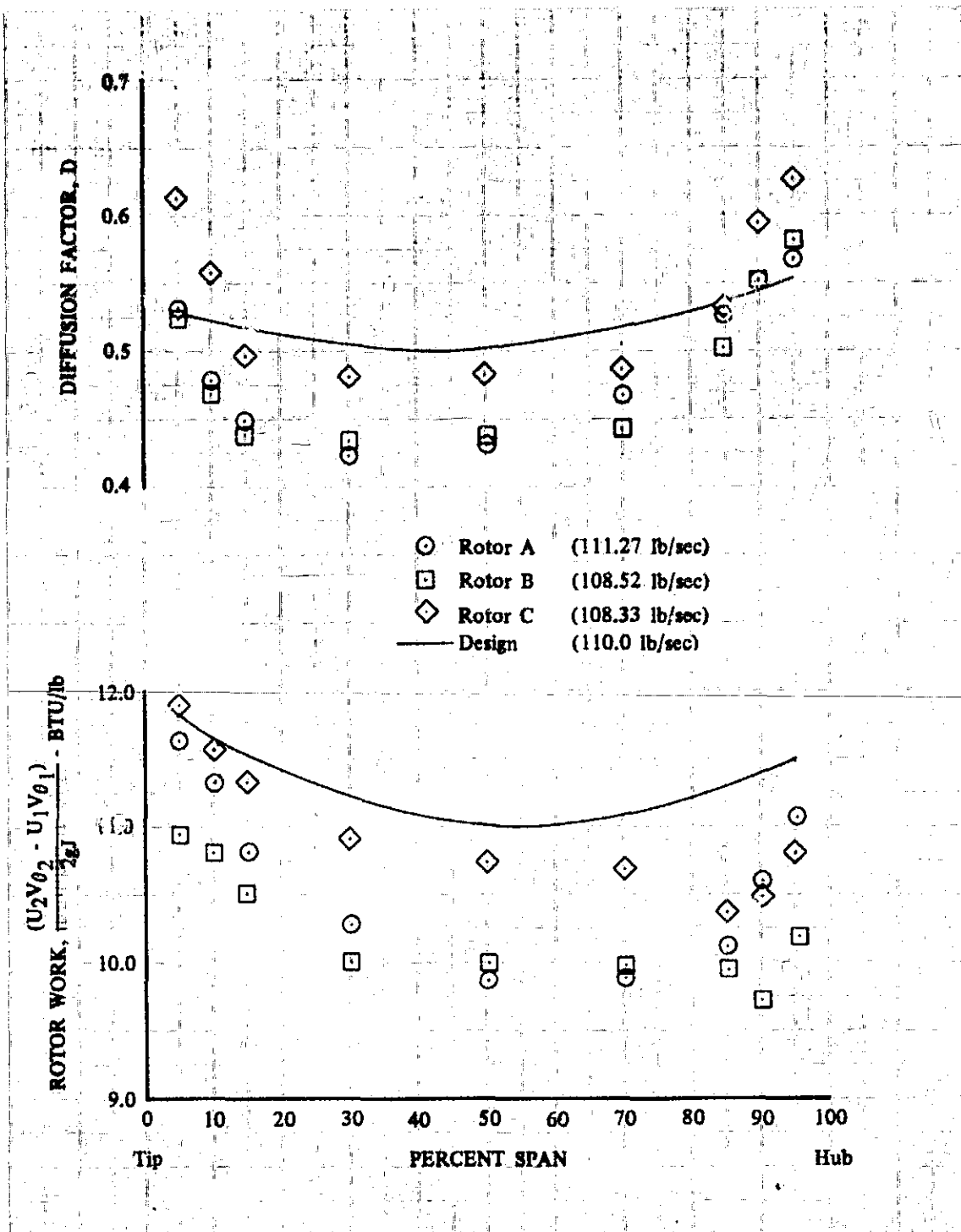
Figure 7. Work Distribution and Diffusion Factor   DF 100318
vs Percent Span for Rotors A, B, and
C; Design Equivalent Rotor Speed and
Flow; Uniform Inlet Flow
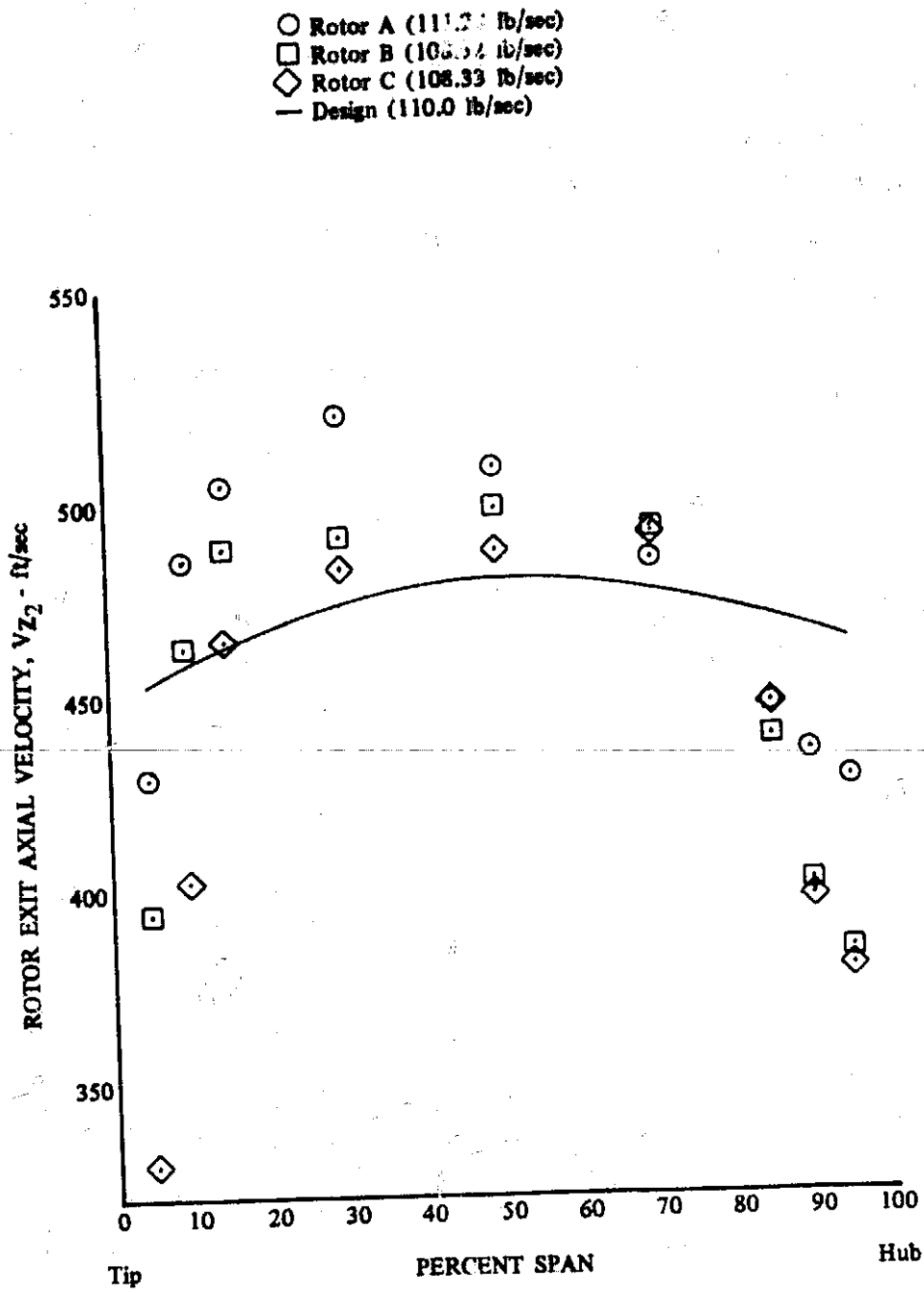
Figure 8. Rotor Exit Axial Velocity vs Percent Span   DF 100319
for Rotors A, B, and C; Design Equiva-
le.t Rotor Speed and Flow; Uniform
Inlet Flow
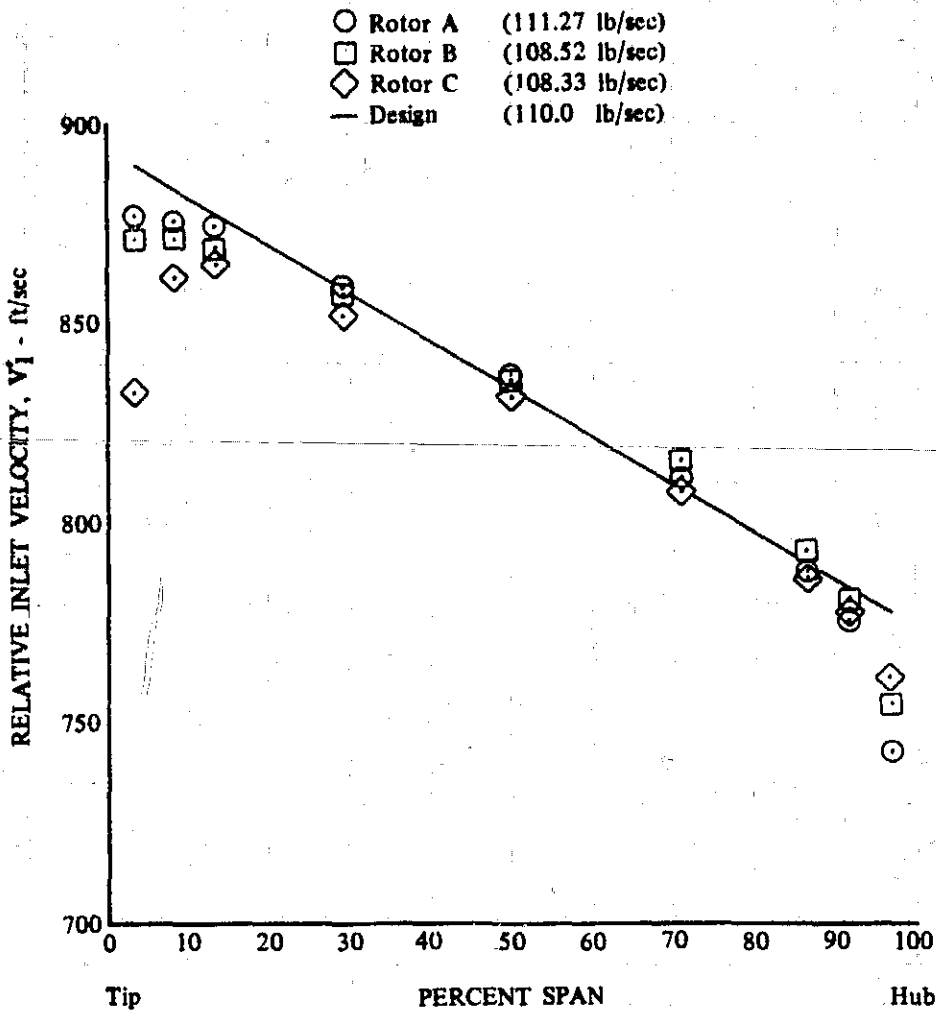
Figure 9. Relative Inlet Velocity vs Percent
Span for Rotors A, B, and C; Design
Equivalent Rotor Speed and Flow; Uniform
Inlet Flow

DF 100320
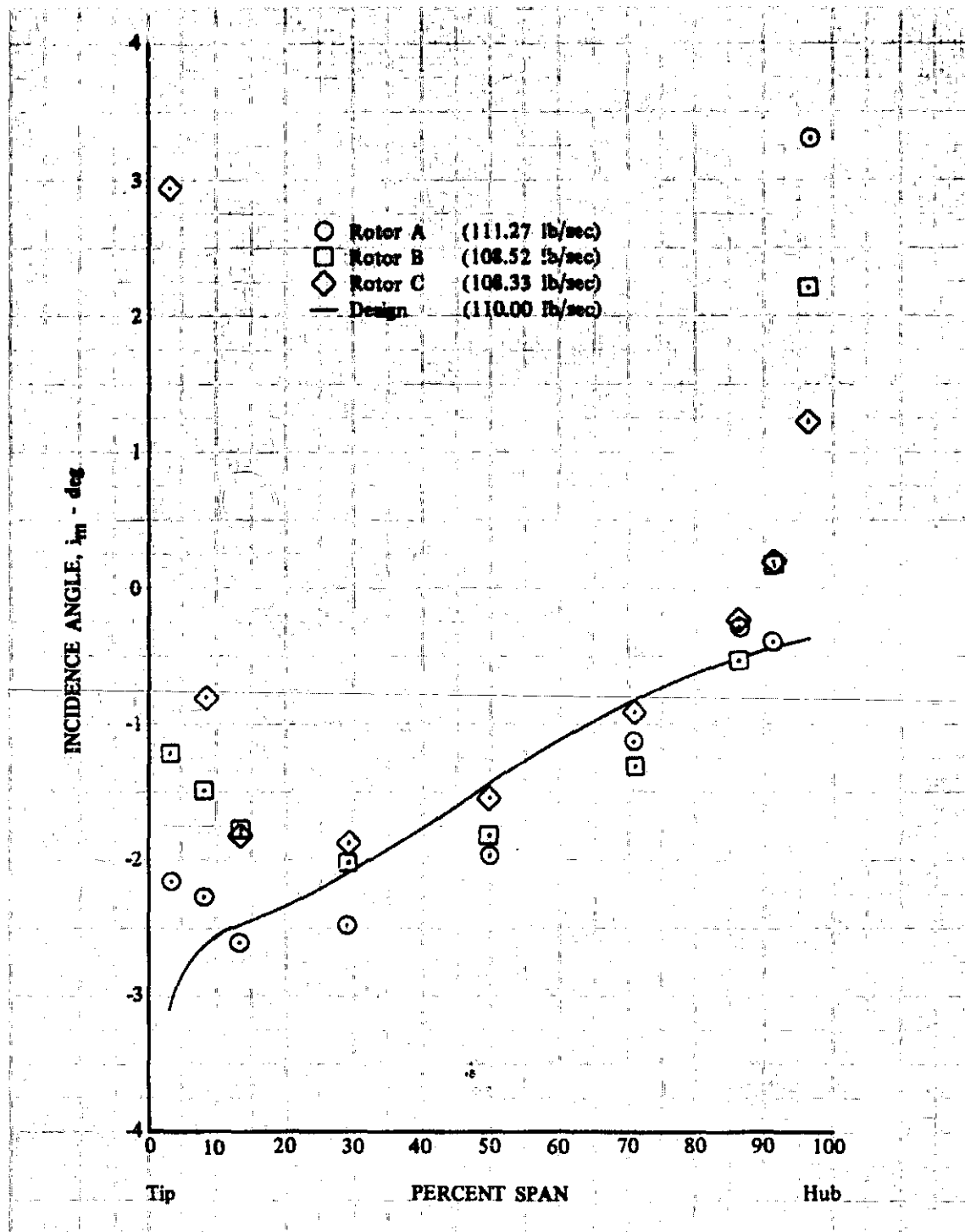
Figure 10. Incidence Angle vs Percent Span for Rotors A, B, and C; Design Equivalent Rotor Speed and Flow; Uniform Inlet Flow

DF 100321
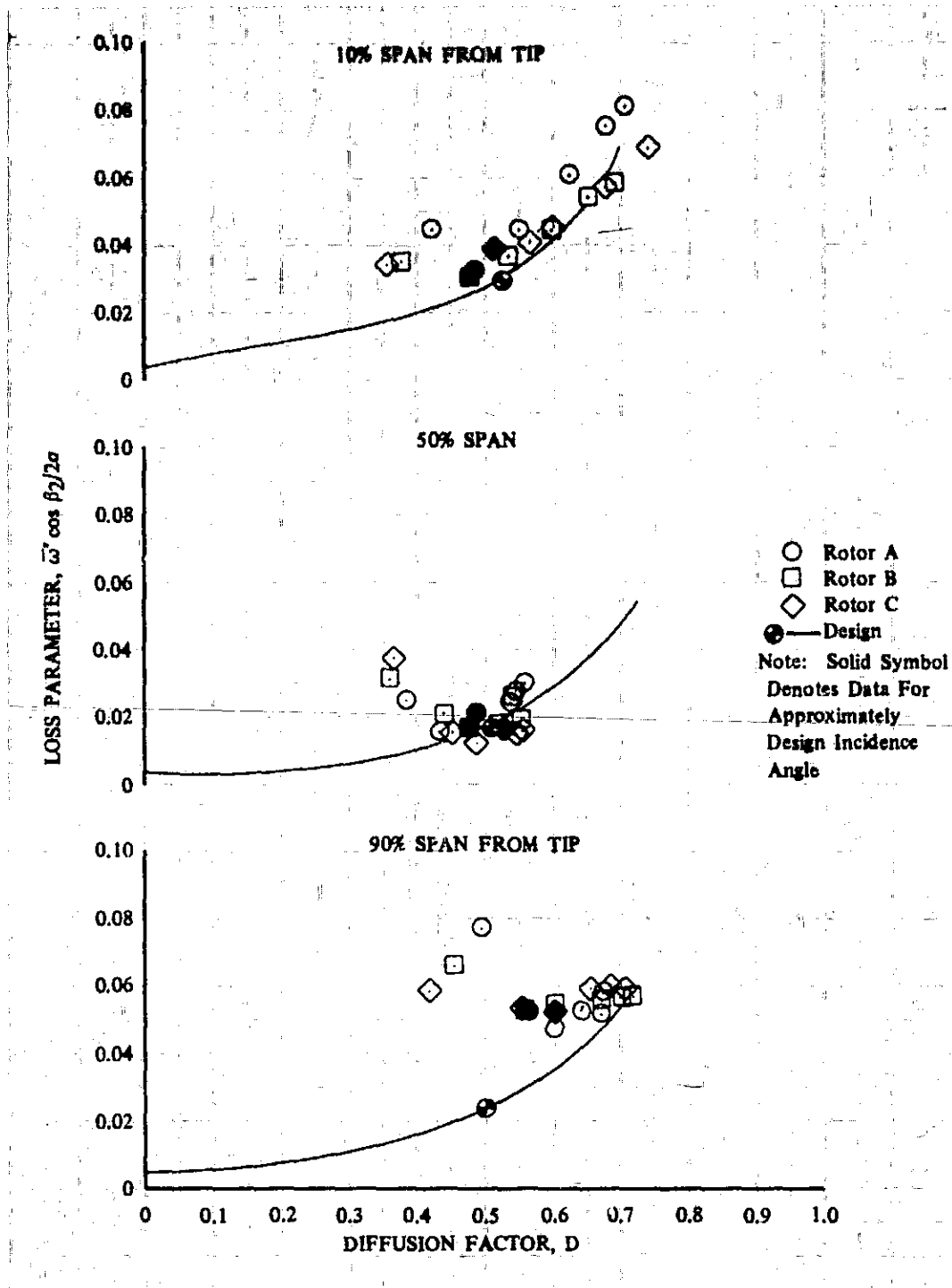
Figure 11. Loss Parameter vs Diffusion
Factor for Rotors A, B, and C;
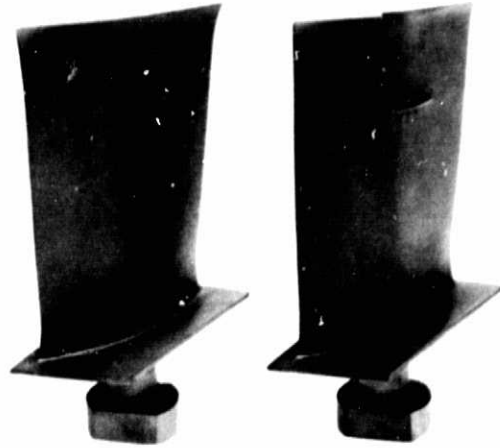Design Equivalent Rotor Speed;
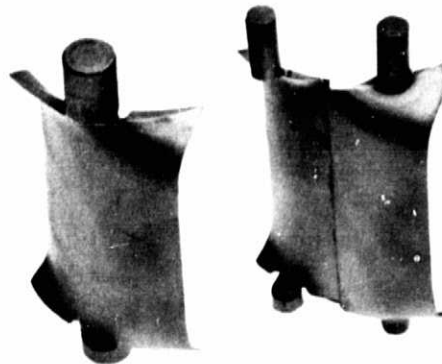Uniform Inlet Flow

DF 100322
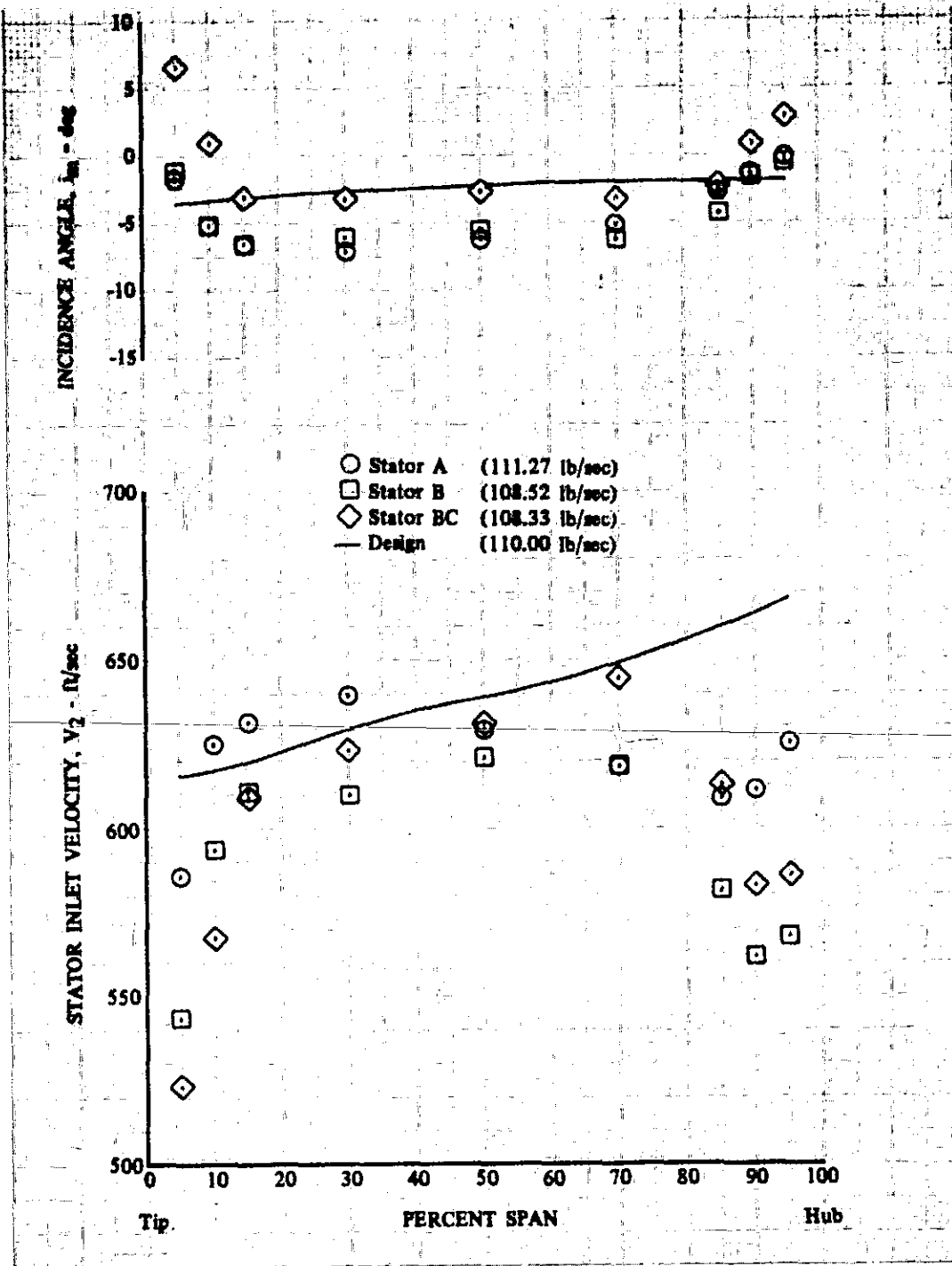
Figure 12. Inlet Velocity and Incidence Angle
vs Percent Span for Stators A, B,
and BC; Design Equivalent Rotor Speed
and Flow; Uniform Inlet Flow

DF 100323
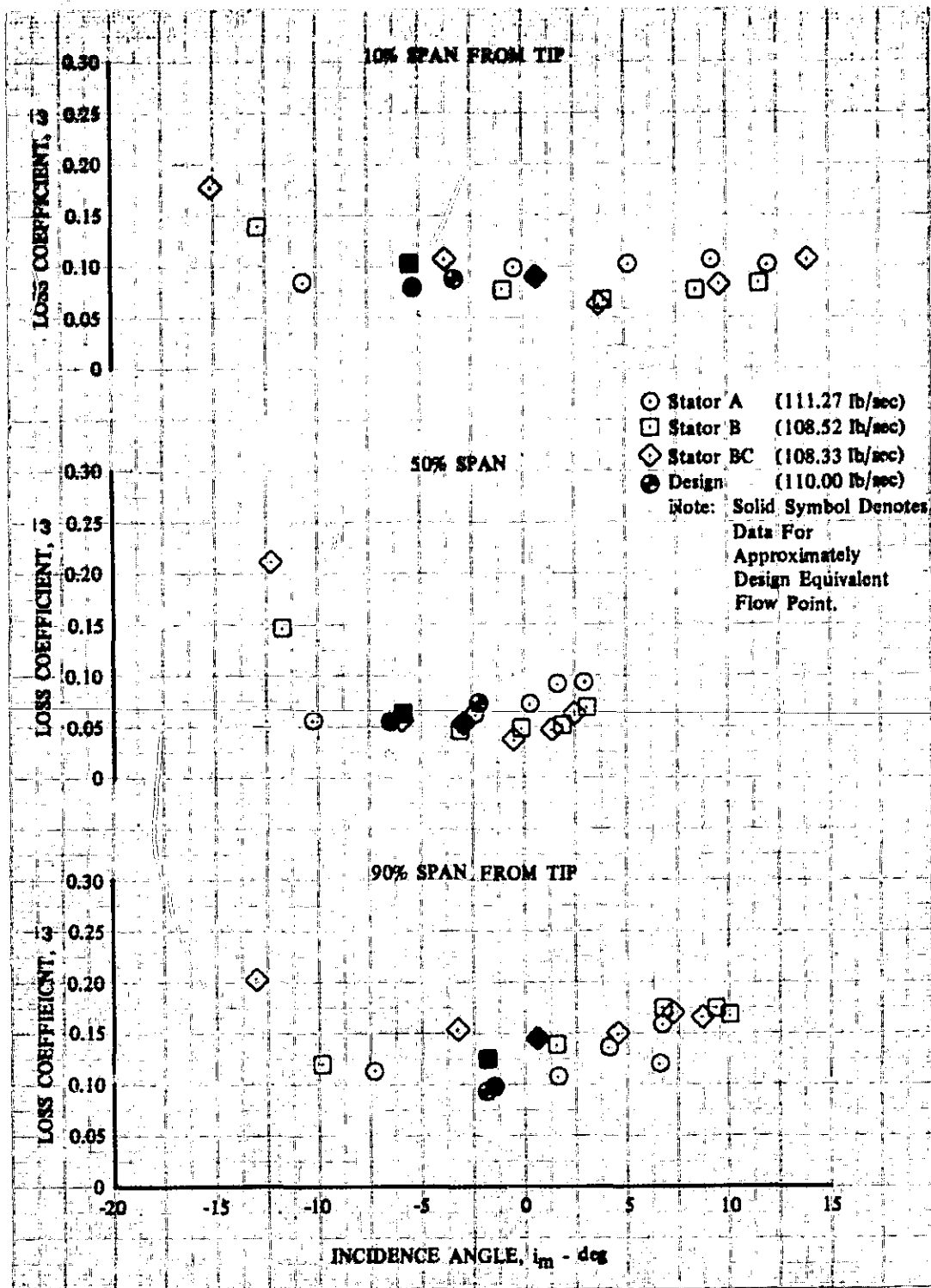
Figure 13. Loss Coefficient vs Incidence Angle for Stators A, B, and BC; 10, 50, and 90% Span From Tip; Uniform Inlet Flow

DF 100324

38
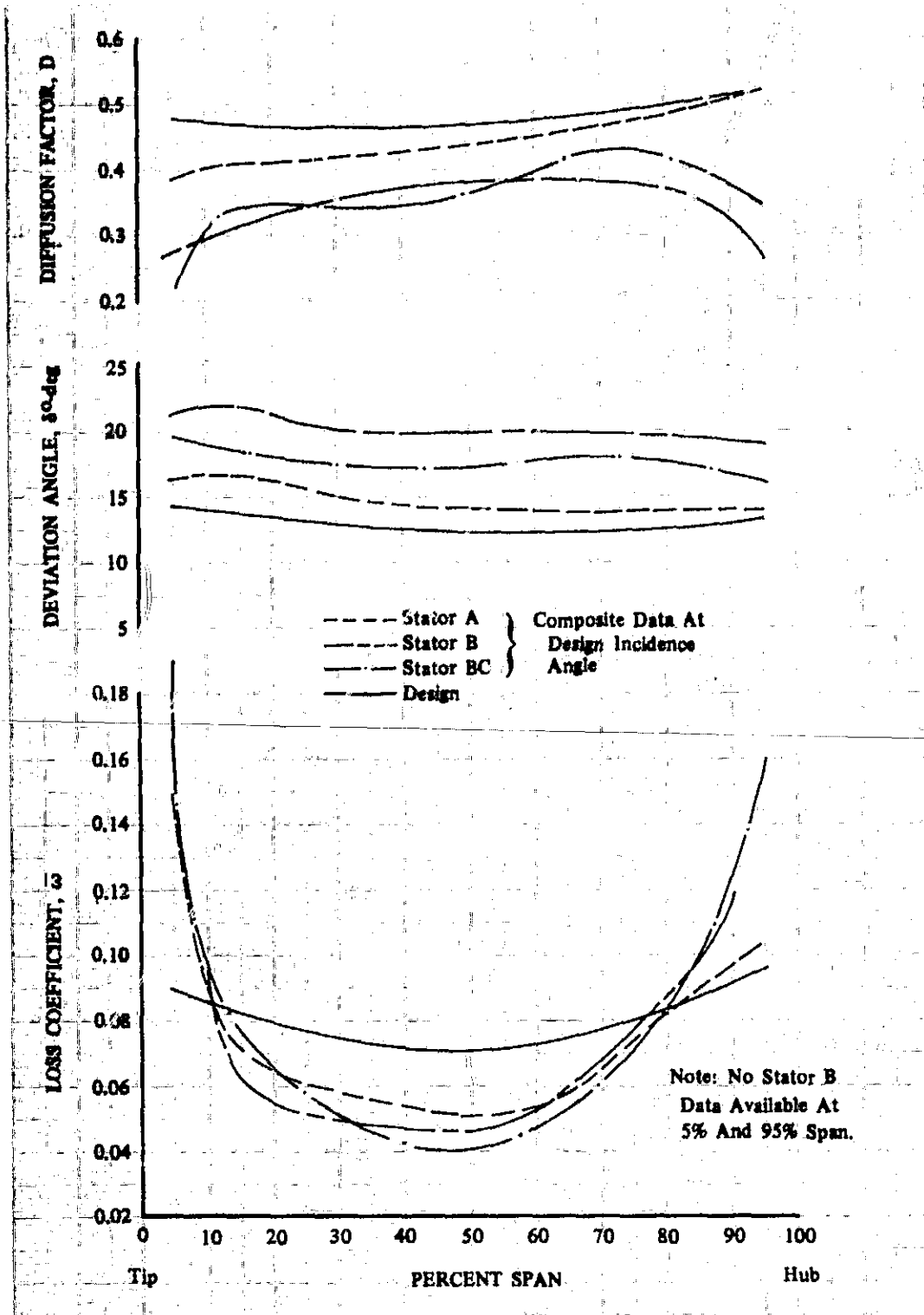
Figure 14. Loss Coefficient, Deviation Angle, and
Diffusion Factor at Design Incidence
Angle vs Percent Span for Stators A,
B, and BC; Design Equivalent Rotor
Speed; Uniform Inlet Flow

DF 100325
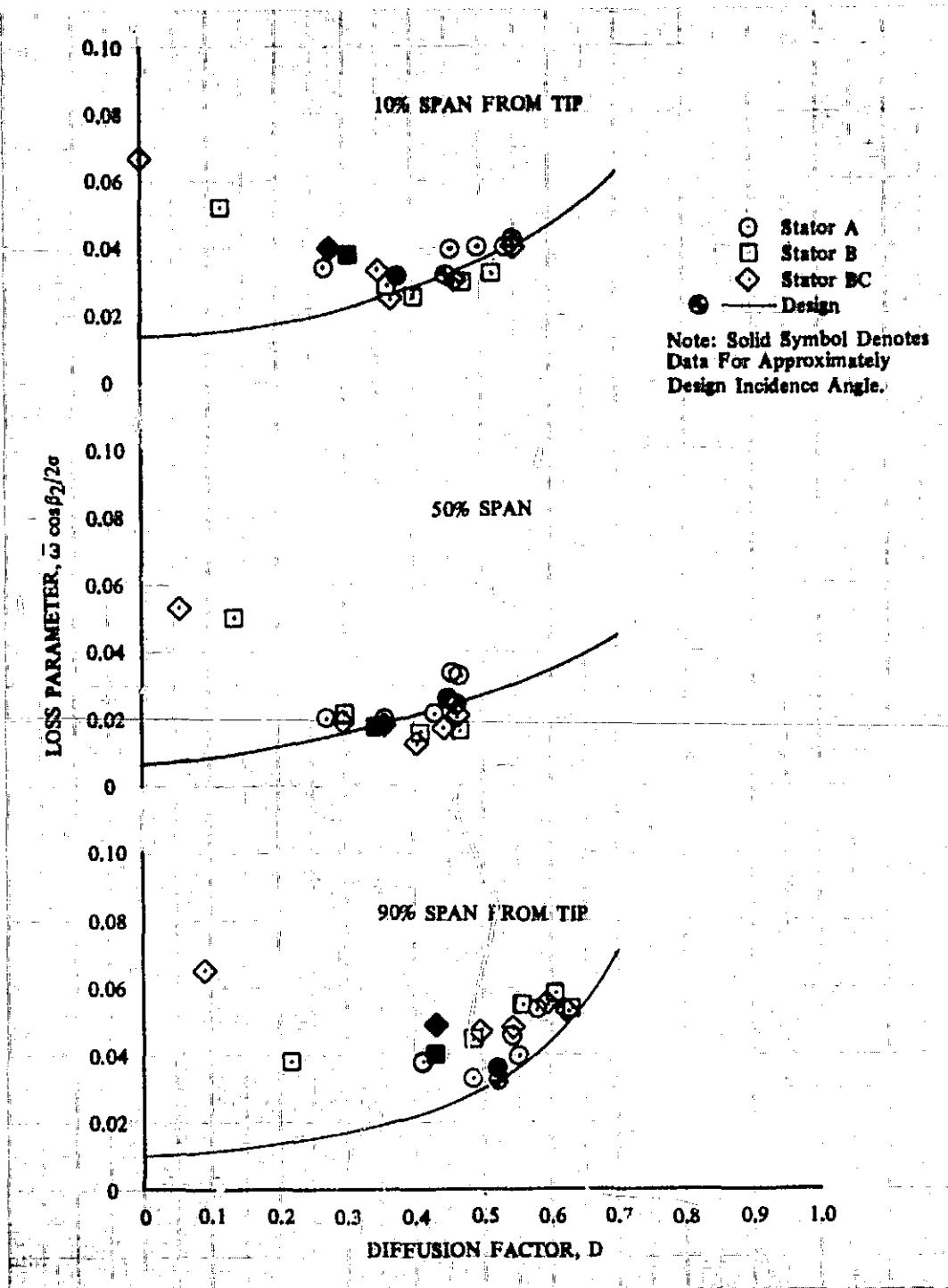
Figure 15. Loss Parameter vs Diffusion Factor
for Stators A, B, and BC; Design
Equivalent Rotor Speed; Uniform Inlet
Flow

DF 100326

40

Figure 16. Rotor D and E Blading   FAE 133394

Figure 17. Stator D and E Blading   FAE 133397
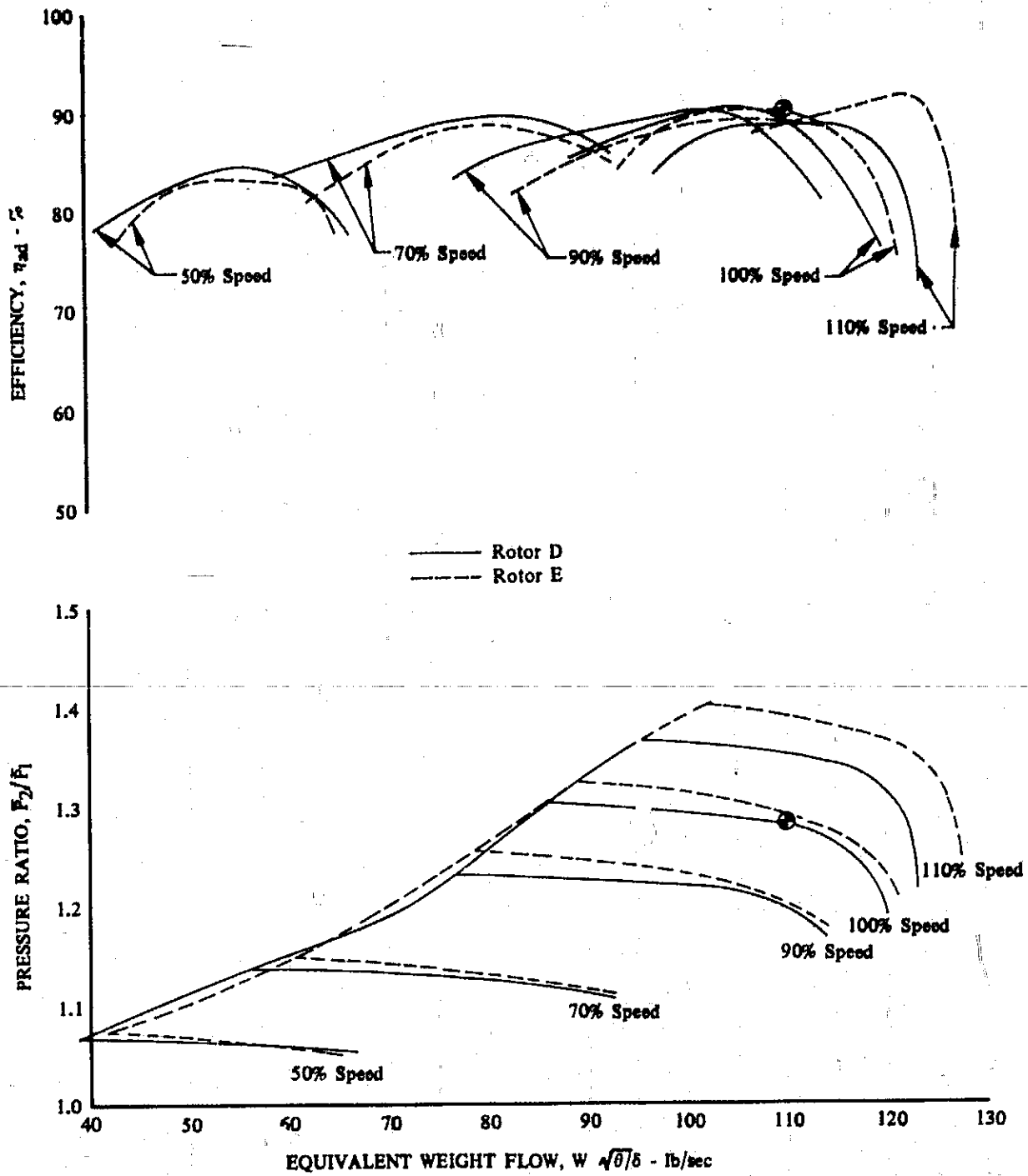
Figure 18. Overall Performance of Rotors D
and E; Uniform Inlet Flow

DF 100327
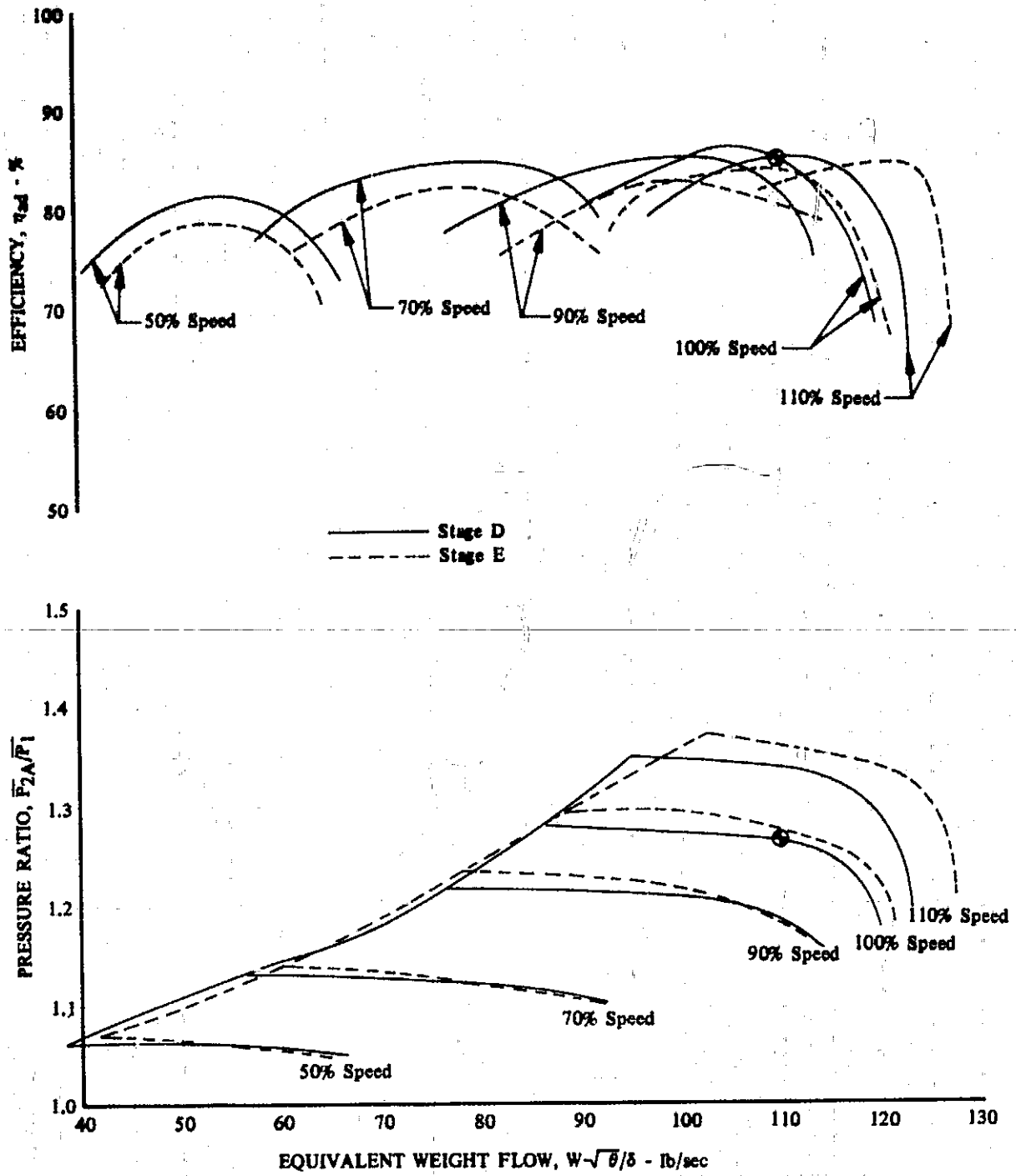
Figure 19. Overall Performance of Stages D and E; Uniform Inlet Flow   DF 100328
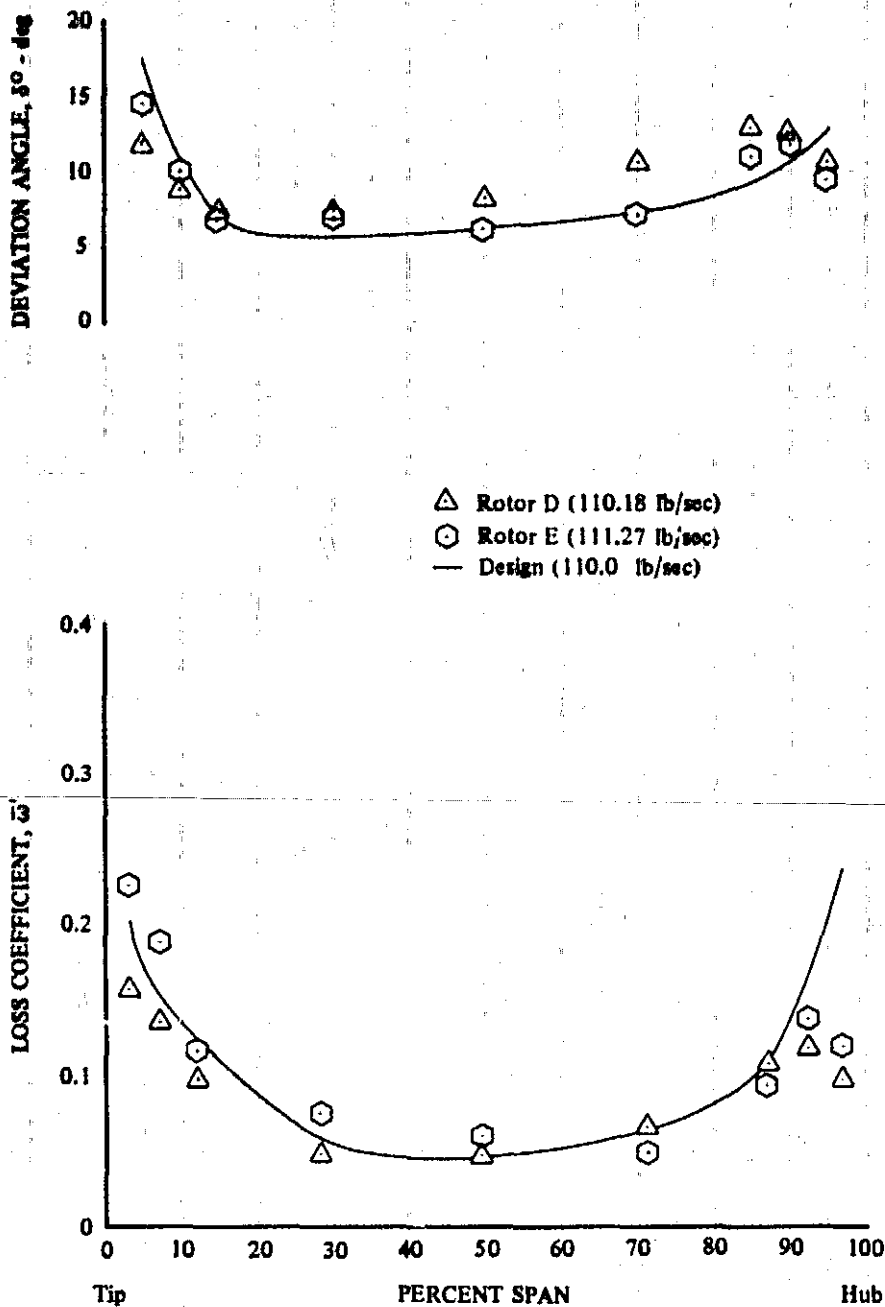
Figure 20. Loss Coefficient and Deviation Angle
vs Percent Span for Rotors D and
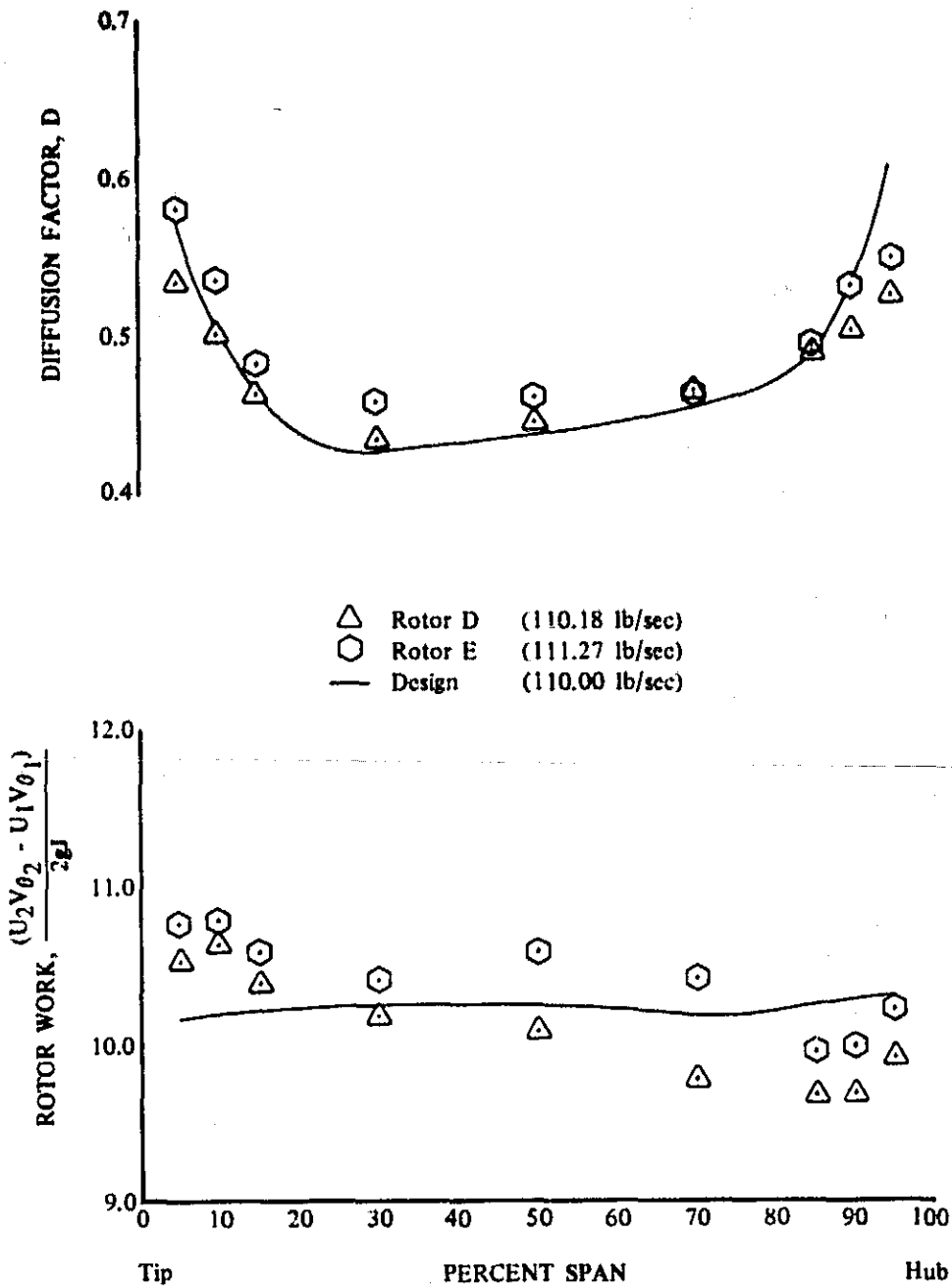E; Design Equivalent Rotor Speed and
Flow; Uniform Inlet Flow

DF 100329

Figure 21. Work Distribution and Diffusion Factor   DF 100330
            vs Percent Span for Rotors D and E;
            Design Equivalent Rotor Speed and
            Flow; Uniform Inlet Flow

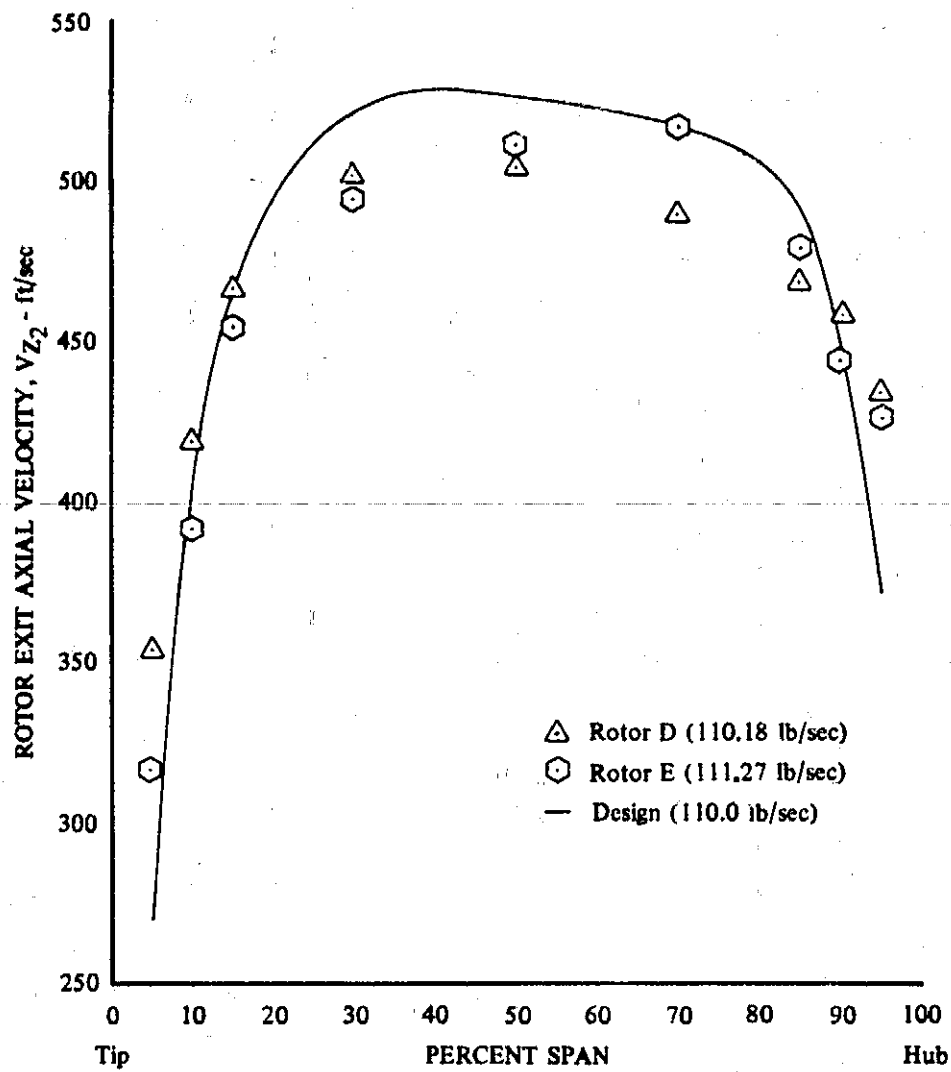Figure 22.   Exit Axial Velocity vs Percent Span   DF 100331
             for Rotors D and E; Design Equivalent
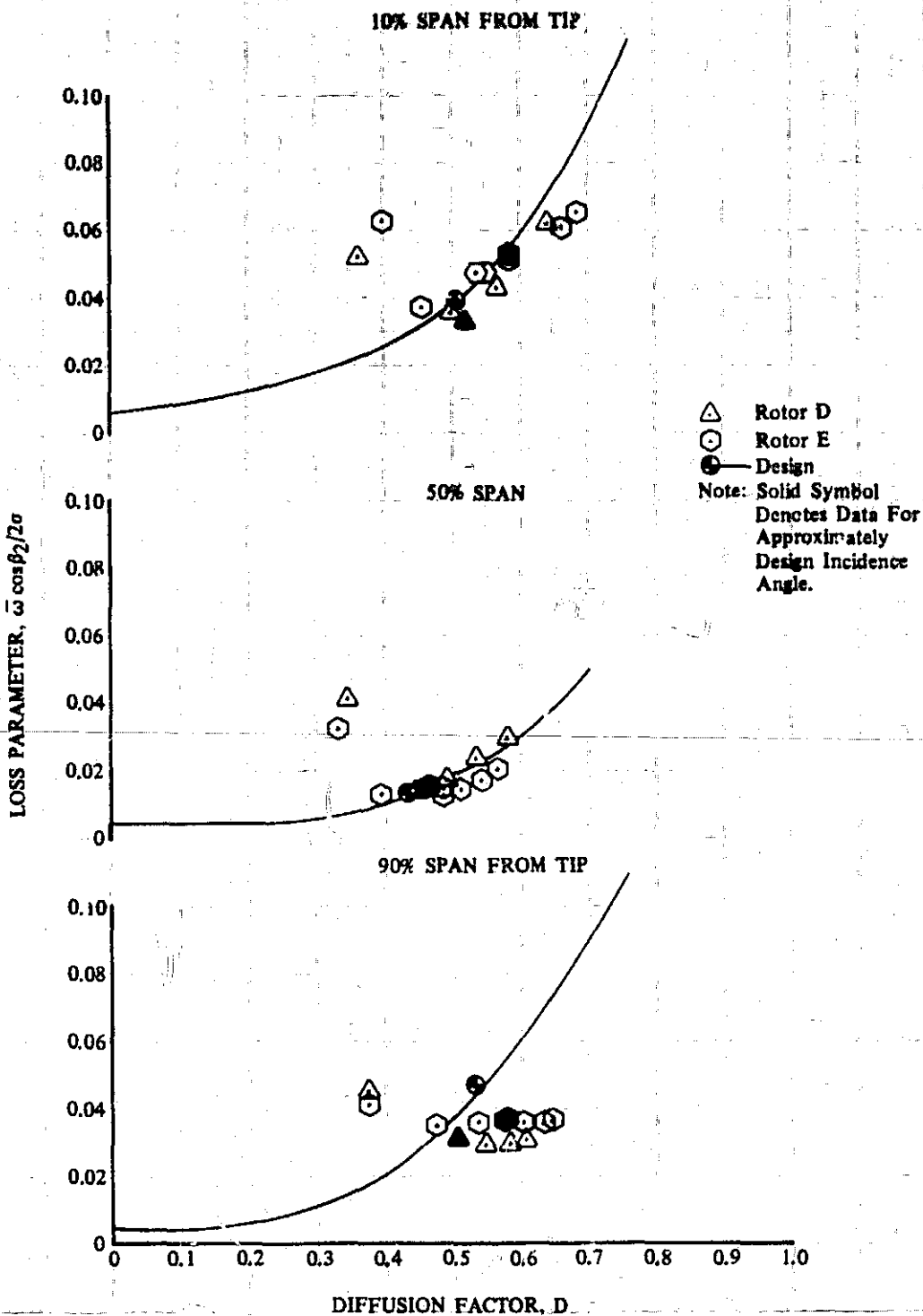   Rotor Speed and Flow; Uniform Inlet
             Flow

Figure 23. Loss Parameter vs Diffusion Factor
for Rotors D and E; Design Equivalent
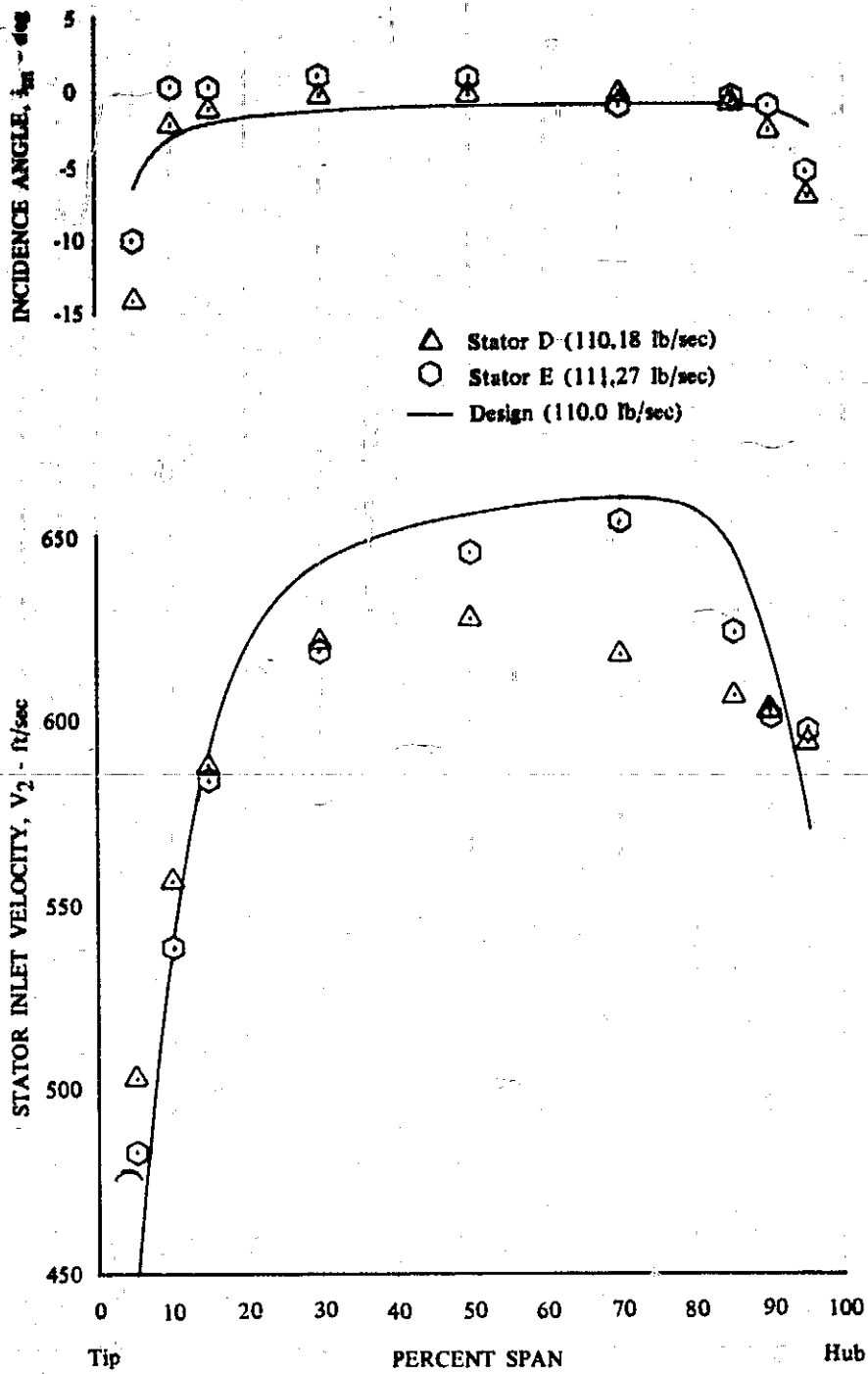Rotor Speed; Uniform Inlet Flow

DF 100332

Figure 24. Inlet Velocity and Incidence Angle vs
Percent Span for Stators D and E;
Near Design Equivalent Rotor Speed
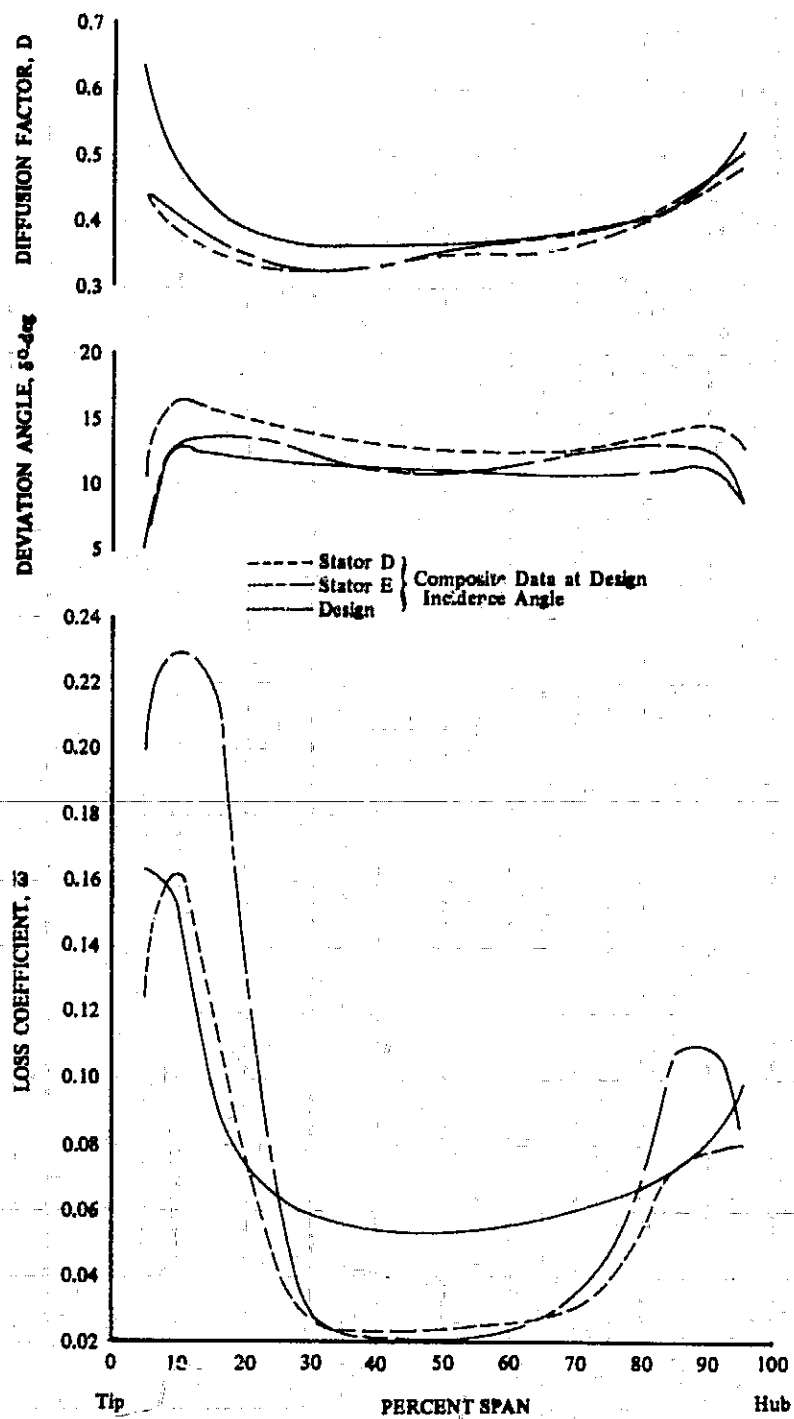and Flow; Uniform Inlet Flow

DF 100333

Figure 25. Loss Coefficient, Deviation Angle, and   DF 100334
Diffusion Factor at Design Incidence
Angle vs Percent Span for Stators D
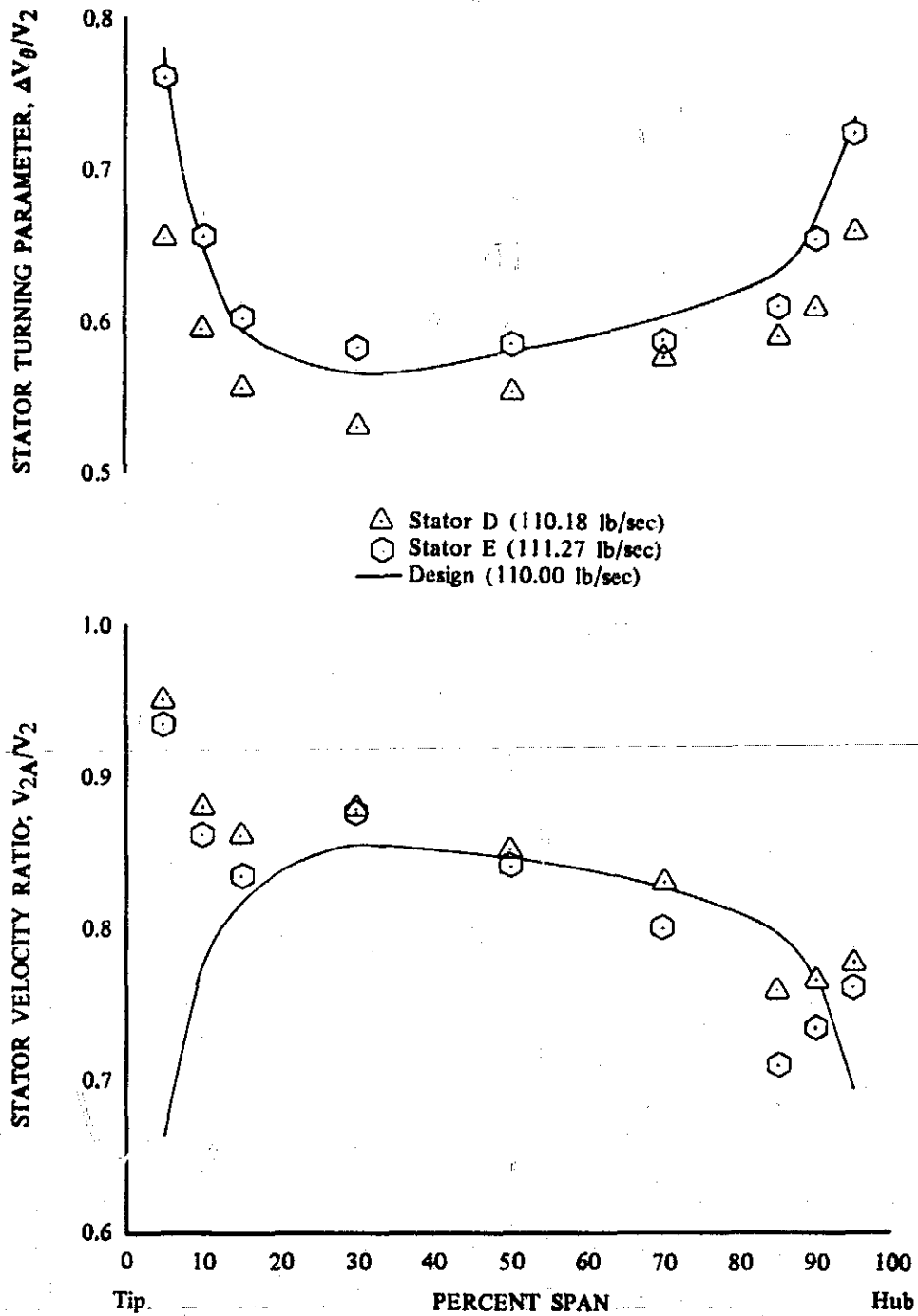and E at Design Equivalent Rotor Speed;
Uniform Inlet Flow

Figure 26. Velocity Ratio and Turning vs Percent   DF 100335
Span for Stators D and E; Near Design
Equivalent Rotor Speed and Flow;
Uniform Inlet Flow
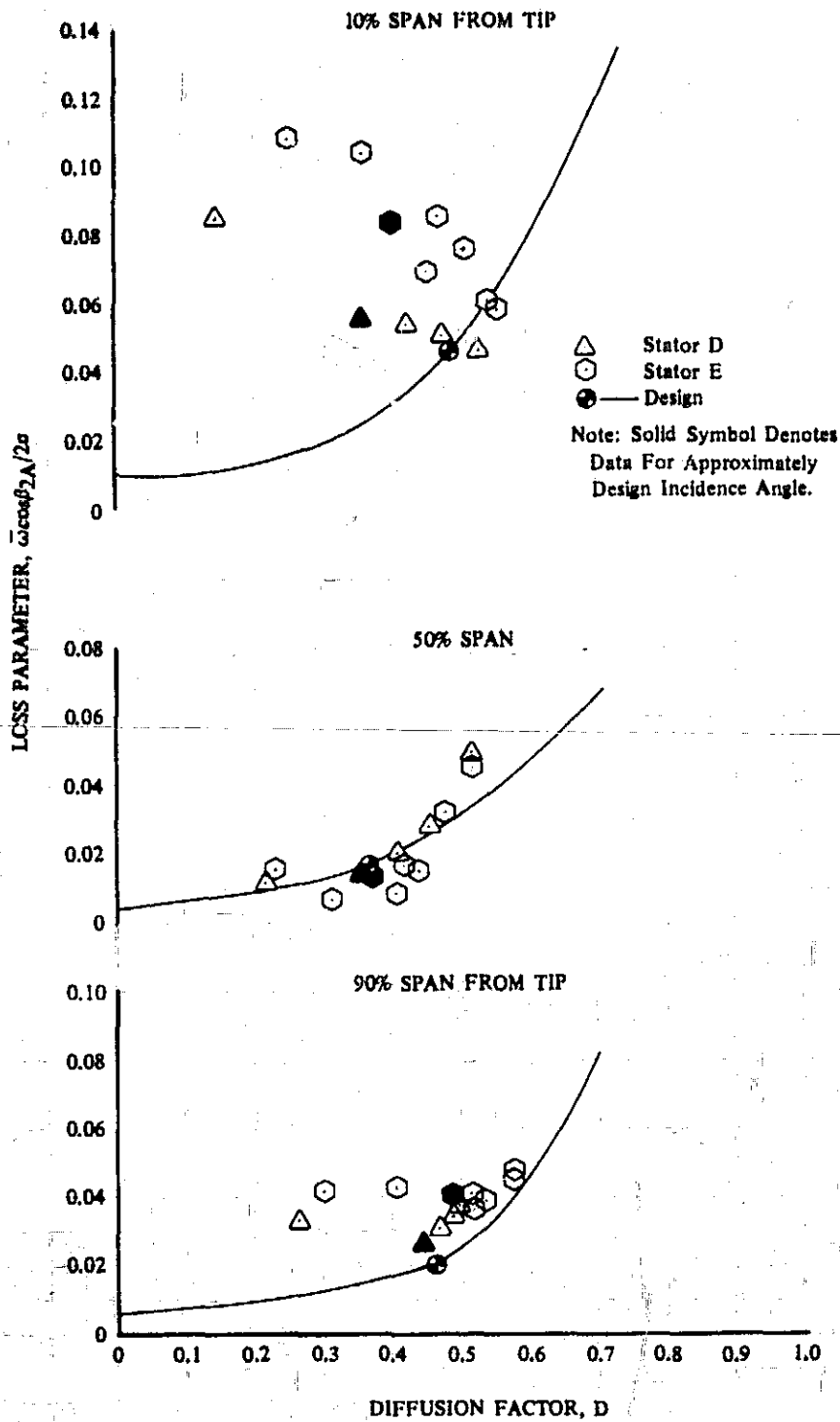
Figure 27. Loss Parameter vs Diffusion Factor for DF 100336
Stators D and E; Design Equivalent Rotor
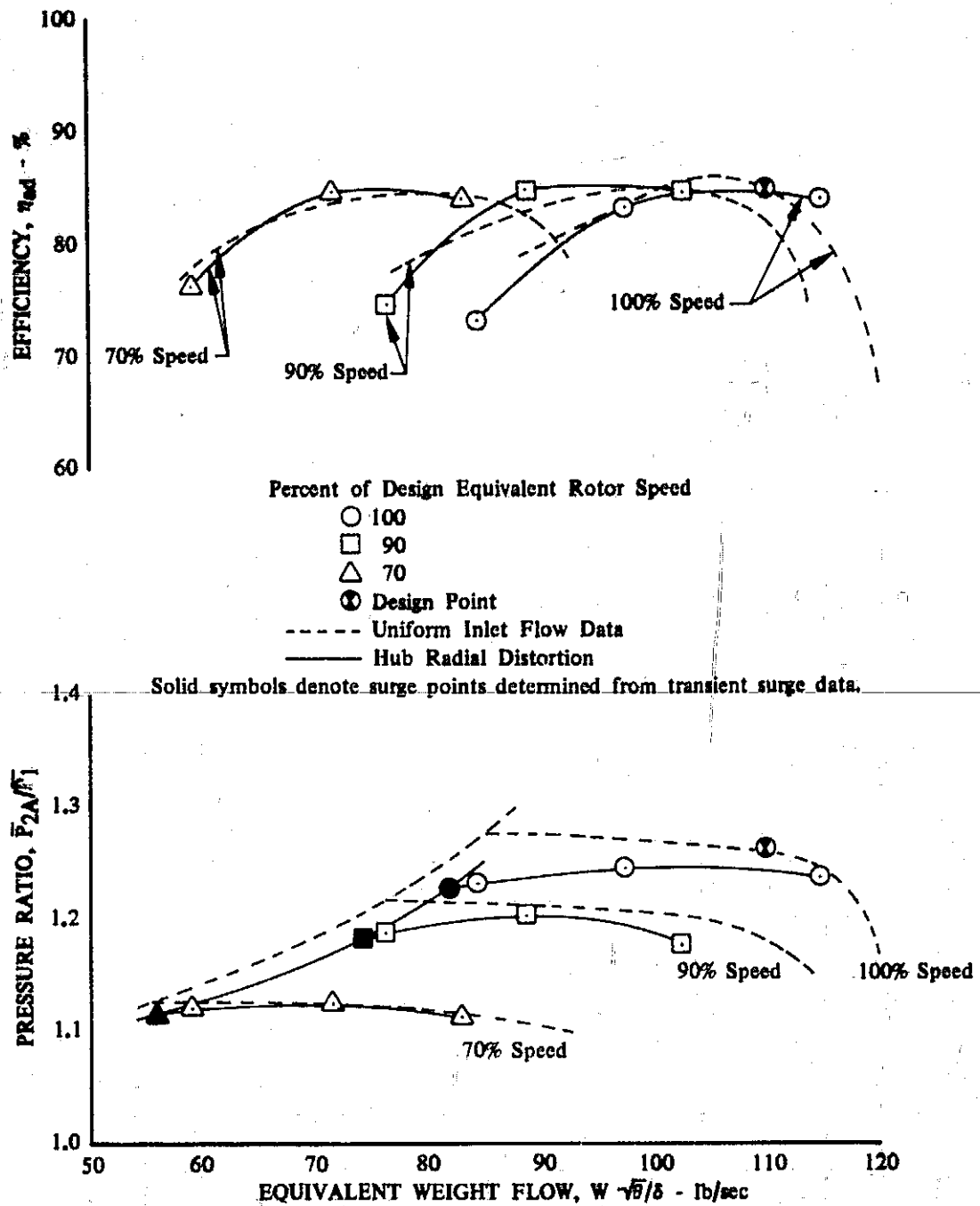Speed; Uniform Inlet Flow

Figure 28. Overall Performance of Stage D; Hub   DF 97733
Radial Distortion Compared with
Uniform Inlet Flow
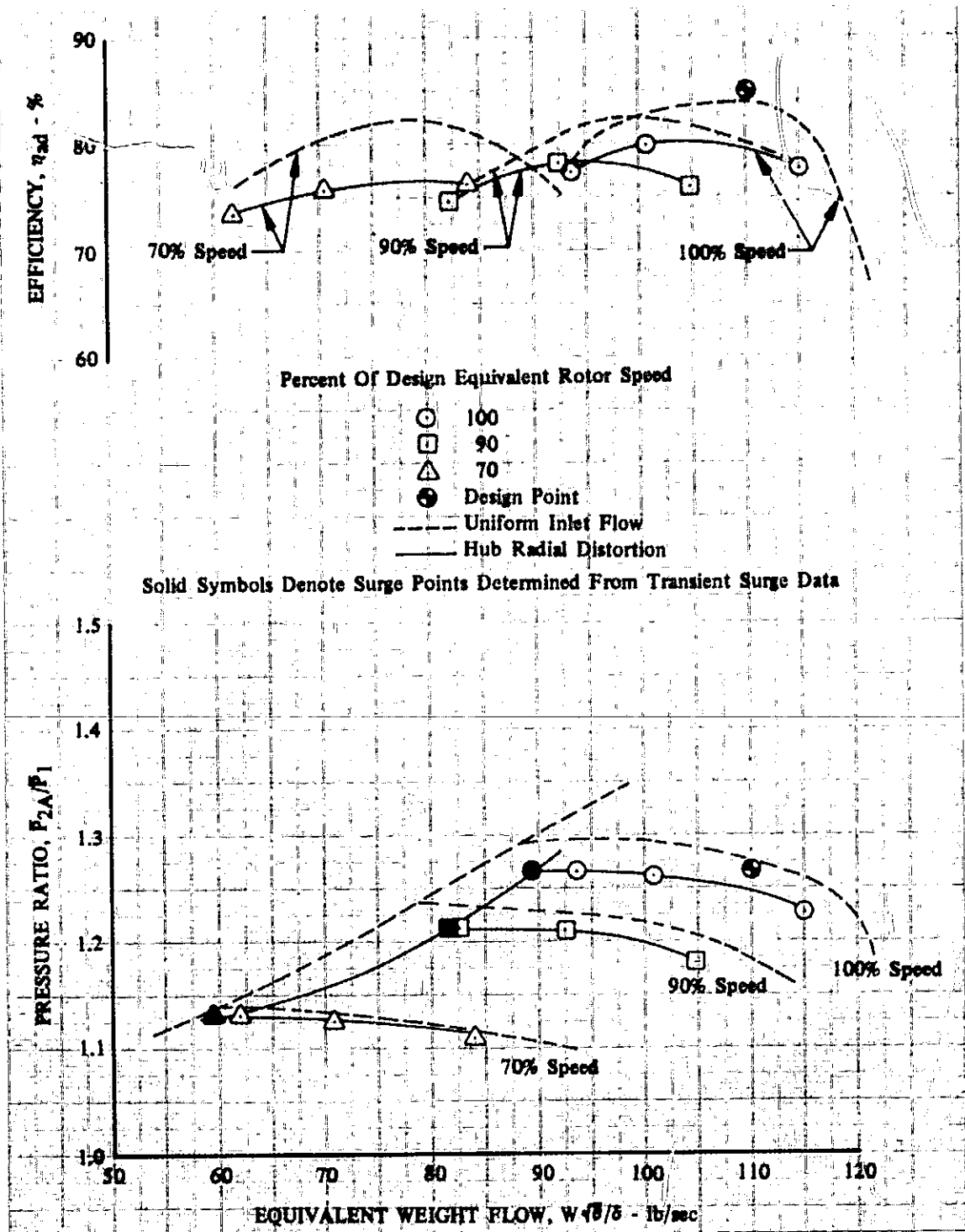
Figure 29.   Overall Performance of Stage E;   DF 100337
             Hub Radial Distortion Compared to
             Uniform Inlet Flow
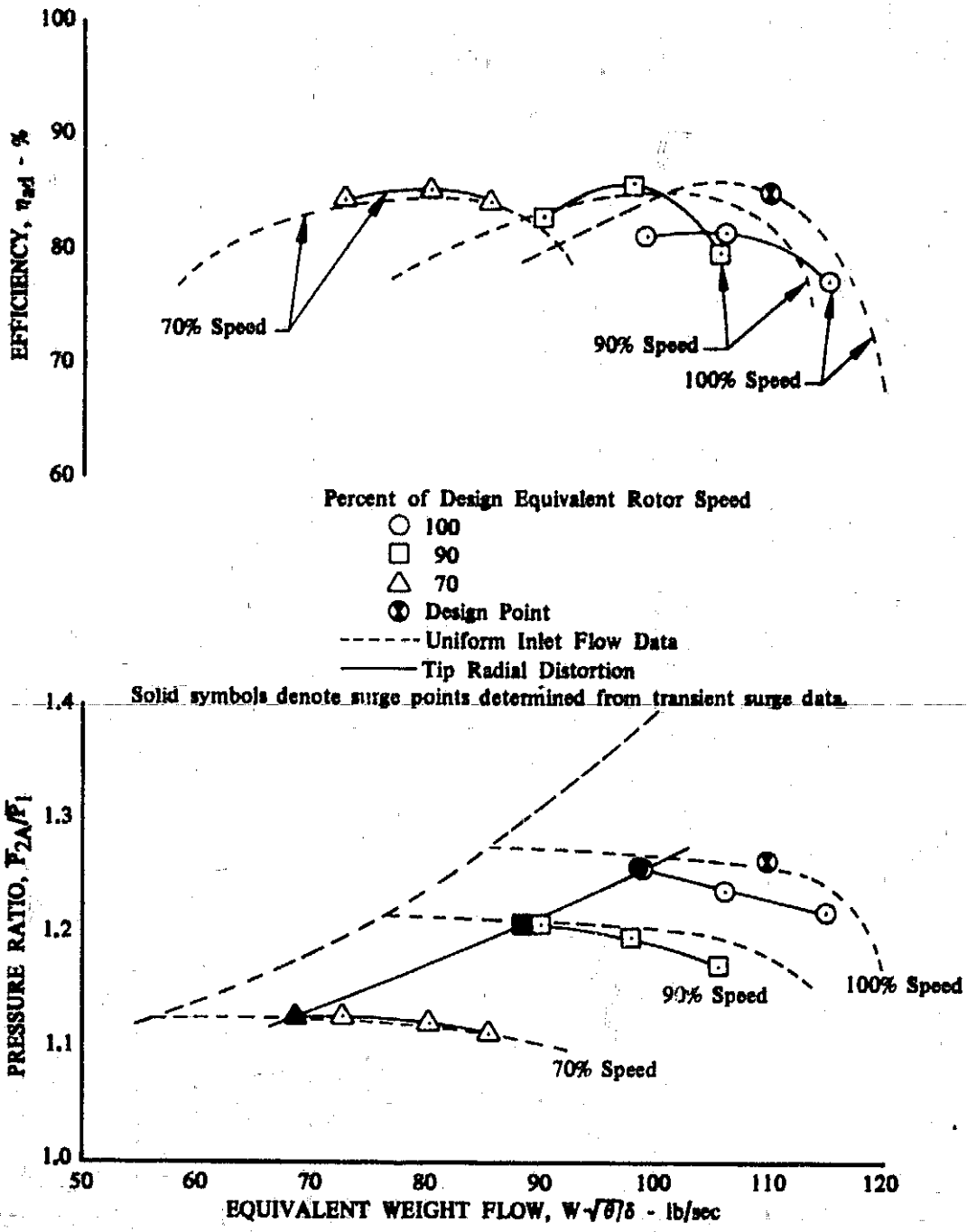
Figure 30. Overall Performance of Stage D; Tip   DF 97735
Radial Distortion Compared with
Uniform Inlet Flow
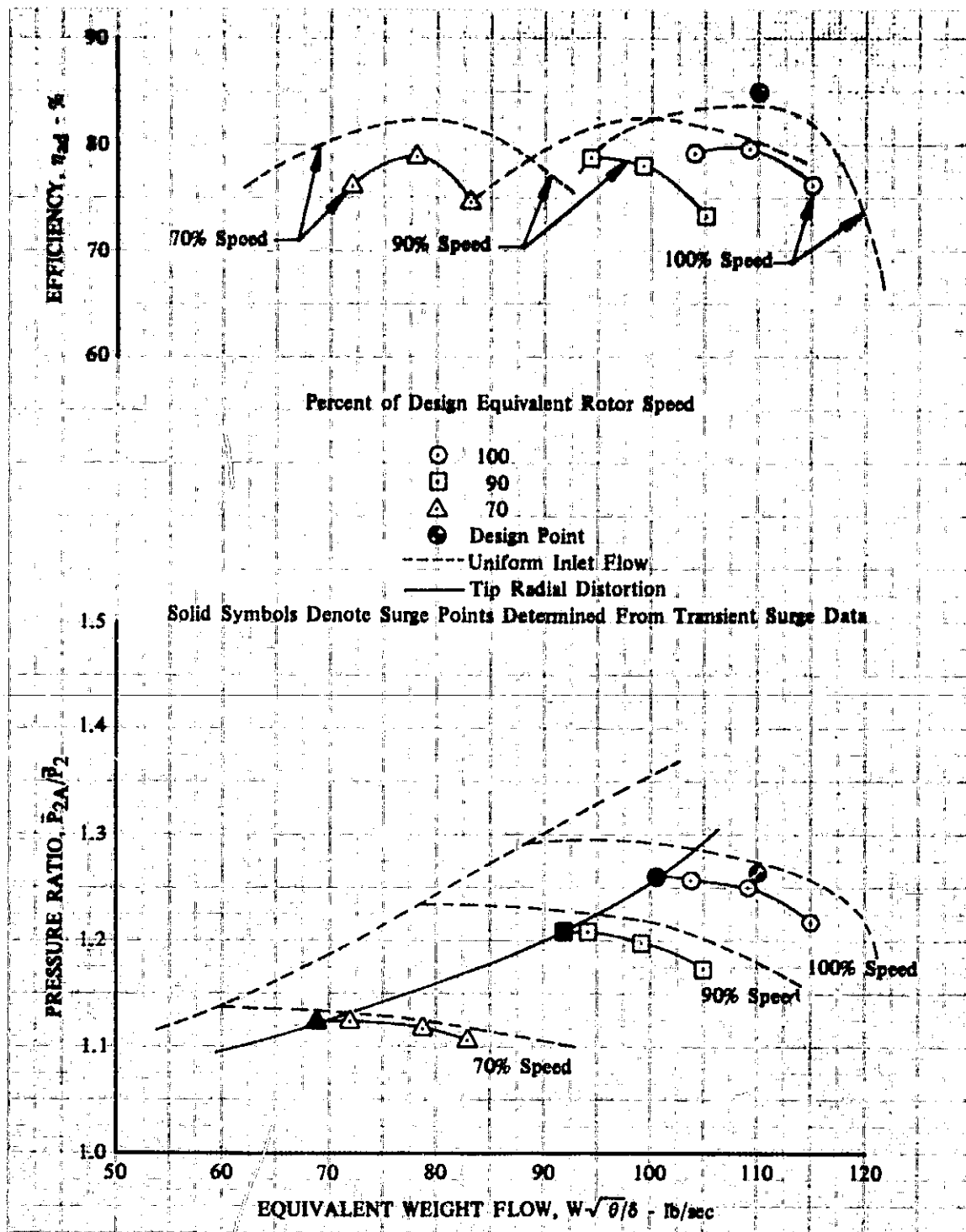
Figure 31. Overall Performance of Stage E; Tip
Radial Distortion Compared to Uniform
Inlet Flow

DF 100338

Figure 32. Local Distortion Parameter vs Instru-   DF 100339
mentation Location for Stage D; Design
Equivalent Rotor Speed; Maximum and
Near Surge Flow; Hub and Tip Radial
Distortion

Figure 33. Local Distortion Parameter vs Instru-
mentation Location for Stage E; Design
Equivalent Rotor Speed; Maximum and
Near Surge Flow; Hub and Tip Radial
Distortion

DF 100340

57
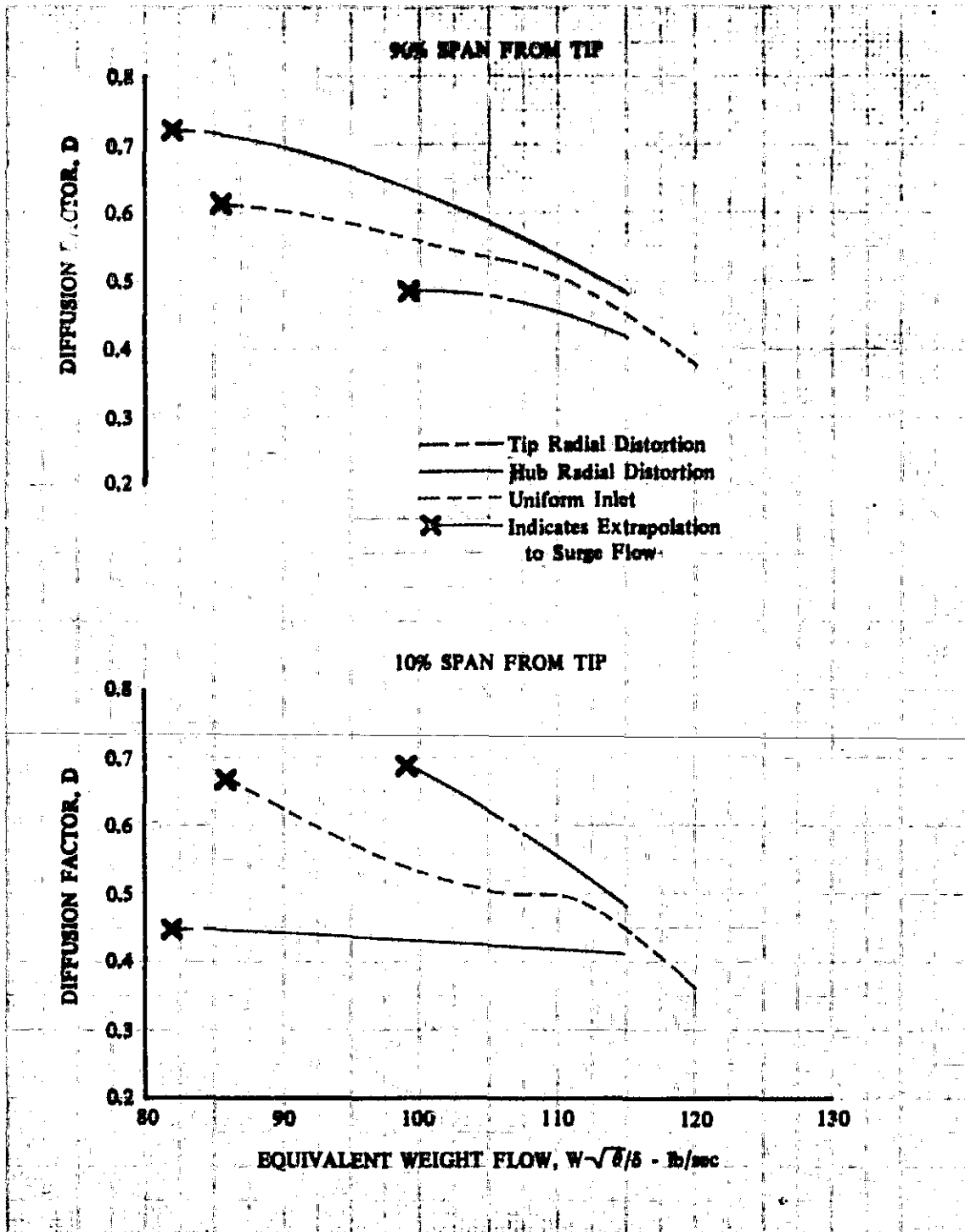
Figure 34. Diffusion Factor vs Equivalent Weight Flow for Stage D; Design Equivalent Rotor Speed; 10 and 90% Span From Tip; Hub and Tip Radial Distortion and Uniform Inlet Flow

DF 100341

58
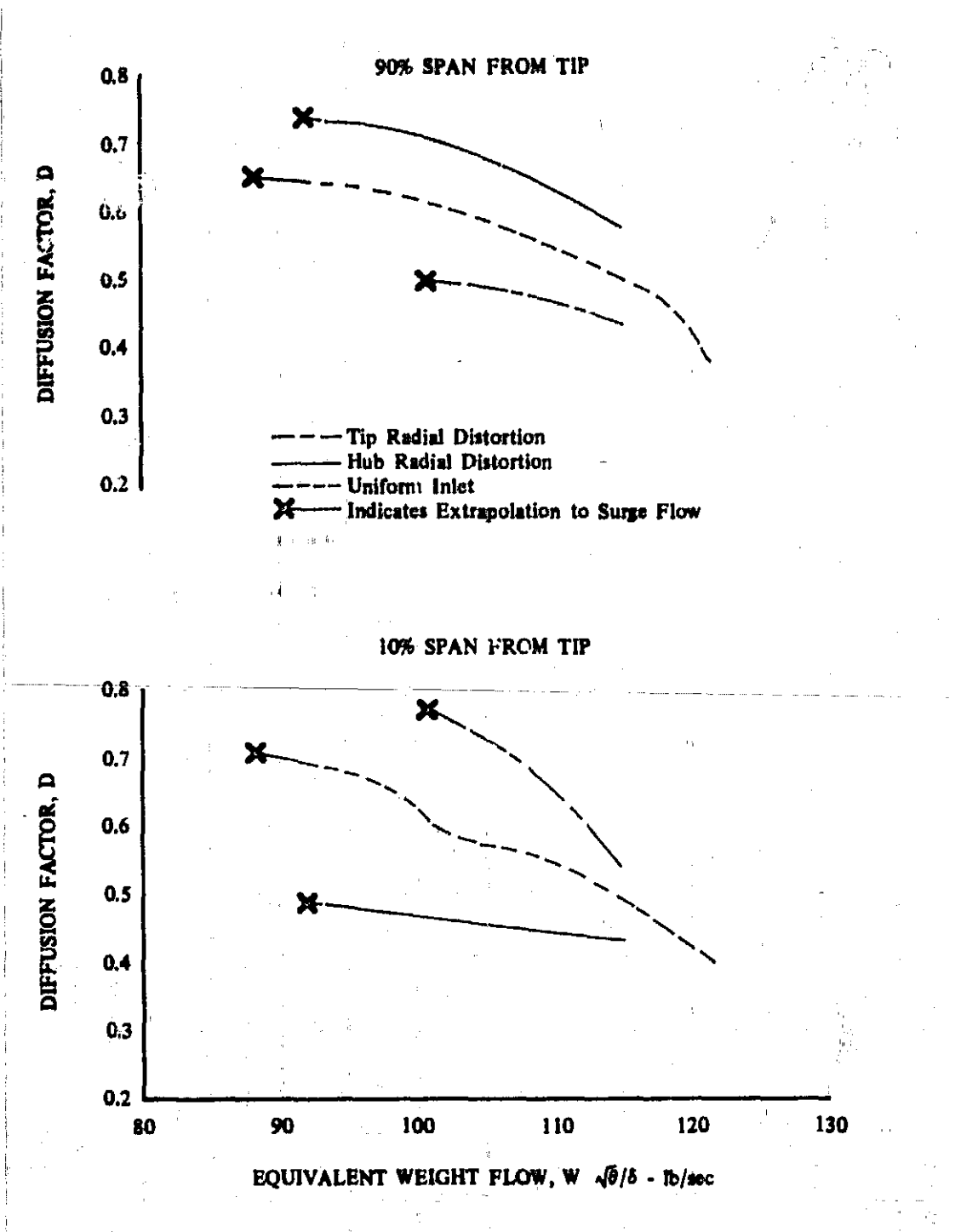
Figure 35. Diffusion Factor vs Equivalent Weight
Flow for Stage E; Design Equivalent
Rotor Speed; 10 and 90% Span From
Tip; Hub and Tip Radial Distortion
and Uniform Inlet Flow

DF 100342

Percent of Design Equivalent Rotor Speed

○ 100
□ 90
△ 70
◐ Design Point
- - - - - Uniform Inlet Flow Data
——— 90-deg Circumferential Distortion

Half-solid symbols denote conditions at which flow distribution data were recorded.
Solid symbols denote surge points determined from transient surge data.
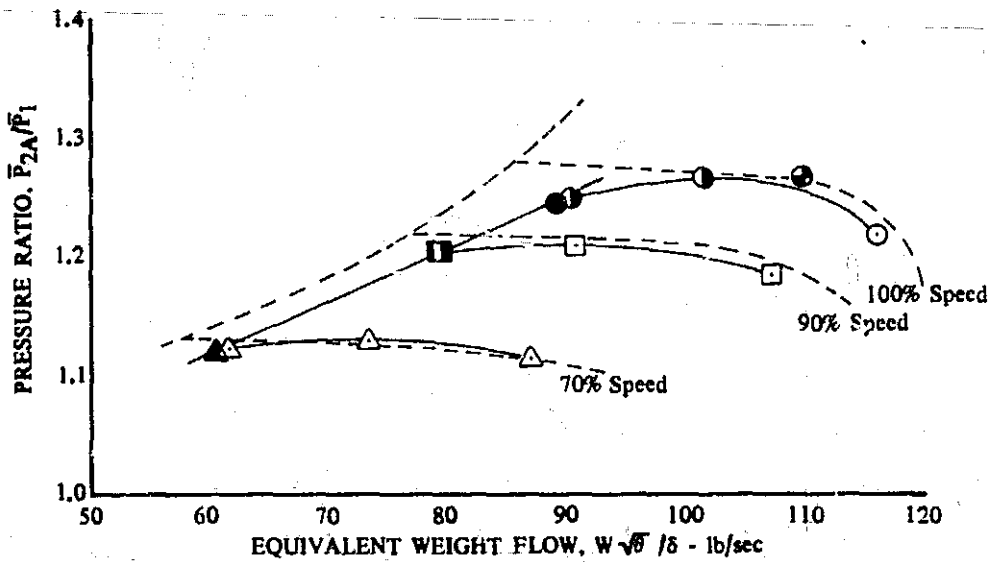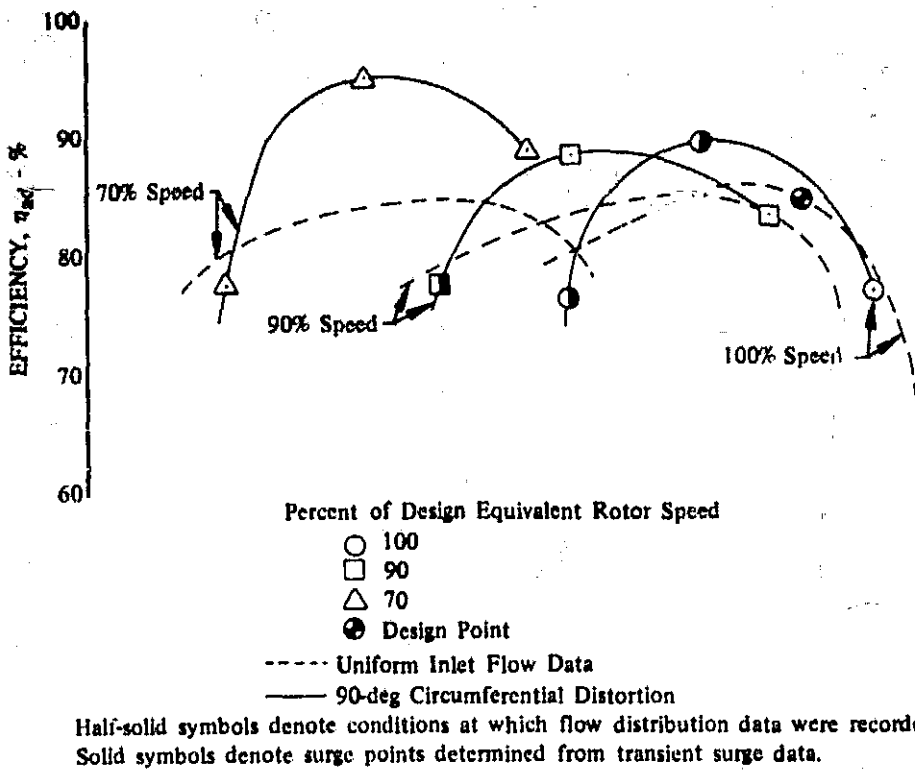
Figure 36. Overall Performance of Stage D;   DF 97774
            Circumferential Distortion Compared
            with Uniform Inlet Flow
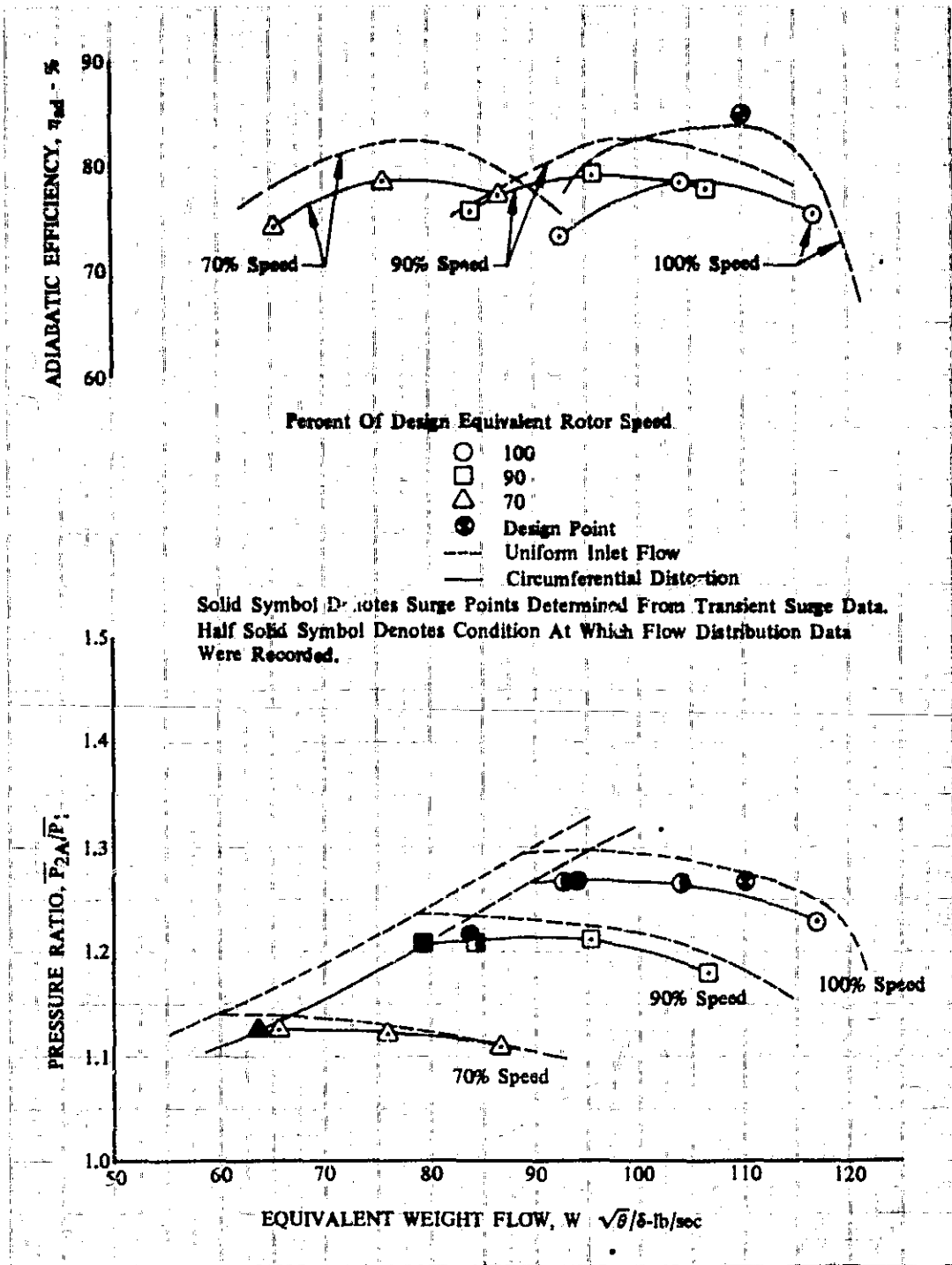
Figure 37. Overall Performance of Stage E;   DF 100343
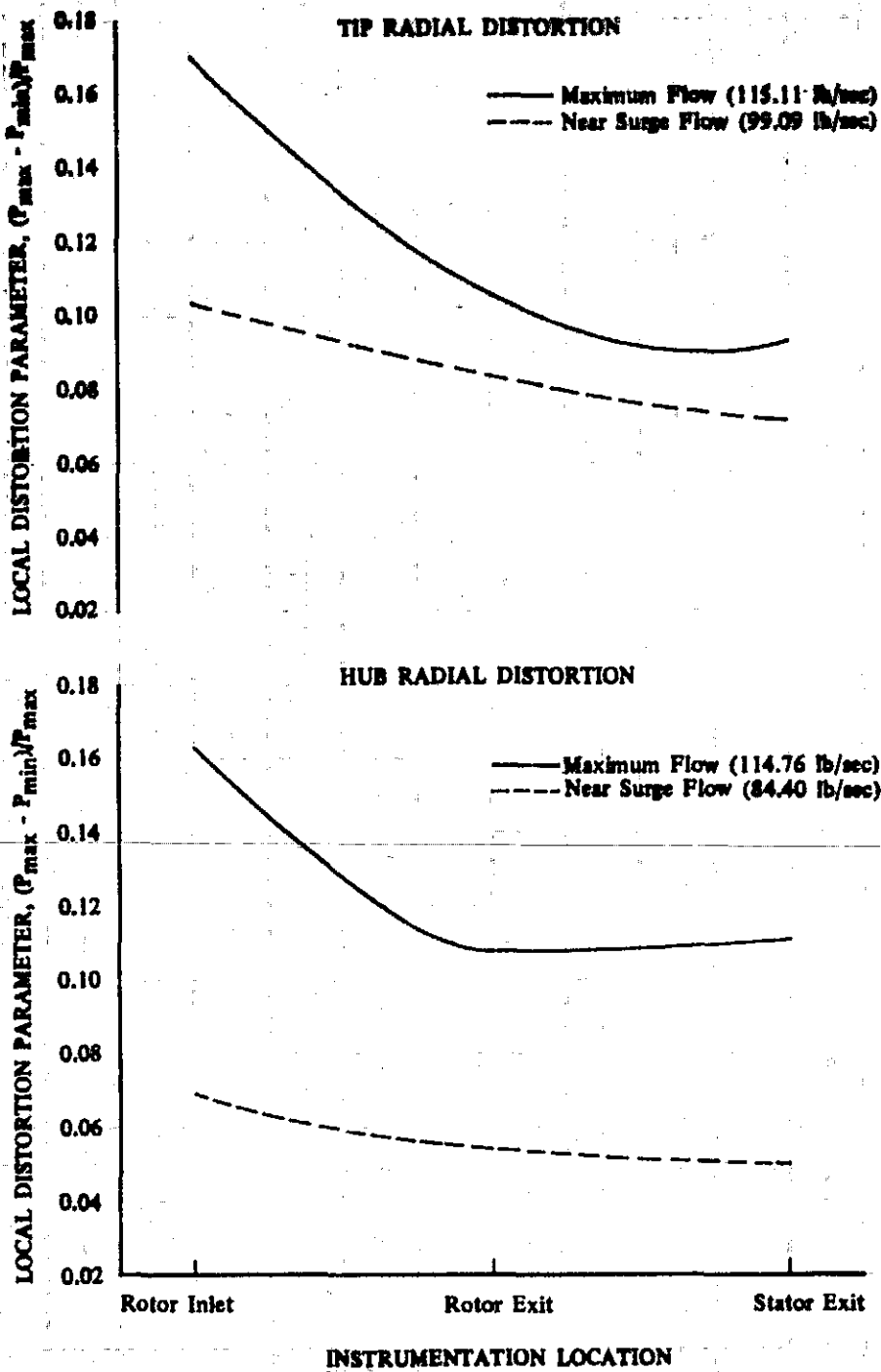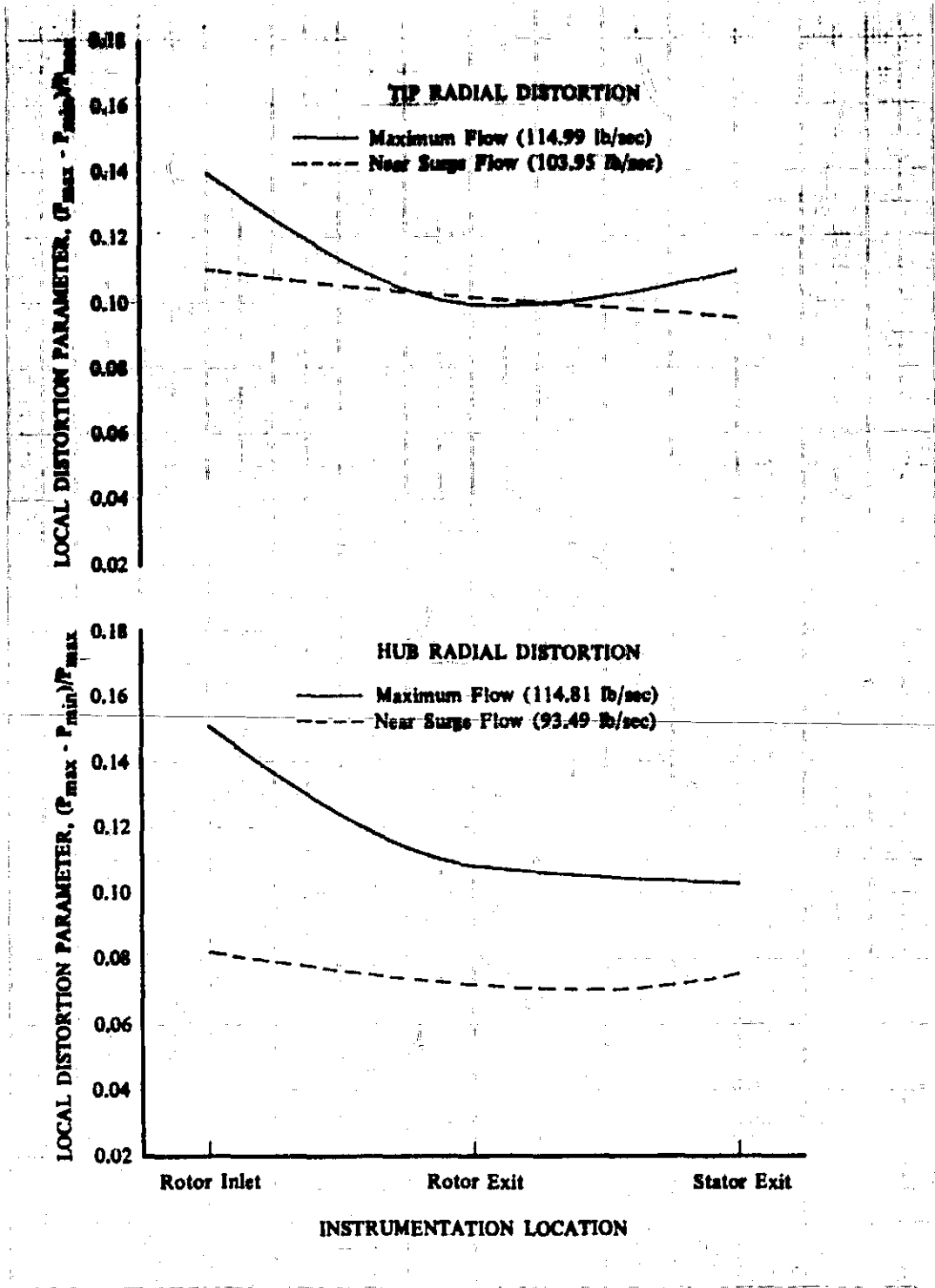Circumferential Distortion Compared
to Uniform Inlet Flow
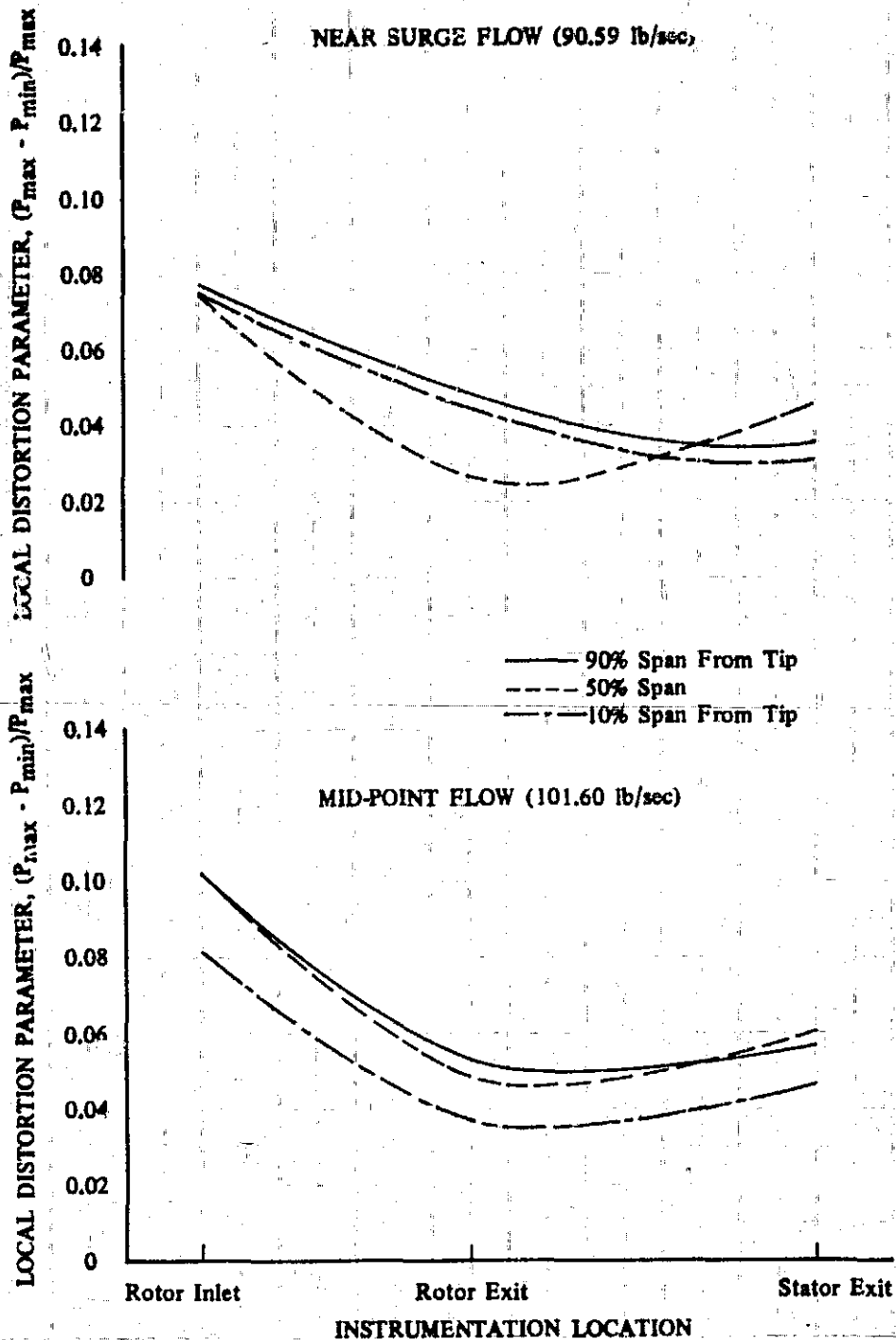
Figure 38. Local Distortion Parameter vs Instrumentation Location for Stage D; Design Equivalent Rotor Speed; Near Surge and Midpoint Flow; 10, 50, and 90% Span From Tip; Circumferential Distortion

DF 100344
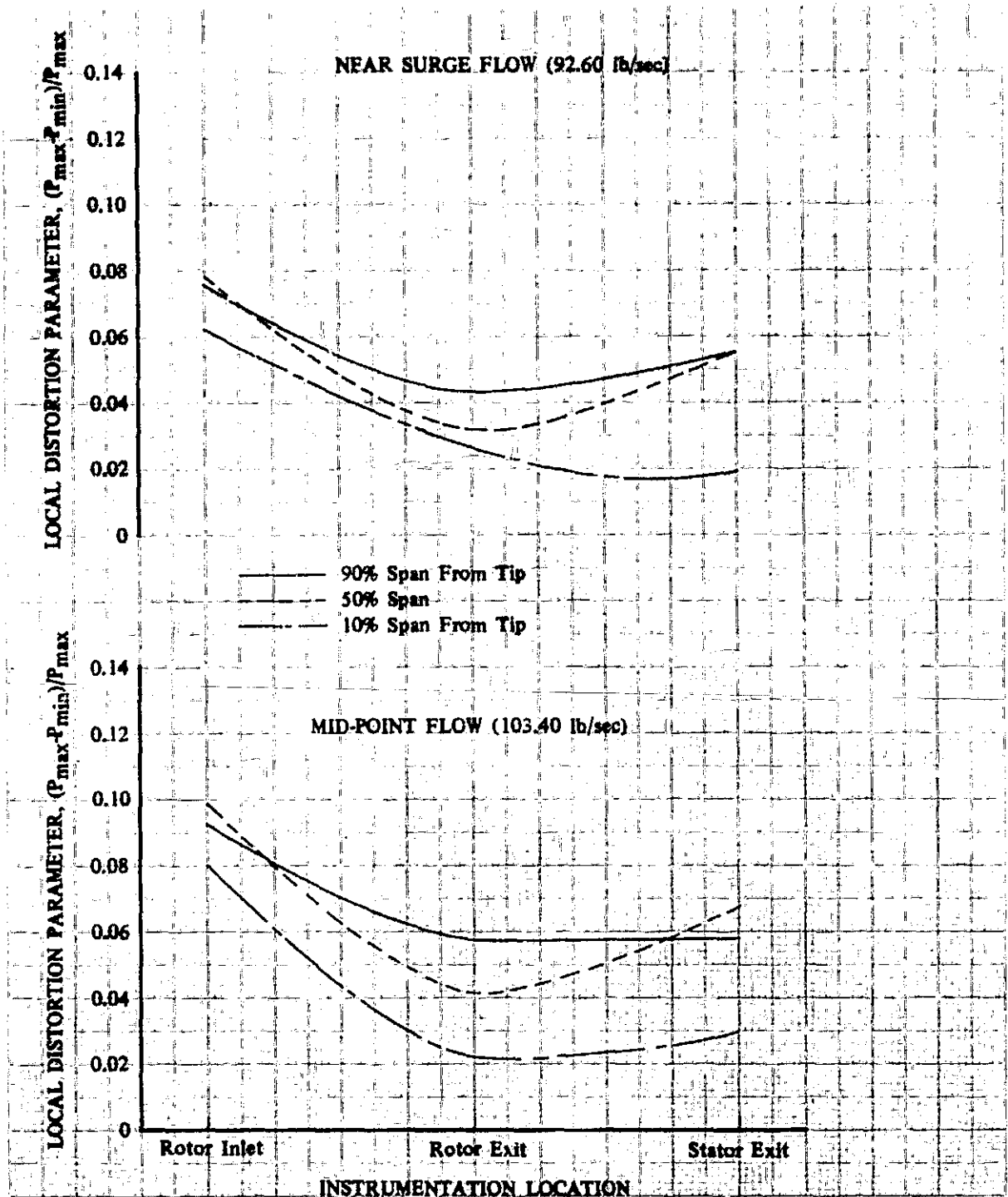
Figure 39. Local Distortion Parameter vs Instrumentation Location for Stage E; Design Equivalent Rotor Speed; Near Surge and Midpoint Flow; 10, 50, and 90% Span From Tip; Circumferential Distortion

DF 100345
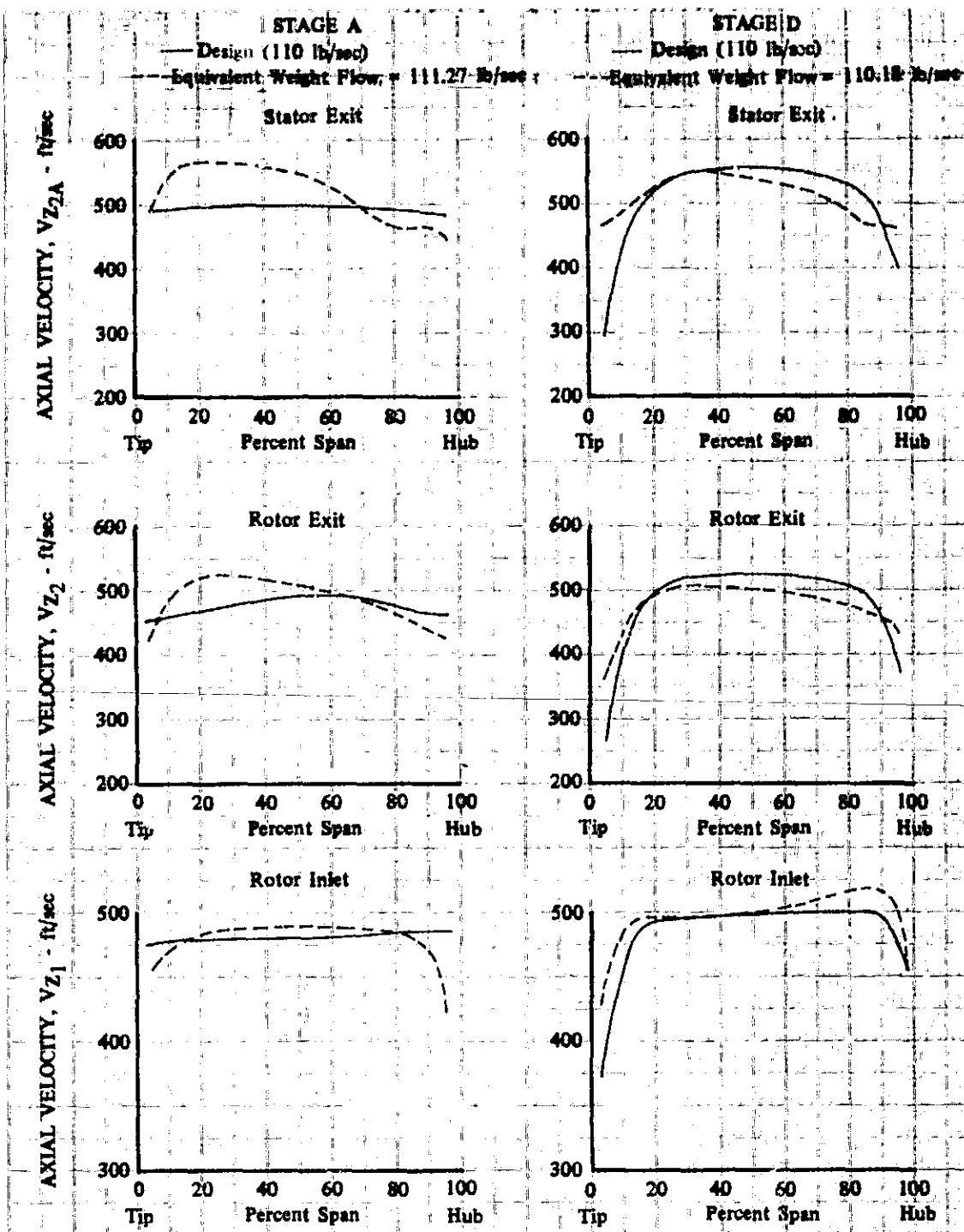
Figure 40. Comparison of Axial Velocity Profiles
to Corresponding Design Values for
Stages A and D at Rotor Inlet, Rotor
Exit, and Stator Exit; Design Equivalent
Rotor Speed

DF 100346
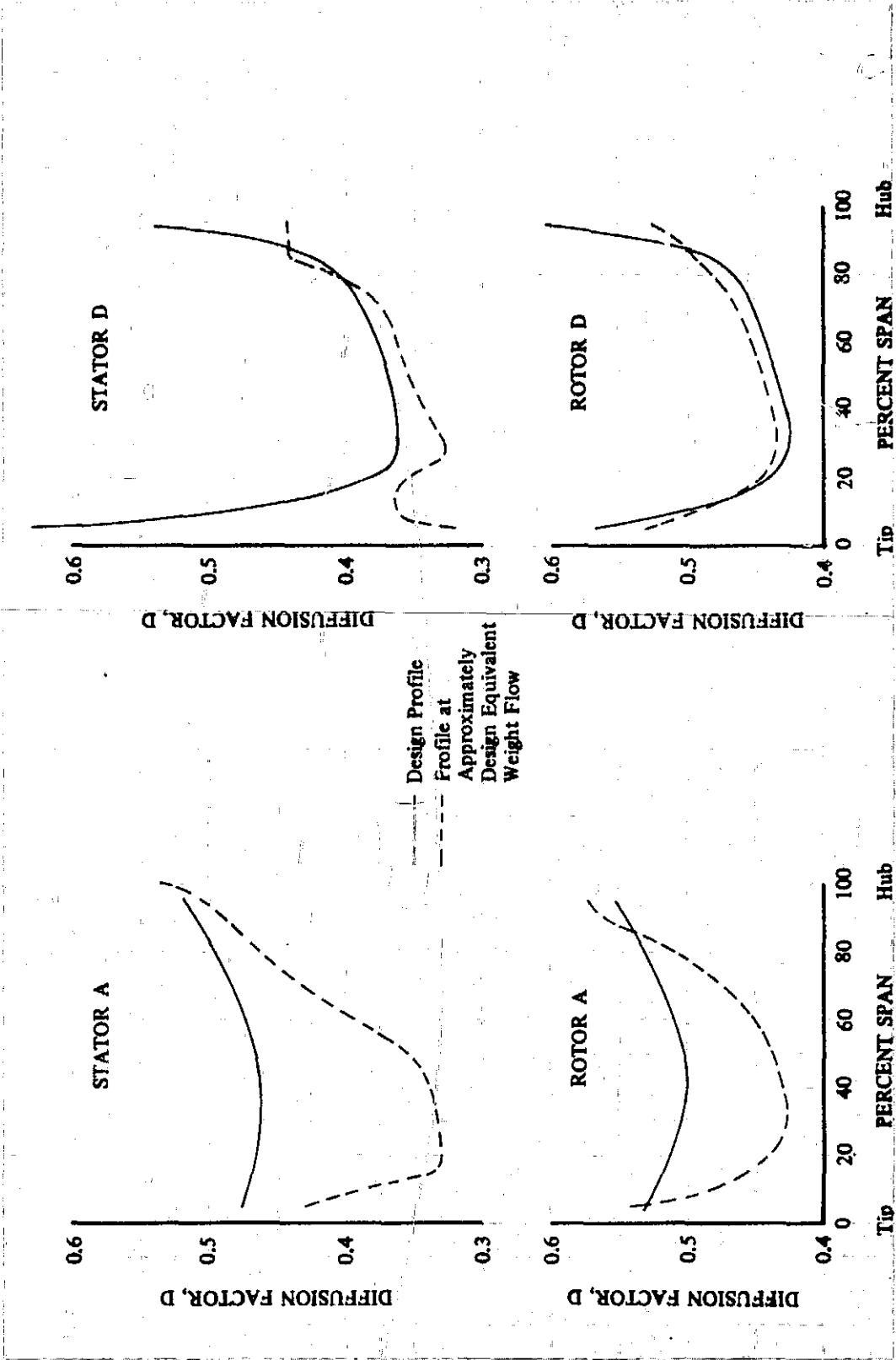
Figure 41. Comparison of Actual and Design Diffusion Factor Profiles at Approximately Design Equivalent Rotor Speed and Flow for Stages A and D; Uniform Inlet Flow

DF 100347

65
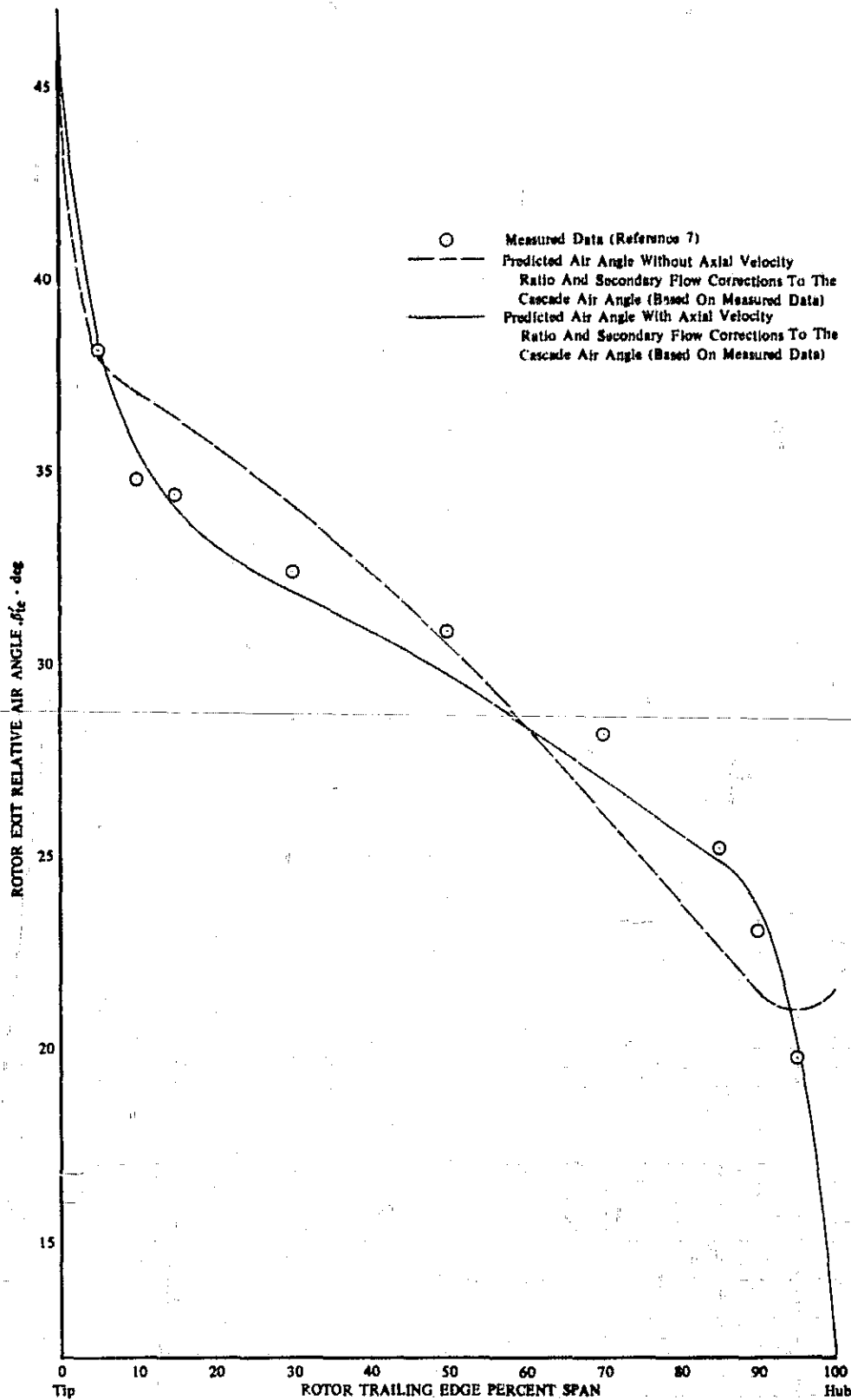
Figure 42. Effect of Axial Velocity Ratio and Secondary Flow Corrections on Rotor Exit Air Angle for Stage A

DF 93408
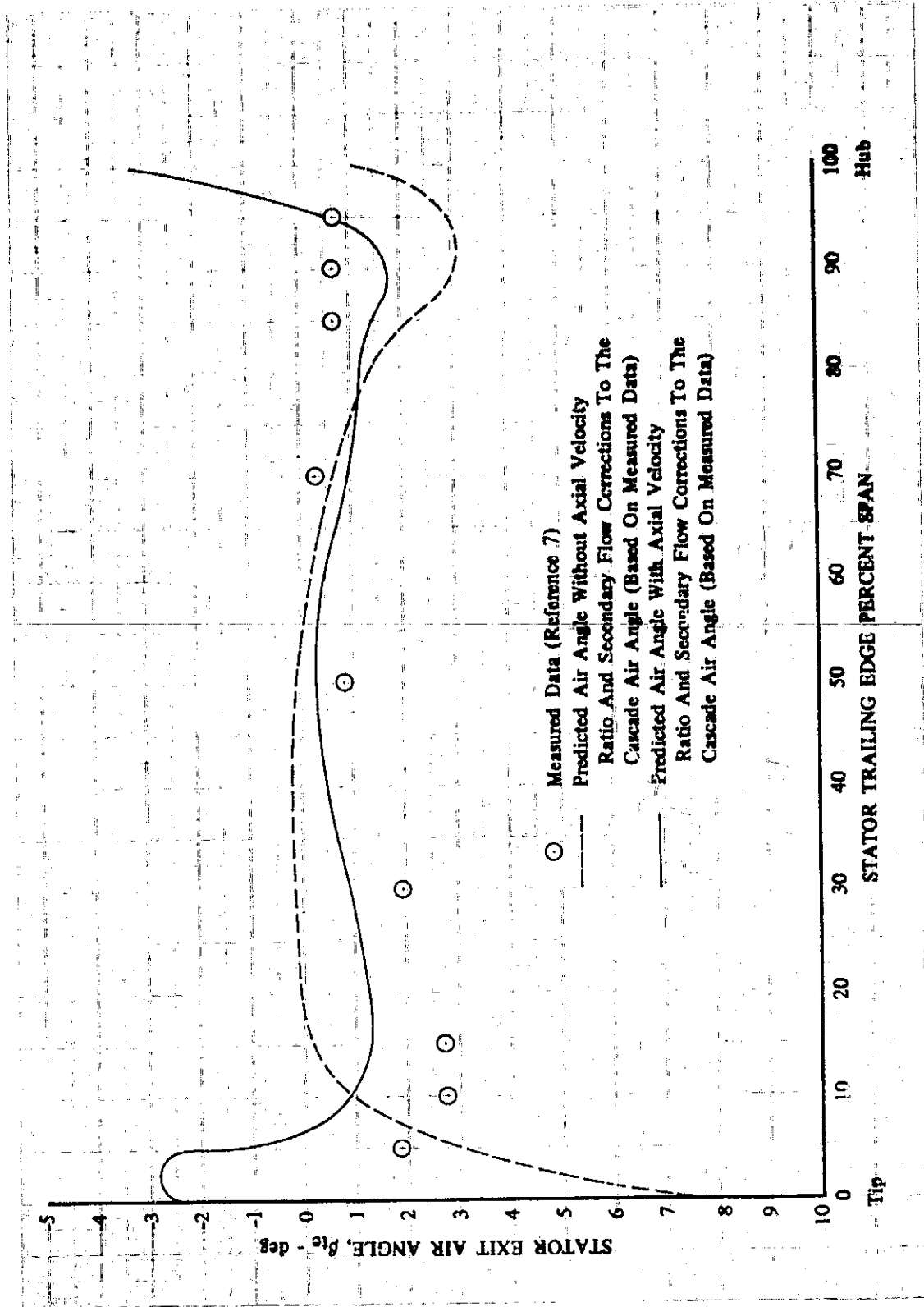
Figure 43. Effect of Axial Velocity Ratio and Secondary Flow Corrections on Stator Exit Air Angle
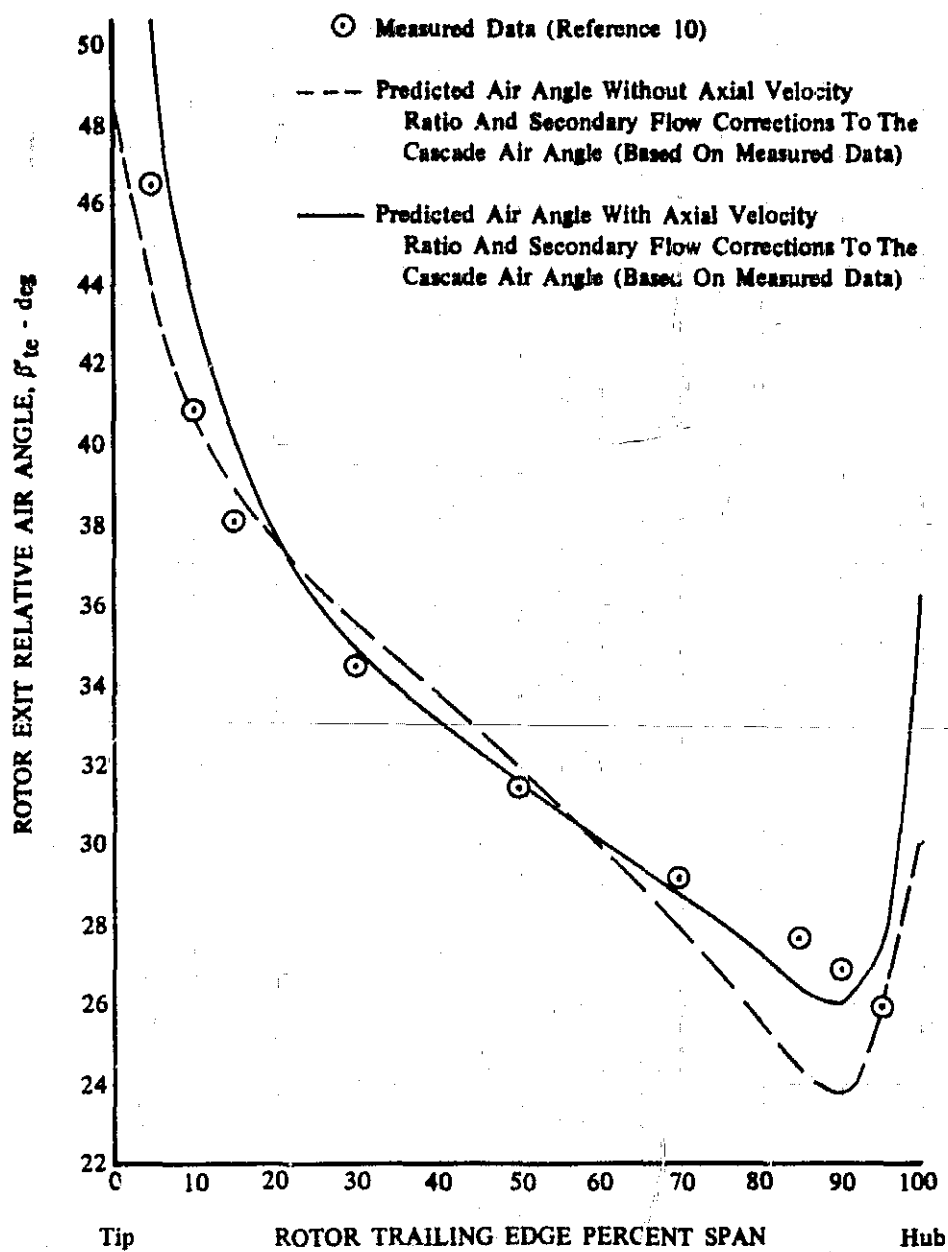
Figure 44. Effect of Axial Velocity Ratio and
Seconday Flow Correction on Rotor
Exit Angle for Stage D

DF 100348
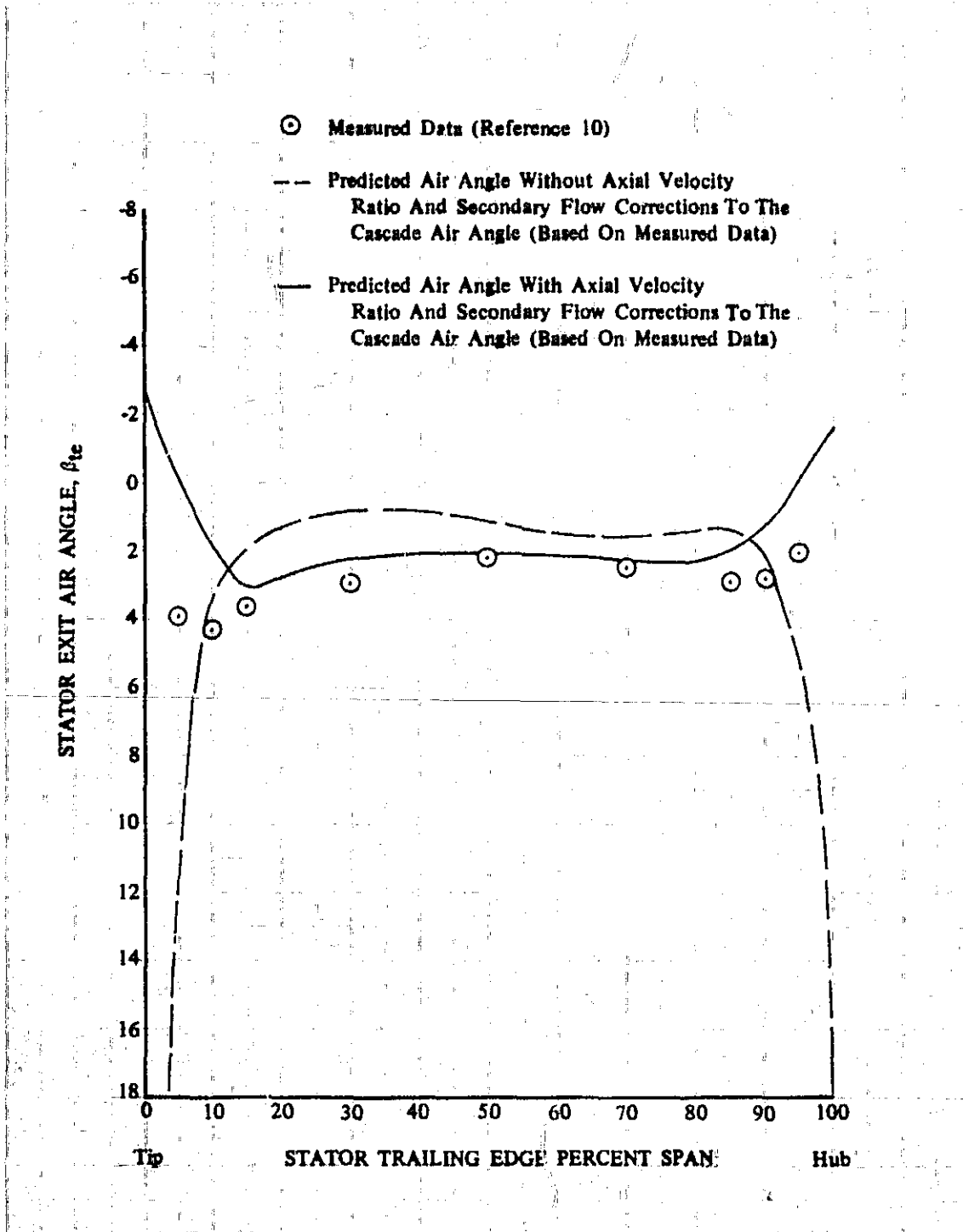
Figure 45. Effect of Axial Velocity Ratio and Secondary Flow Corrections on Stator Exit Air Angle for Stage D

DF 100349
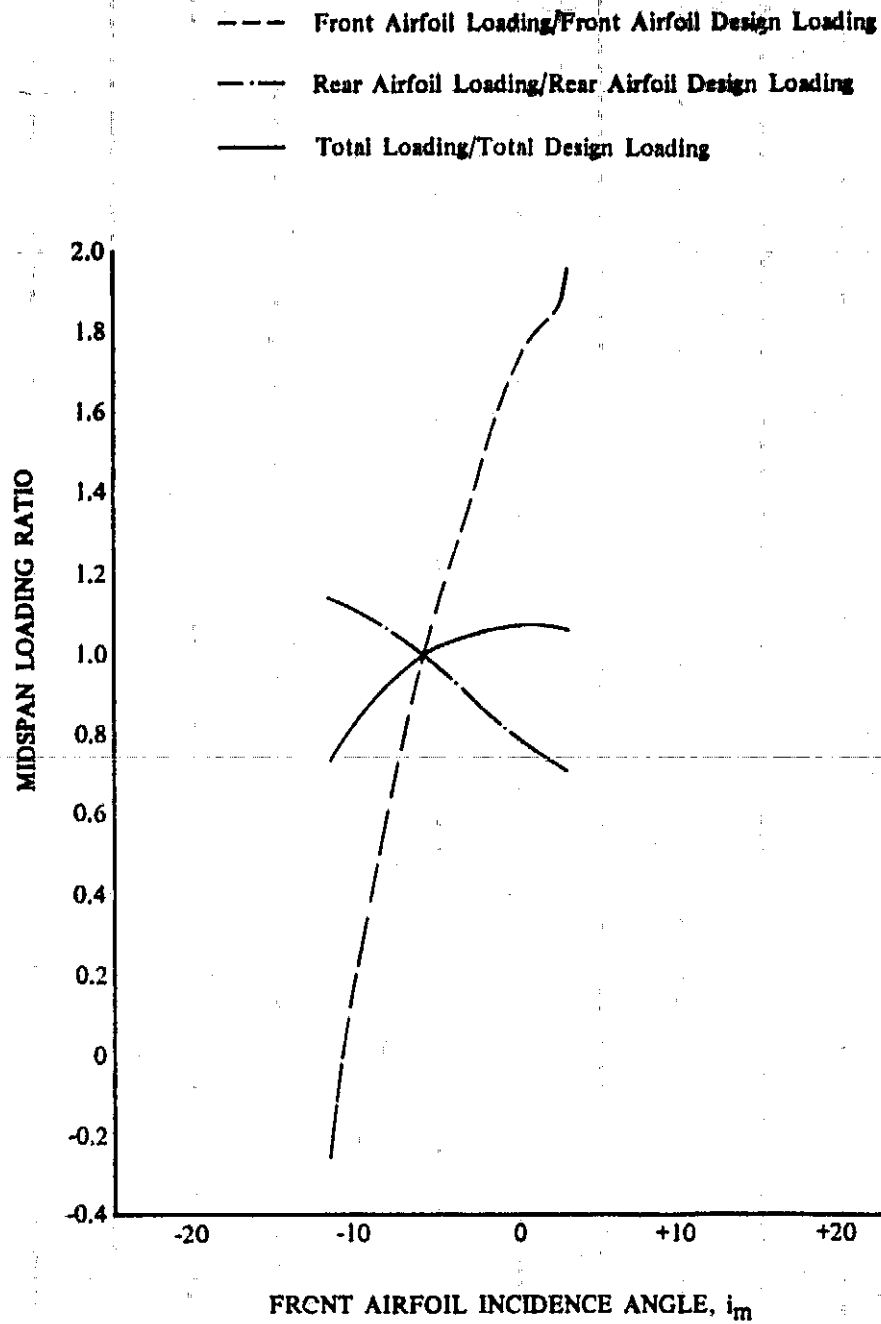
Figure 46. Tandem Stator B Midspan Loading
Change with Changing Front Airfoil
Incidence Angle; Design Equivalent
Rotor Speed; Uniform Inlet Flow
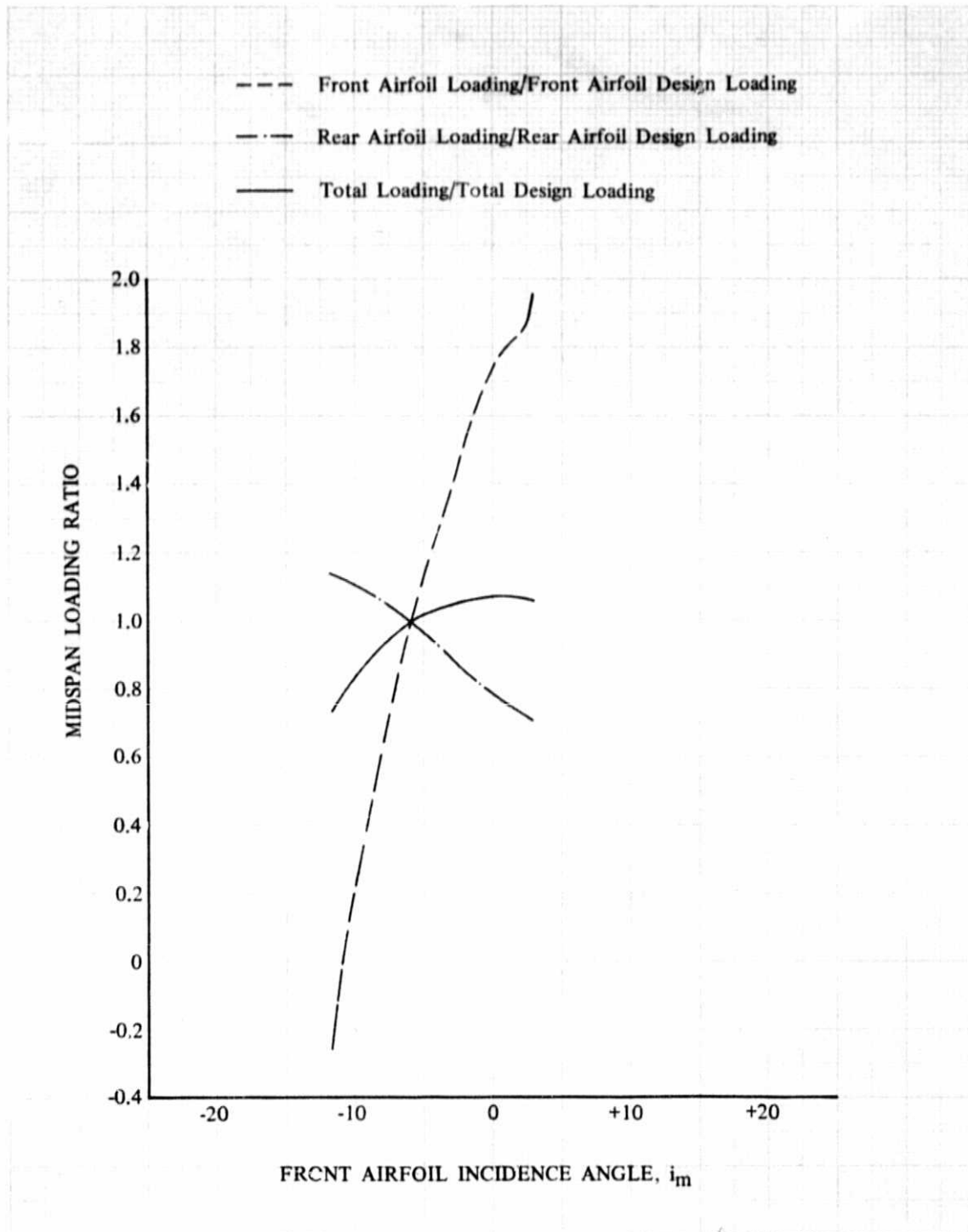
DF 100350

Figure 46. Tandem Stator B Midspan Loading Change with Changing Front Airfoil Incidence Angle; Design Equivalent Rotor Speed; Uniform Inlet Flow
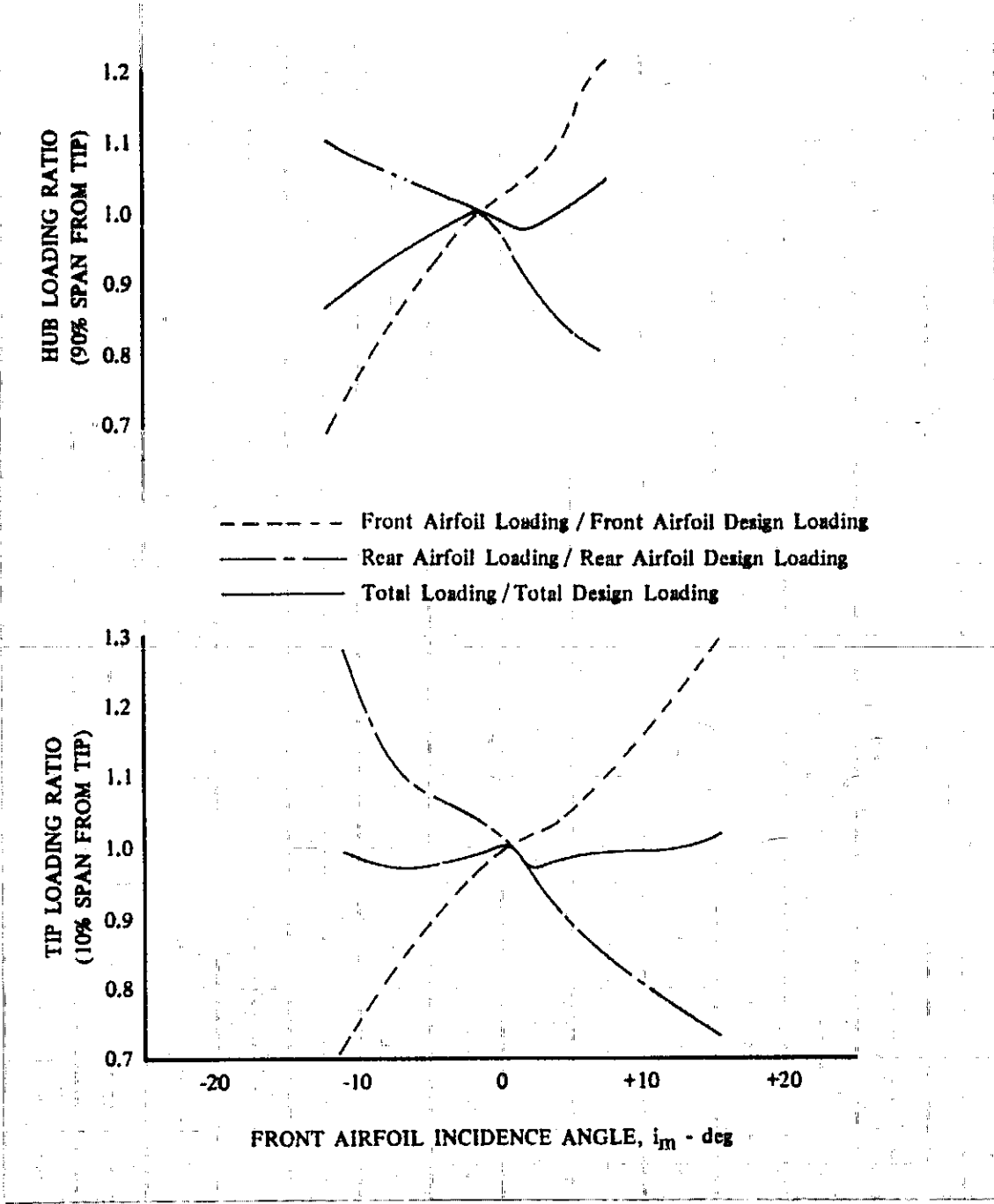
DF 100350

Figure 47. Tandem Stator E Hub and Tip Loading   DF 100351
Change with Changing Front Airfoil
Incidence Angle; Design Equivalent
Rotor Speed; Uniform Inlet Flow

APPENDIX A
TABLES OF BLADE AND VANE GEOMETRY

Tables A-1 through A-9 present geometry data for the rotor and stator airfoils used in the Task I and Task III investigations. Information included in these tables is defined on planes tangent to the conic surfaces that approximate design streamlines of revolution.

Table A-1. Rotor A Geometry Data

Airfoil: Circular Arc   No. of Blades: 70   Chord Length: 2.57 inches

Percent Span From Tip

	Leading Edge	Trailing Edge	κ'_{le} (deg)	κ'_{te} (deg)	ϕ (deg)	$\gamma°$ (deg)	σ	t/c	r_{le} (in.)	r_{te} (in.)
Hub	96.5	95.0	51.84	7.75	44.09	29.708	1.7241	0.0783	0.010	0.010
	91.5	90.0	52.28	9.30	42.98	30.705	1.7036	0.0763	0.010	0.010
	86.4	85.0	52.69	10.92	41.77	31.724	1.6835	0.0743	0.010	0.010
	70.9	70.0	54.06	15.70	38.36	34.826	1.6250	0.0682	0.009	0.009
	50.0	50.0	56.05	20.67	35.39	38.359	1.5528	0.0600	0.008	0.008
	29.1	30.0	58.03	24.82	33.22	41.443	1.4868	0.0518	0.007	0.007
	13.6	15.0	59.40	27.48	31.92	43.446	1.4409	0.0457	0.006	0.006
	8.5	10.0	59.83	28.05	31.77	43.960	1.4265	0.0437	0.006	0.006
Tip	3.5	5.0	60.60	28.78	31.82	44.696	1.4122	0.0417	0.006	0.006

Table A-2. Stator A Geometry Data

Airfoil: Circular Arc   No. of Vanes: 66   Chord Length: 2.35 inches

Percent Span From Tip

	Leading Edge	Trailing Edge	κ_{le} (deg)	κ_{te} (deg)	ϕ (deg)	$\gamma°$ (deg)	σ	t/c	r_{le} (in.)	r_{te} (in.)
Hub	95.0	95.0	46.97	-13.03	60.00	16.972	1.4850	0.09	0.014	0.014
	90.0	90.1	46.20	-12.85	59.06	16.768	1.4689	0.09	0.014	0.014
	85.0	85.2	45.47	-12.73	58.20	16.375	1.4531	0.09	0.014	0.014
	70.0	70.1	43.67	-12.33	56.00	15.673	1.4073	0.09	0.014	0.014
	50.0	50.0	42.23	-12.12	54.35	15.055	1.3504	0.09	0.014	0.014
	30.0	29.8	42.35	-12.71	55.06	14.825	1.2980	0.09	0.014	0.014
	15.0	14.8	43.30	-13.51	56.81	14.902	1.2614	0.09	0.014	0.014
	10.0	9.9	43.85	-13.81	57.66	15.027	1.2497	0.09	0.014	0.014
Tip	5.0	4.9	44.45	-14.15	52.61	15.153	1.2382	0.09	0.014	0.014

Table A-3. Tandem Rotor B Geometry Data

Airfoils: Circular Arc   Number of Blades: 70   Chord Lengths: 1.?? in.

Percent Span From Tip		Front Airfoil						Rear Airfoil						Each Airfoil	
Front Body Leading Edge	Rear Body Trailing Edge	κ_{le} (deg)	κ_{te} (deg)	ϕ (deg)	γ^* (deg)	r_{le} (in.)	r_{te} (in.)	κ_{le} (deg)	κ_{te} (deg)	ϕ (deg)	γ^* (deg)	r_{le} (in.)	r_{te} (in.)	θ	t/c
95.0	95.0	31.54	13.24	6.6	17.55	0.007	0.007	45.25	7.75	37.70	26.50	0.005	0.007	0.9721	0.0753
91.5	90.0	32.28	14.71	7.75	18.36	0.007	0.007	47.25	9.30	37.95	28.10	0.007	0.007	0.9410	0.0763
97.1	57.1	32.69	17.49	7.20	40.08	0.007	0.007	46.86	10.92	37.94	29.95	0.007	0.007	0.9495	0.0743
70.9	70.0	34.06	17.55	4.55	40.94	0.007	0.007	52.00	15.70	36.30	33.70	0.005	0.007	0.9130	0.0692
50.0	50.0	36.05	3.45	6.40	32.77	0.006	0.006	54.17	20.47	33.50	37.42	0.006	0.006	0.8731	0.0600
29.1	30.0	38.03	20.95	7.06	34.47	0.005	0.005	55.03	21.92	30.21	40.45	0.00	0.006	0.8397	0.0514
12.0	15.0	39.40	5.52	7.89	35.61	0.005	0.005	55.28	27.48	27.80	41.65	0.005	0.005	0.8127	0.0477
7.5	7.5	39.87	31.60	8.23	35.98	0.005	0.005	55.29	28.05	27.24	41.90	0.005	0.005	0.8041	0.0457
3.5	3.0	40.00	32.06	8.50	36.29	0.00	0.005	55.24	28.78	26.50	42.03	0.005	0.005	0.7962	0.0447

Hub (first rows) ... Tip (last rows)

Table A-4. Tandem Stator B Geometry Data

Airfoils: Circular Arc   Number of Vanes: 66   Chord Lengths: 1.30 in.

Percent Span From Tip		Front Airfoil						Rear Airfoil						Each Airfoil	
Front Body Leading Edge	Rear Body Trailing Edge	κ_{le} (deg)	κ_{te} (deg)	ϕ (deg)	γ^* (deg)	r_{le} (in.)	r_{te} (in.)	κ_{le} (deg)	κ_{te} (deg)	ϕ (deg)	γ^* (deg)	r_{le} (in.)	r_{te} (in.)	θ	t/c
95.0	95.0	46.97	31.97	12.00	40.97	0.005	0.005	39.17	-13.01	13.00	13.22	0.005	0.005	0.722	0.09
90.0	90.1	46.19	31.03	11.53	40.45	0.005	0.005	39.30	-12.45	31.33	13.09	0.005	0.005	0.813	0.09
70.0	70.0	45.31	31.27	11.24	39.95	0.005	0.005	39.10	-12.53	31.65	13.00	0.005	0.005	0.404	0.09
70.0	70.1	43.77	32.27	10.70	38.55	0.005	0.005	38.19	-12.16	30.50	13.00	0.005	0.005	0.774	0.09
50.0	50.7	42.23	32.33	10.00	37.23	0.005	0.005	37.44	-12.12	30.49	12.88	0.005	0.005	0.747	0.09
30.0	30.7	42.35	31.90	10.45	37.40	0.005	0.005	37.40	-12.66	30.26	12.50	0.005	0.005	0.714	0.09
15.0	11.8	43.40	32.20	11.20	35.70	0.005	0.005	39.00	-13.30	31.30	12.65	0.005	0.005	0.492	0.09
10.0	9.9	43.90	32.05	11.53	34.65	0.004	0.005	38.11	-13.90	32.05	12.03	0.005	0.005	0.492	0.09
5.0	4.0	44.45	32.13	12.00	35.50	0.005	0.005	35.50	-14.10	33.00	13.40	0.005	0.005	0.435	0.09

Hub (first rows) ... Tip (last rows)

75

Table A-5. Tandem Rotor C Geometry Data

Airfoils: Circular Arc Number of Blades: 70 Chord Lengths: 1.35 inches

Percent Span From Tip

	Front Body Leading Edge	Rear Body Trailing Edge	Front Airfoil κ_{le} (deg)	κ_{te} (deg)	ϕ (deg)	γ^* (deg)	r_{le} (in.)	r_{te} (in.)	Rear Airfoil κ_{le} (deg)	κ_{te} (deg)	ϕ (deg)	γ^* (deg)	r_{le} (in.)	Each Airfoil r_{te} (in.)	σ	t/c
Hub	95.0	95.0	51.75	36.63	15.10	44.23	0.005	0.005	42.75	7.75	35.00	25.15	0.005	0.005	0.929	0.0753
	91.5	90.0	52.19	37.39	14.60	44.85	0.005	0.005	41.10	9.10	34.00	26.05	0.005	0.005	0.909	0.0753
	86.4	85.0	52.60	38.40	14.20	45.47	0.005	0.005	43.50	10.70	32.80	27.08	0.005	0.005	0.899	0.0743
	70.9	70.0	54.04	41.04	13.00	47.60	0.004	0.004	45.00	15.45	29.55	30.25	0.004	0.004	0.864	0.0752
	50.0	50.0	56.10	44.10	12.00	50.10	0.004	0.004	46.67	20.67	26.00	33.67	0.004	0.004	0.829	0.0600
	29.1	30.0	58.09	46.18	11.91	52.05	0.003	0.003	48.95	25.00	23.95	37.00	0.003	0.003	0.791	0.0515
	13.6	15.0	59.60	47.20	12.40	53.68	0.003	0.003	51.65	27.50	24.15	40.05	0.003	0.003	0.707	0.0477
	8.5	10.0	60.18	47.46	12.72	54.10	0.003	0.003	52.63	28.03	24.53	41.10	0.003	0.003	0.730	0.0435
Tip	5.7	5.0	60.75	47.72	13.03	54.45	0.003	0.003	53.78	28.78	23.00	42.03	0.003	0.003	0.731	0.0417

76

Table A-6. Rotor D Geometry Data

Airfoil: Simulated Double-Circular-Arc* Number of Blades: 70 Chord Length: 2.57 inches

Percent Span From Tip

	Leading Edge	Trailing Edge	κ'_{le} (deg)	κ_{te} (deg)	ϕ (deg)	$\gamma°$ (deg)	σ	t/c	r_{le} (in.)	r_{te} (in.)
Hub	96.8	95.0	52.42	15.14	37.27	33.78	1.725	0.0782	0.009	0.009
	92.0	90.0	50.91	14.15	36.75	32.53	1.705	0.0763	0.009	0.009
	86.9	85.0	50.57	14.63	35.94	32.60	1.684	0.0743	0.009	0.009
	71.0	70.0	52.04	18.64	33.40	35.34	1.627	0.0691	0.008	0.008
	49.5	50.0	53.96	23.19	30.77	38.58	1.553	0.0599	0.007	0.007
	28.1	30.0	55.88	31.53	26.98	45.02	1.439	0.0454	0.006	0.006
	7.1	10.0	62.12	33.03	29.09	47.58	1.424	0.0433	0.006	0.006
Tip	3.0	5.0	68.00	35.87	32.12	51.93	1.412	0.0415	0.006	0.006

*Mean camber line and suction and pressure surface lines of each blade element are lines with a constant rate of angle change with path distance on the conic surface, which approximates the design streamline of revolution.

Table A-7. Stator D Geometry Data

Airfoil: Simulated Double-Circular-Arc* Number of Vanes: 66 Chord Length: 2.35 inches

Percent Span From Tip

	Leading Edge	Trailing Edge	κ_{le} (deg)	κ_{te} (deg)	ϕ (deg)	$\gamma°$ (deg)	σ	t/c	r_{le} (in.)	r_{te} (in.)
Hub	95.0	95.0	50.16	- 8.83	59.00	20.66	1.484	0.09	0.010	0.010
	90.0	90.0	43.38	-11.31	54.70	16.03	1.468	0.09	0.010	0.010
	85.0	85.0	40.28	-11.31	51.60	14.48	1.453	0.09	0.010	0.010
	70.0	70.0	38.02	-10.97	49.00	13.52	1.407	0.09	0.010	0.010
	50.0	50.0	36.68	-11.01	47.70	12.83	1.350	0.09	0.010	0.010
	30.0	30.0	35.83	-11.66	47.50	12.08	1.298	0.09	0.010	0.010
	15.0	15.0	38.65	-12.44	51.10	13.10	1.262	0.09	0.010	0.010
	10.0	10.0	43.11	-12.68	55.80	15.21	1.250	0.09	0.023	0.010
Tip	5.0	5.0	59.14	- 4.85	64.00	27.14	1.238	0.09	0.040	0.014

*Mean camber line and suction and pressure surface lines of each blade element are lines with a constant rate of angle change with path distance on the conic surface, which approximates the design streamline of revolution.

Table A-8. Tandem Rotor E Geometry Data

Airfoil: Simulated Double-Circular-Arc* Number of Blades: 70 Chord Length: 2.? in.

	Percent Span From Tip		Front Airfoil						Rear Airfoil						Each Airfoil	
	Front Body Leading Edge	Rear Body Trailing Edge	κ_{le} (deg)	κ_{te} (deg)	r_{le} (in.)	r_{te} (in.)	ϕ (deg)	γ^* (deg)	κ_{le} (deg)	κ_{te} (deg)	r_{le} (in.)	r_{te} (in.)	ϕ (deg)	γ^* (deg)	σ	t/c
Hub	96.8	95.0	52.420	39.220	0.006	0.006	13.200	45.820	42.420	15.110	0.006	0.006	27.290	23.730	0.904	0.075
	92.0	90.0	50.910	37.910	0.006	0.006	13.000	44.410	41.180	14.150	0.006	0.006	26.930	27.611	0.894	0.076
	86.9	85.0	50.570	37.790	0.006	0.006	12.780	44.180	41.110	14.630	0.006	0.006	26.510	27.723	0.857	0.074
	71.0	70.0	52.040	39.880	0.006	0.006	12.160	45.960	43.390	18.140	0.006	0.006	24.940	31.110	0.839	0.069
	49.5	50.0	53.960	42.590	0.006	0.006	11.370	48.275	45.170	23.130	0.006	0.006	22.280	34.330	0.818	0.060
	28.1	30.0	55.880	45.160	0.006	0.006	10.720	50.520	47.640	27.500	0.006	0.006	20.140	37.670	0.771	0.052
	12.0	15.0	58.510	48.090	0.008	0.006	10.420	53.300	50.790	31.530	0.006	0.006	19.230	41.160	0.733	0.046
	7.1	10.0	62.120	49.020	0.011	0.006	13.100	53.570	52.430	33.030	0.006	0.006	19.400	42.730	0.719	0.044
Tip	3.0	5.0	68.000	52.100	0.016	0.006	15.900	60.050	55.790	35.870	0.006	0.006	19.920	45.830	0.705	0.042

*Mean camber line and suction and pressure surface lines of each blade element are lines with a constant rate of angle change with path distance on the conic surface, which approximates the design streamline of revolution.

Table A-9. Tandem Stator E Geometry Data

Airfoil: Simulated Double-Circular-Arc* Number of Vanes: 66 Chord Length: 2.35 in.

	Percent Span From Tip		Front Airfoil						Rear Airfoil						Each Airfoil	
	Front Body Leading Edge	Rear Body Trailing Edge	κ_{le} (deg)	κ_{te} (deg)	r_{le} (in.)	r_{te} (in.)	ϕ (deg)	γ^* (deg)	κ_{le} (deg)	κ_{te} (deg)	r_{le} (in.)	r_{te} (in.)	ϕ (deg)	γ^* (deg)	σ	t/c
Hub	95.0	95.0	50.160	25.160	0.008	0.006	25.00	37.660	28.170	-8.830	0.006	0.008	37.00	9.670	0.775	0.09
	90.0	90.0	43.380	19.780	0.007	0.006	23.60	31.580	22.940	-11.310	0.006	0.007	34.25	5.815	0.739	0.09
	85.0	85.0	40.280	17.630	0.006	0.006	22.65	28.955	20.990	-11.310	0.006	0.006	32.30	4.840	0.713	0.09
	70.0	70.0	38.020	16.880	0.006	0.006	21.14	27.450	18.890	-12.970	0.006	0.006	29.86	3.960	0.678	0.09
	50.0	56.0	36.680	16.680	0.006	0.006	20.00	26.680	18.490	-12.010	0.006	0.006	29.50	3.740	0.656	0.09
	30.0	30.0	35.830	16.470	0.006	0.006	19.36	26.150	18.320	-11.660	0.006	0.006	29.98	3.330	0.644	0.09
	15.0	15.0	38.650	17.000	0.008	0.006	21.65	27.825	19.600	-12.440	0.006	0.006	32.04	3.580	0.643	0.09
	10.0	10.0	43.110	19.360	0.013	0.006	23.75	31.230	20.930	-12.680	0.006	0.006	33.61	4.125	0.645	0.09
Tip	5.0	5.0	59.110	27.140	0.035	0.006	32.00	43.140	31.650	-4.850	0.006	0.010	36.50	13.400	0.649	0.09

*Mean camber line and suction and pressure surface lines of each blade element are lines with a constant rate of angle change with path distance on the conic surface, which approximates the design streamline of revolution.

APPENDIX B
DEFINITION OF SYMBOLS AND PERFORMANCE VARIABLES

a'_0	Inlet relative stagnation velocity of sound, ft/sec
c	Chord length, in.
d	Diameter, in.
D	Diffusion factor
g	Gravitation constant, 32.2 lb_m $-ft/lb_f-sec^2$
i_m	Incidence angle, deg
J	Mechanical equivalent of heat, 778.2 ft-lb_f/Btu
M	Mach number
N	Rotor speed, rpm
P	Total pressure, psia
p	Static pressure, psia
R	Gas constant for air, 53.34 ft-lb_f/lb_m - °R
r	Radius, in.
S	Blade passage gap (leading edge), in.
t	Blade maximum thickness, in.
T	Total temperature, °R
T_s	Static temperature, °R
U	Rotor speed, ft/sec
V	Velocity, ft/sec
W	Actual flowrate, lb_m/sec
α	Cone angle (angle of plane tangent to conic surface that approximates the design streamline of revolution), deg
β	Air angle, deg from axial direction
γ	Ratio of specific heats
$\gamma°$	Blade-chord angle, deg from axial direction

Definitions of Symbols and Performance Variables (Continued)

δ Ratio of total pressure to NASA standard sea level pressure of 14.694 psia

δ° Deviation angle, deg

η_{ad} Adiabatic efficiency

θ Ratio of total temperature to NASA standard sea level temperature of 518.7°R

κ Blade metal angle, deg from axial direction

σ Solidity, c/s

ϕ Blade camber angle, $\kappa_{le} - \kappa_{te}$, deg

$\bar{\omega}$ Loss coefficient

$\bar{\omega}\cos\beta/2\sigma$ Loss parameter

Subscripts:

0   Compressor inlet (bellmouth)

1   Rotor inlet

2   Rotor exit

2A   Stator exit

id   Isentropic condition

m   Mean, mass, or minimum loss

le   Leading edge

te   Trailing edge

s   Static condition

z   Axial component

θ Tangential component

Superscripts:

'   Related to rotor blade

—   Mass average value

80

Definition of Overall Performance Variables

Pressure Ratio:

Rotor: $\dfrac{\overline{P}_2}{\overline{P}_1}$ Stage: $\dfrac{\overline{P}_{2A}}{\overline{P}_1}$

Corrected Flow:

$$\frac{W\sqrt{\theta}}{\delta}$$

Equivalent Rotor Speed:

$$N/\sqrt{\theta}$$

Adiabatic Efficiency:

Rotor: $\dfrac{(\overline{P}_2/\overline{P}_1)^{\frac{\gamma-1}{\gamma}} - 1}{\overline{T}_{2A}/518.7 - 1}$ Stage: $\dfrac{(\overline{P}_2/\overline{P}_1)^{\frac{\gamma-1}{\gamma}} - 1}{\overline{T}_{2A}/518.7 - 1}$

Surge Margin at Peak Efficiency Point:

Stage: $\left\{ \left[\dfrac{\overline{P}_{2A}/\overline{P}_1}{W\sqrt{\theta}/\delta}\right]_{surge} \middle/ \left[\dfrac{\overline{P}_{2A}/\overline{P}_1}{W\sqrt{\theta}/\delta}\right]_{\substack{peak\\efficiency}} - 1.0 \right\}$

Definition of Blade Element Performance Variables

Incidence Angle:

Rotor: $i_m = \beta'_1 - \kappa_{le}$ Stator: $i_m = \beta_2 - \kappa_{le}$

Diffusion Factor:

Rotor: $D = 1 - \dfrac{V'_2}{V'_1} + \dfrac{d_2 V_{\theta 2} - d_1 V_{\theta 1}}{(d_1 + d_2) V'_1 \sigma}$

Stator: $D = 1 - \dfrac{V'_{2A}}{V_2} + \dfrac{d_2 V_{\theta 2} - d_{2A} V_{\theta 2A}}{(d_2 + d_{2A}) V_2 \sigma}$

Deviation Angle:

$$\text{Rotor:} \quad \delta^\circ = \beta'_2 - \kappa_{te} \qquad\qquad \text{Stator} \; \delta^\circ = \beta_{2A} - \kappa_{te}$$

Loss Coefficient:

$$\text{Rotor:} \quad \bar{\omega}' = \frac{P'_{2_{id}} - P'_2}{P'_1 - p_1}$$

where:

$$P'_{2_{id}} = P'_1 \left\{ 1 + \frac{\gamma - 1}{2} \left(\frac{U_2^2}{a'^2_{0_1}} \right) \left[1 - \left(\frac{d_1}{d_2} \right)^2 \right] \right\}^{\frac{\gamma}{\gamma - 1}}$$

P' is found from $p/P' = \left[1 + \dfrac{\gamma - 1}{2} M'^2 \right]^{\frac{\gamma}{1 - \gamma}}$

and M' is calculated using trigonometric functions and the measurements of U, β, P, and p.

$$\text{Stator:} \quad \bar{\omega} = \frac{P_{2_1} - \bar{P}_{2A}}{P_{2_1} - p_2}$$

where:

$\quad P_{2_1}$ = the wake rake freestream total pressure

REFERENCES

1. Sheets, H. E., "The Slotted-Blade Axial-Flow Blower," Transactions of the ASME, November 1956.

2. Linnemann, H., "Tandem Grid in a Single-Stage Axial Blower," Translated from Konstrucktion by Redstone Scientific Information Center, No. 276, 21 September 1964.

3. Sanger, N. L., "Analytical Study of the Effects of Geometric Changes on the Flow Characteristics of Tandem-Bladed Compressor Stators," NASA TND-6264, March 1971.

4. Sanger, N. L., "Analytical Study on a Two-Dimensional Plane of the Off-Design Flow Properties of Tandem-Bladed Compressor Stators," NASA TM X-2734, March 1973.

5. Brent, J. A., J. G. Cheatham, and A. W. Nilsen, "Single-Stage Experimental Evaluation of Tandem-Airfoil Rotor and Stator Blading for Compressors, Part I - Analysis and Design of Stages A, B, and C," NASA CR-120803, PWA FR-4667, June 1972.

6. Brent, J. A., J. G. Cheatham, and D. R. Clemmons, "Single-Stage Experimental Evaluation of Tandem-Airfoil Rotor and Stator Blading for Compressors, Part V - Analysis and Design of Stages D and E," NASA CR-121008, PWA FR-5212, December 1972.

7. Brent, J. A., "Single-Stage Experimental Evaluation of Tandem-Airfoil Rotor and Stator Blading for Compressors, Part II - Data and Performance for Stage A," NASA CR-120804, PWA FR-4719, July 1972.

8. Brent, J. A., and D. R. Clemmons, "Single-Stage Experimental Evaluation of Tandem-Airfoil Rotor and Stator Blading for Compressors, Part III - Data and Performance for Stage C," NASA CR-120938, PWA FR-5028, August 1972.

9. Brent, J. A. and J. G. Cheatham, "Single-Stage Experimental Evaluation of Tandem-Airfoil Rotor and Stator Blading for Compressors, Part IV - Data and Performance for Stage B," NASA CR-121145, PWA FR-5083, June 1973.

10. Clemmons, D. R., "Single-Stage Experimental Evaluation of Tandem-Airfoil Rotor and Stator Blading for Compressors, Part VI - Data and Performance for Stage D," NASA CR-134511, PWA FR-5852, November 1973.

11. Cheatham, J. G., "Single-Stage Experimental Evaluation of Tandem-Airfoil Rotor and Stator Blading for Compressors, Part VII - Data and Performance for Stage E," NASA CR-134529, PWA FR-5955, January 1974.

12. "Aerodynamic Design of Axial Flow Compressor" (Revised), NASA SP-36, 1965.